Winter 1996

Optical Fiber Fourier Transform Infrared Evanescent Wave Absorption Spectroscopy of Aluminum Hydroxide and Natural Corrosion

Juock S. Namkung
Old Dominion University

OPTICAL FIBER
FOURIER TRANSFORM INFRARED
EVANESCENT WAVE ABSORPTION SPECTROSCOPY
OF
ALUMINUM HYDROXIDE AND NATURAL CORROSION

by

Juock S. Namkung
Master of Science, May 1979, College of William & Mary

A Dissertation submitted to the Faculty of
Old Dominion University in Partial Fulfillment of the
Requirements for the Degree of

DOCTOR OF PHILOSOPHY

ELECTRICAL ENGINEERING

OLD DOMINION UNIVERSITY

December 1996

Approved by:

_____
Dr. Sacharia Albin (Director)

_____
Dr. Vishnu K. Lakdawala (Member)

_____
Dr. Linda L. Vahala (Member)

_____
Dr. John B. Cooper (Member)

ABSTRACT

OPTICAL FIBER FOURIER TRANSFORM INFRARED
EVANESCENT WAVE ABSORPTION SPECTROSCOPY
OF
ALUMINUM HYDROXIDE AND NATURAL CORROSION

Juock S. Namkung
Old Dominion University
Director: Dr. Sacharia Albin

A new technique for continuous, real-time, in-situ detection of natural corrosion of aluminum alloys is presented. The technique is a generalized version of attenuated total reflectance (ATR) spectroscopy, that combines optical fibers and a Michelson interferometer spectrometer to make evanescent wave absorption measurements. Aluminum hydroxide is one of the major corrosion products of aluminum. Absorption spectra of powdered samples of aluminum corrosion, in the spectral region around three micrometers have been studied and compared with the spectra from pure powdered aluminum hydroxide. A chalcogenide optical fiber was used as an attenuated total reflectance (ATR) optical element. The same samples were studied using conventional ATR spectroscopy, with a zinc selenide crystal optical element as a reference. The corrosion samples are from different aircraft components. The corrosion samples showed spectral features such as positions, widths, and shapes similar to those of aluminum hydroxide. Five spectral features are identified in aluminum hydroxide in the spectral region from 3300 to 3650 cm^{-1}. Two spectral features are identified in the data for aluminum corrosion in the same spectral region. Absorptance was determined in each case. The experimental results from pure aluminum hydroxide and aluminum corrosion agree with the theoretical values. However for the fiber case, those values are lower than theoretical values. This discrepancy is due to the conditions under which radiation is launched into the fiber.

TABLE OF CONTENTS

LIST OF TABLES

TABLE PAGE

LIST OF FIGURES

CHAPTER 1

INTRODUCTION

Material degradation including corrosion may cause damage which can endanger human society and the environment. Therefore, the investigation of material degradation and the development of technology for suitable protection are important. Corrosion is a major problem causing direct economic impact to industry worldwide. Especially for the airline and power industries, corrosion detection and follow-on corrective actions are prime problems in maintaining operational safety. Many attempts have been made by scientists working on nondestructive evaluation (NDE) technologies to develop reliable corrosion detection methods. These methods include various ultrasonic, electromagnetic, and thermal NDE techniques. Application of these techniques usually requires precise structural information of the test components to ensure reliable interpretation of results. Also, simple structural shapes work best with these techniques, but such shapes are not practical in normal operational conditions.

The use of infrared spectrometry and Fourier Transform Infrared Spectroscopy (FTIR) is well established for general-purpose analysis of a wide range of samples. It may be stated that the technique of FTIR is the single most powerful analytical tool for defining an unknown sample. This is because of the ability of FTIR to examine the complex spectral details of solids, liquids, and gases, whether these samples are pure or present as a mixture. But until recently, FTIR spectrometers have not used with optical fibers as components. The ability to make measurements at a remote site as a reaction occurs and monitor continuously by using optical fiber probes offers significant advance in corrosion sensing. The broad spectral coverage of the FTIR measurement technique using a single detector to monitor all spectral elements allows known corrosion products to be monitored and other corrosion products to be detected. The advantages of FTIR spectroscopy as a

measurement technique and the use of optical fibers as remote probes enhance each other when combined and applied to remote sensing and monitoring.

The investigation of optical fiber Fourier transform spectroscopy has increased with the development of new fibers which transmit in the infrared. Fibers are now available which transmit in the 3 to 20 micrometer region and allow transmission over long distances depending on the fiber composition and spectral range of interest.

The development of infrared transmitting optical fibers, such as silver halide[1] or chalcogenide (As-Se-Te) optical fiber[2,3], offers the possibility of significantly improving the sensitivity of the monitoring or sensing technique. The advantage results because more intense fundamental infrared vibrational absorption bands may be monitored rather than much weaker near infrared overtone or combination bands. Chalcogenide optical fiber as an example, transmits well into the infrared beyond a wavelength of ten micrometers. Such fibers are useful for process monitoring or reaction monitoring or spectrochemical quality control.

Remote sensing using optical fibers and interferometers for Optical-Fiber Fourier-Transform Evanescent-Wave absorption Spectroscopy has several attractive features. The multiplex advantage of Fourier-Transform spectrometers with their broad spectral coverage matches well with the broad spectral transmittance properties of multimode optical fibers. As remote probes, optical fibers may be embedded in otherwise inaccessible places so that the sample or process being monitored does not have to be located near the spectrometer. Also, most optical fibers which are clad or coated are relatively strong and flexible and have small bend radii and may be integrated into complex structures. The broad spectral coverage of Optical-Fiber Fourier-Transform spectrometers allows numerous spectral features belonging to different compounds or chemical components in a sample to be monitored simultaneously by evanescent wave spectroscopy.

1.1 OPTICAL FIBER SENSOR

Optical fiber sensors are routinely used for remote sensing applications. Some of the attributes of optical fibers which make them attractive for remote sensing include:

(a) light weight and flexibility,

(b) small physical size and non-intrusive nature,

(c) transmission over broad spectral range,

(d) low radiation attenuation, allowing remote analyses over long distances,

(e) excellent corrosion resistance,

(f) immunity to electro-magnetic interference, and

(g) applicability over a large range of physical conditions of temperature, pressure, stress and strain.

Because of their small size and flexibility, optical fibers may be embedded within complex structures. Also, optical fibers may be used to probe harsh environmental conditions which otherwise can not be reached or monitored.

Fiber optic sensors can be divided into two categories: intensity-modulated and phase-modulated sensor.[4] Intensity-modulated sensors are generally associated with displacement or some other physical pertubation that interact with the fiber. This perturbation causes a change in received light intensity, which is a function of the phenomenon being measured. The light loss can be associated with transmission, reflection, microbending or other phenomena which can be incorporated in the fiber. Phase-modulated sensors compare the phase of light in a sensing fiber to the light in a reference fiber. Phase-modulated sensors use interferometric techniques to detect phase shift of the sensing fiber, which is exposed to a perturbing environment. Phase difference can be measured with extreme sensitivity so phase-modulated sensors are more accurate than intensity-modulated sensors.

1.2 EVANESCENT FIELD

The evanescent field is an exponentially decaying field in the optically rarer medium that results from the presence of a standing wave established at a totally reflecting interface within the optically denser medium. The decaying field in the rarer medium is termed evanescent from the Latin root, *evanscere*, meaning to tend to vanish. This is expressed as the exponential decay of the amplitude of the evanescent field as a function of distance along a normal to the interface in a rarer medium.

Suppose that the radiation propagating in the optically denser medium 1, with refractive index n_1, undergoes total internal reflection at the interface with an optically rarer medium 2, with refractive index n_2, when the angle of incidence θ_i exceeds the critical angle θ_c (see Figure 1a). Then the decrease of the electric field amplitude E_0 at the surface of the rarer medium to some value E, at a distance z from the surface, can be expressed as follows[5,6]:

$$E(Z) = E_0 \exp(-\gamma z), \tag{1}$$

where

$$\gamma = [\, 2\pi (\sin^2 \theta - n_{21}^2)^{1/2} \,] / \lambda_1 . \tag{2}$$

$$= (2\pi/\lambda) \bullet (n_1 \sin^2\theta - n_2^2)^{1/2} \tag{3}$$

Here $\lambda_1 = \lambda/n_1$ is the wavelength of the radiation in the denser medium 1, λ is the wavelength in free space, and $n_{21} = n_2 / n_1$.

When total internal reflection occurs, there is a well known penetration of the evanescent field into the rarer medium, where the field amplitude decays exponentially with distance from the surface. Figure 1b and 1c show standing wave amplitude pattern

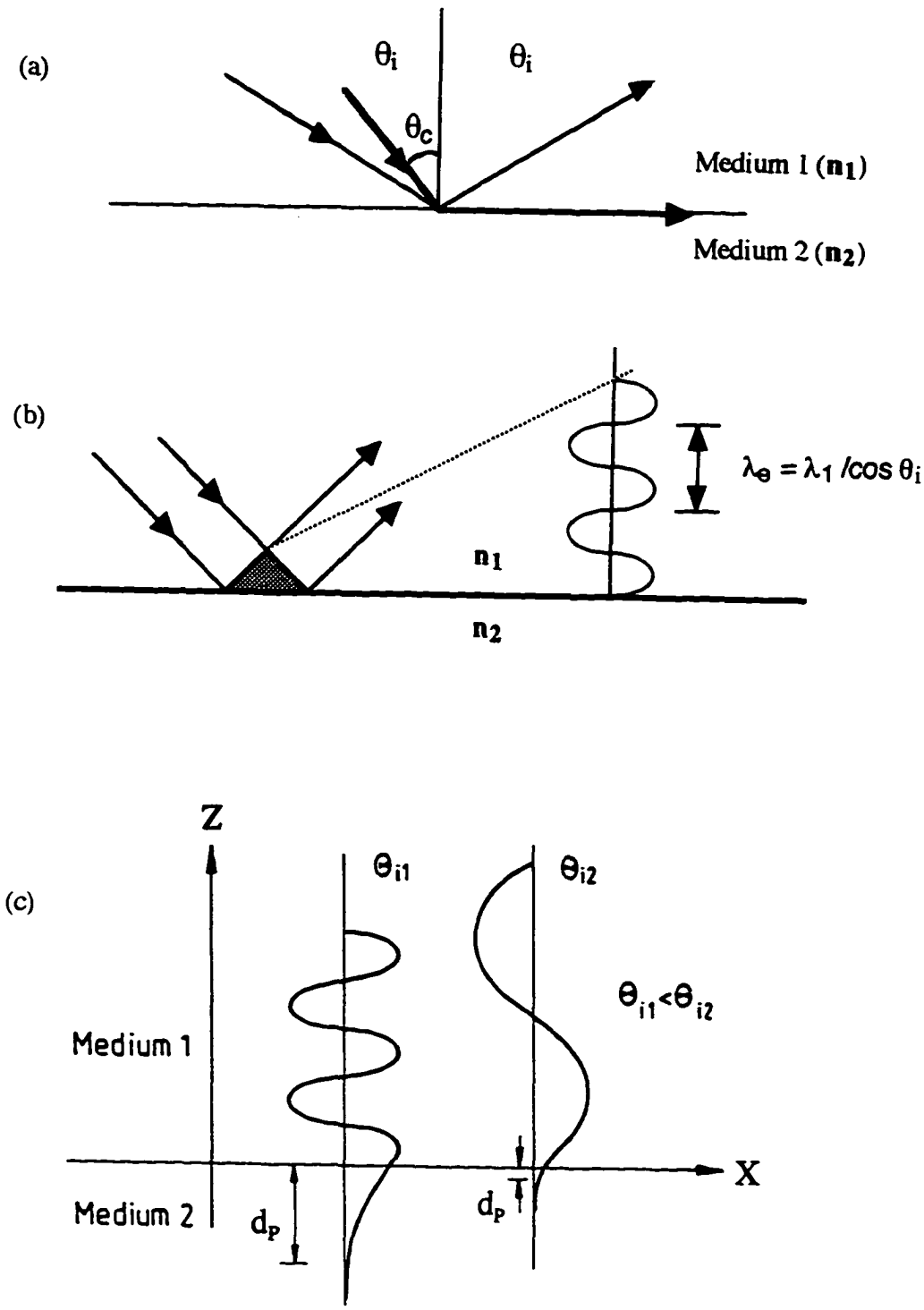

Figure 1. Schematic profiles of evanescent field in total internal reflection for two angles of incidence $\theta_c < \theta_{i1} < \theta_{i2}$.

established near a totally reflecting interface depending on the incident angle θ_i. In this Figure, λ_e is the wavelength of the standing wave established in the denser medium and $\lambda_e/2\pi$ is the reciprocal of the incident wave vector.

The penetration depth, d_p, is defined as the depth at which electric field E decays to a value of $E_0 \exp(-1)$. This occurs at a value of $z = d_p = 1/\gamma$. This parameter is often used as a measure of depth that is sampled in internal reflection spectroscopy (IRS). However, it should be noted that E is not zero at d_p. For $\theta = \pi/2$, one obtains the minimum penetration depth:

$$d_{p,min} = (\lambda/2\pi) \bullet (n_1^2 - n_2^2)^{-1/2} . \quad (4)$$

The decay of the field E/E_0 is a function of penetration depth into a rarer medium. The evanescent field is characterized by the penetration depth as a function of angle of incidence, wavelength, and indices of refraction of the two media.

The penetration depth is the single most defining characteristics of the evanescent field. However for quantitative analyses, the strength or magnitude of the interaction of the evanescent field with the absorbing sample is measured by the effective thickness which will be explained in detail in the theory section. As defined by Harrick [6], the effective thickness is the film thickness required to give the same absorption as that obtained in a transmission experiment. The effective thickness depends on four factors: (a) the penetration depth, (2) the magnitude of the incident electric field, (3) the area illuminated by the incident radiation which depends on $(1/\cos\theta)$, and (5) a refractive index matching factor, which depends on the magnitude of the refractive indices of the two media. Since the dependence of the effective thickness on the penetration depth is linear, the penetration depth is often used as a qualitative reference for evanescent field absorption.

1.3 INTERNAL REFLECTION SPECTROSCOPY

Internal reflection spectroscopy is the technique of recording an optical spectrum of a sample material which is in contact with an optically denser but transparent medium and then measuring the wavelength dependence of the reflectivity at this interface by introducing radiation into the denser medium. In this technique the reflectivity is a measure of the interaction of the evanescent wave with the sample material and the resulting spectrum shows the absorption characteristics of a sample material.[5,6]

Internal reflection spectroscopy requires little or no sample preparation with most types of samples. Materials can be examined in the natural state by bring them in contact with an internal reflection element. Some examples of internal reflection elements are shown on Figure 2 referenced from F.M. Mirabella.[5] It is not even necessary to wet the surface of the element to obtain optical contact. As long as the sample is physically within the penetration depth of the evanescent field from the surface, it is possible to obtain a spectrum of the sample. This method is suitable for a wide range of samples.

There are two different methods of coupling to the evanescent wave and extracting energy from it. In one coupling mechanism some or all of the energy is redirected and there is no energy loss, whereas in the other coupling method the energy is absorbed and there is a loss. These coupling mechanisms give rise to frustrated total reflection (FTR) and attenuated total reflection (ATR), respectively [6].

Attenuated total reflection is due to an absorbing coupling mechanism. The reflectivity of total internal reflection can be continuously adjusted between some value greater than 0 to 100 % by placing an absorbing medium in contact with a reflecting surface. The resulting reflection is said to be attenuated. In ATR spectroscopy a light beam reflecting at a surface with high refractive index penetrates a short distance into the adjoining medium with a lower refractive index. The use of crystals as ATR elements (see

Figure 2), such as germanium, allows an infrared beam propagating inside the crystal to be used to analyze a sample pressed against the surface of the crystal. The sample absorbs the evanescent wave which is just outside the crystal surface. The amount of absorption by the sample may be controlled by adjusting the number of bounces of the radiation as it propagates through the crystal. Attenuated total reflection is observed when the angle of incidence remains above the critical angle and the wavelength is swept through an absorption band.

Using a crystal as a ATR element have many advantages as a reference or a standard technique. Some of the advantages include:

(a) large cross section area and large throughput,

(b) large sample surface area in relation to its length,

(c) flat optical surface,which means that no skew ray contribution as in cylindrical optical fiber,

(d) well defined optical path through crystal,

(e) Same reflection angle for all rays.

With these advantages and enhanced sensitivity, a crystal ATR element has become a powerful tool to identify sample materials. Since a crystal ATR element has well defined optical path, the spectral data collected using a crystal is easier to analyze and determine optical parameters. Consequently, the technique can serve as a reference for comparison with the spectral data collected using optical fiber as an ATR element.

1.4 INFRARED TRANSMITTING MATERIALS

Infrared transmitting materials were mainly used as window materials for infrared spectroscopy in early stages of research. Infrared transmitting materials have, in general, small force constants and large masses of constituent atoms to obtain an excellent

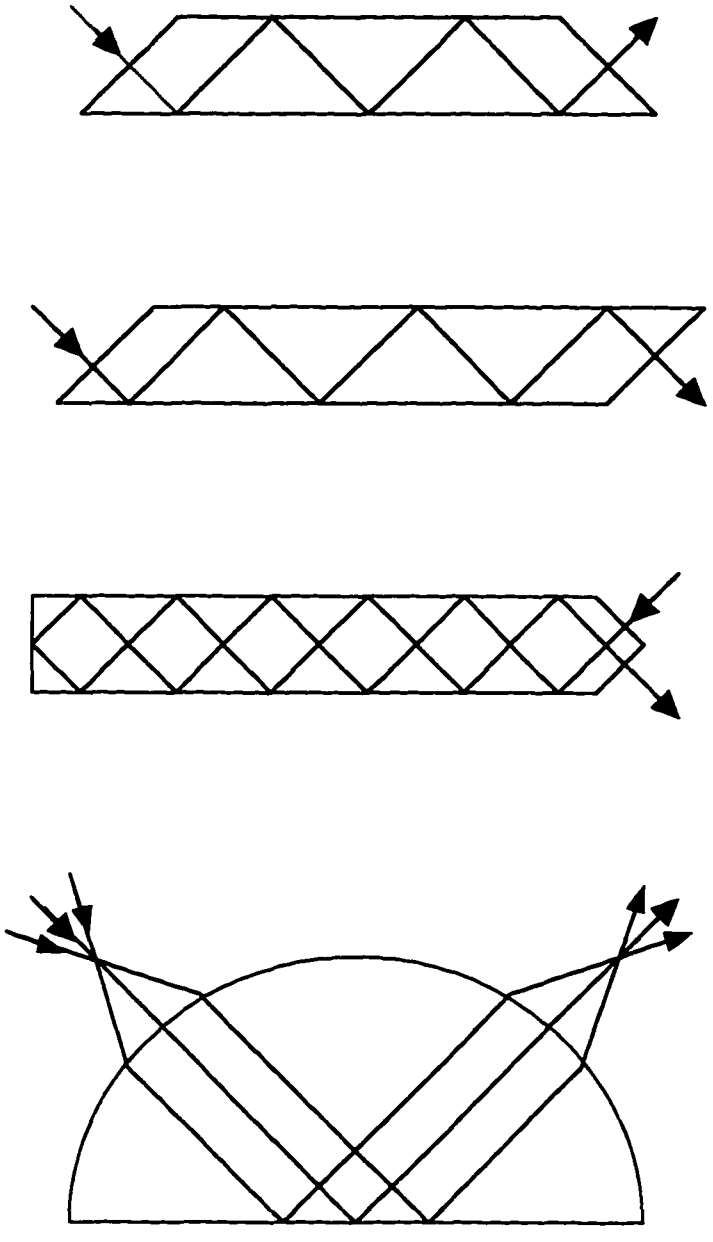

Figure 2. Some samples of internal reflection elements.

transparency in the infrared region. The materials are therefore relatively soft and usually contain heavy metals. Infrared transmitting materials can be classified into crystalline and glass forms.[7] Crystalline forms consist of oxides, halides, semiconducting elements, chalcogenides and intermetallic compounds. Glass forms are classified into oxides, halides, and chalcogenides. Typical materials of each category are shown in Table 1.

1.4.1 CRYSTALLINE MATERIALS

The transparent region of oxide crystals falls below 10 μm, and the region widely used for infrared optical transmission is mostly within 4 μm. Typical oxides are SiO_2 (quartz), Al_2O_3 (sapphire), TiO_2 (rutile), and MgO. Of these oxides, SiO_2 is usually used in glass form. Halide crystals have very wide transparent region ranging from the ultraviolet to far beyond 10μm. These materials are widely used as infrared optical transmitting window. The refractive indices of halide crystals are relatively small, resulting in small Fresnel reflections. However their solubility in water is large compared to other materials such as oxides. Typical halides are LiF, CaF_2, MgF_2, NaCl, KCl, KBr, CsBr, CsI, AgCl, KRS-5, and KRS-6. KRS-5 and KRS-6 are polycrystals composed of TlBr-TlI and TlBr-TlCl, respectively.

Diamond (C), silicon (Si), germanium (Ge), selenium (Se), and tellurium (Te) can be classified into semiconducting elements. One disadvantage of Si and Ge is that they show large Fresnel losses due to large refractive indices. Also, transmittance degradation occurs at temperature above 200°C. Chalcogenide are composed of chalcogen elements, which are S, Se, Te, and elements such as Zn, Cd, and Pb. Intermetallic compounds are defined here as the compounds between IIIb elements (such as Al,Ga, and In) and Vb elements (such as P, As and Sb). GaAs and InP are well known light emitting materials.

Table 1. Infrared materials

Form	Group	Materials
Crystal	Oxide	SiO_2, Al_2O_3, TiO_2, MgO, $SrTiO_3$, $BaTiO_3$ SiO, BeO, CaO, $LiAl_5O_8$, etc.
	Halide	LiF, CaF_2, MgF_2, NaCl, KCl, KBr, CsBr, CsI, AgCl, KRS-5, KRS-6, etc.
	Semiconductors	C(diamond), Si, Ge, Se, Te, etc.
	Chalcogenide	ZnS, CdS, ZnTe, CdTe, ZnSe, PbS, PbSe, PbTe, etc.
	Intermetallic Compound	AlP, AlAs, AlSb, GaP, GaAs, GaSb, Inp, InAs, InSb, etc.
Glass	Oxide	SiO_2, GeO_2, GeO_2-Sb_2O_3, TeO_2-ZnO-BaO, etc.
	Halide	$ZnCl_2$, BeF_2, AlF_3, ZrF_4 systems, HfF_4 systems, ThF_4-BaF_4, etc.
	Chalcogenide	As-S, Ge-S, As-Se, Ge-Se, Ge-As-Se, Ge-Sb-Se, Ge-Se-Te, As-Se-Te, etc.

InSb and InAs are used as materials for infrared light detecting devices. The transparent regions for these compounds reach up to 10 μm. Some of the optical and physical properties of crystalline materials are shown in Table 2.

1.4.2 GLASS MATERIALS

The typical oxide glass is the amorphous form of silica. The infrared properties are as good as those of crystalline SiO_2, with a transparent region between 0.15 and 4.5 μm. Heavy metal oxide glasses are preferable for infrared transmitting materials. The advantage of heavy metal glasses such as GeO_2 glass is that infrared absorption due to lattice vibration can be shifted toward the longer wavelength. This leads to the ultra-low loss in the infrared region. The most extensively studied halide glasses are fluoride glasses such as BeF_2, AlF_3, and ZrF_4: ZrF_4-based and HfF_4-based glasses are the materials most used as optical fiber with their high compositional flexibility.

Infrared transparent glasses may be formed from the materials such as arsenic, germanium, and antimony combined with heavier elements in the oxygen family which include sulfur, selenium, tellurium . The vitreous materials derived from such compounds are known chalcogenide glasses. The electronic absorption edges of chalcogenide glasses are in the visible, or near infrared region. Generally the transmission of typical bulk chalcogenide glass specimen may extend to the 10-15 μm region of the infrared. These materials have refractive indices near 2.5, and low transition temperatures (200-300°C).

1.5 CHALCOGENIDE OPTICAL FIBER

Optical materials studied to date for infrared transmitting fibers are heavy metal oxides, halides, and chalcogenides. Chalcogenide glasses are defined as glasses containing at least one of the elements from S, Se, and Te. The infrared absorption edge shifts toward

Table 2. Properties of typical crystalline materials

Group	Material	Transparent region (μm)	Refractive index at 4 μm	Density (g/cm^3)	Melting point (° C)	Water solubility (g/100g at 20°C)
Oxides	SiO_2	0.12-4.5	1.53 (2μm)	2.65	1743	< 0.001
	Al_2O_3	-5.5	1.73	3.98	2030	$9.8x10^{-5}$
	TiO_2	-6.0	2.45 (4.3 μm)	4.26	1825	insoluble
	MgO	-6.8	1.71	3.59	2800	$1.2x10^{-5}$
Halides	CaF_2	0.13-9	1.41	3.2	1360	0.0017
	KBr	0.21-27	1.54	2.8	730	53.5
	AgCl	0.21-5	2.0	5.6	458	1.5x10-4
Semiconducting elements	Si	1.2 -15	3.43	3.2	621	44
	Se		3.7	4.82	490	<0.005
	Te	3.5 -8.0	6.3	6.25	725	< 0.005
Chalcogenide	ZnSe	0.5 -22	2.58 (2μm)	5.65	1373	<0.001
	PbS	3.0-7	4.15	7.5	1387 (° K)	
Intermetallic compound	InSb	7.0 -16	4.0 (10μm)	5.78	523	0.00

longer wavelengths as the atomic number increases, and so it is necessary to choose the chalcogen elements whose atomic numbers are large for transmitting longer wavelength light. Chalcogenide fibers with many different combinations of these compounds are manufactured and characterized for various applications.[8,9]

One of the applications of infrared optical fibers is for long distance communications. Single mode optical fibers are used for this purpose since it is required of ultra-low loss transmission and small material dispersion. The other use of infrared optical fibers is for the various remote sensing systems. The uses of infrared fibers are particularly advantageous because these fibers can transmit longer wavelength light over wide transparent wavelength regions. It is often necessary to measure infrared spectra of various molecules in a chemical analysis. Optical fibers were used for this research to detect $Al(OH)_3$ compound related with corrosion sensing.

Chalcogenide glass infrared fibers exhibit higher loss than crystal infrared fibers. The fibers used for this research are manufactured by Amorphous Materials Inc[10], in Texas. In order to reduce the losses, Tellurium, which is a heavier atom, is substituted partially in place of the Se from As-Se chalcogenide fiber. The core glass is a As-Se-Te glass composition and was pulled by a sealed chamber method.[11] It is also reported that the fibers from the As-Se-Te system were more flexible than others such as As-S and Ge-S glasses. Details of physical properties of As-Se-Te core glass fiber are listed in Table 3 referenced from A. R. Hilton [12].

Table 3. Properties of As-Se-Te core glass fibers

Core Glass	As-Se-Te
Glass Transition	136 °C
Softening point	170 °C
Thermal Expansion	23.5×10^{-6} /°C
Transparent region	2-11 μm
Refractive index	
at 4μm	2.82
10μm	2.81
Thermal change in index	3×10^{-5}/°C
Fiber absorption	
at 5.25 μm	0.7
9.27μm	0.8
10.6 μm	4-5
Numerical aperture	
unclad (est.)	0.7
clad (est.)	0.7
Bending Radius	
30 mil Diam.	1.5/0.4 clad
20 mil Diam.	0.3
10 mil Diam.	0.2

CHAPTER 2

OPTICAL FIBER FTIR SPECTROSCOPY

Fourier transform spectroscopy using optical fibers for remote sensing includes several techniques. The technique to be employed here is based on absorption of the evanescent field which is present at the interface between the fiber and the surrounding medium. The compound to be studied is detected directly from its evanescent wave absorption spectrum. Absorption of the evanescent field is described in section 1.3 for the theory of Attenuated Total Reflection (ATR) spectroscopy.[13]

In conventional ATR spectroscopy short solid crystals, a few centimeters in length, have been used as the ATR optical element. The technique can be used for the study of liquids, solids, pastes and thin films. The technique in the conventional form has been reviewed by Harrick [6,14]. The conventional ATR spectroscopy is not suitable for remote measurement. The disadvantage of ATR crystals is that they are rigid and also only short crystals may be used since ATR crystals must be incorporated within the spectrometer. For example, the ATR crystal must be collocated with the spectrometer in order to be integrated in the instrument optical path.

Many potential applications of infrared analyses using an ATR element were impractical or impossible due to the requirement that the sample be brought inside or in close proximity to the spectrometer. A certain amount of remote sensing may be accomplished by directing the radiation beam out of the spectrometer, through the sample, and then onto a detector. But many potential applications remained outside the scope of infrared analyses, because of the difficulty in getting the infrared beam to the sample. This includes samples that are too hazardous or too large to bring into the laboratory, or industrial processes occurring inside reactors or furnaces. Very often reactions cannot be conveniently monitored by conventional techniques.

The use of optical fibers as light pipes and as ATR elements can, to a large extent, solve these problems completely. Very long optical fibers can guide radiation far from the spectrometer, to a remote location. Integrated systems, combining optical fibers and interferometers, have broad spectral coverage. These systems overcome the problem of directing the radiation beam to distant samples or processes which is to be monitored or analyzed and then back to the spectrometer detector.

Optical fiber is also advantageous for monitoring samples that are part of a time dependent process and can not be brought to the spectrometer. The use of fibers has extended the range of samples that may be analyzed. The small size of fibers also means that intrusion into the process being monitored is minimal. The small size combined with the flexibility of long fibers to reach remote processes, offers the possibility of simple, continuous, real-time, in-situ remote sensing. Consequently, researchers have increasingly considered the possibility of using long optical fibers as ATR optical elements.

Optical fibers are becoming important in many areas of remote sensing, and also in communications, because of their low attenuations, which result in small signal loss over long fiber lengths. However, fiber attenuations are wavelength dependent, and there are spectral regions where fibers have large radiation losses. If optical fibers are to be used for remote spectroscopic applications, the spectral properties of the fibers must be known. Until recently, very little attention has been given to the spectral attenuation of optical fibers, particularly infrared transmitting fluoride glass and chalcogenide fibers which have been developed within the last few years.

2.1 PREVIOUS RESEARCH

The earliest research into the spectral characterization of infrared transmitting optical fibers has occurred within the last ten years and includes the studies of Frank et al. [15],

Fredricks et al.[16] and Wright et al.[17] These researchers used Fourier transform infrared spectroscopy to spectrally characterize near-infrared transmitting silica-core optical fibers. They considered the optical arrangements necessary to integrate the optical fiber into the optical path of the interferometer spectrometer. They measured the attenuation of transmitting silica-clad and plastic-clad silica-core multimode optical fiber over the infrared and near infrared spectral range. Their measurements concentrated on the spectral distribution of attenuation in the near-infrared range. Only later did researchers consider the important question of loss of throughput when an optical fiber is incorporated into the spectrometer optical path.

Among the earliest examples of the applicability of optical fibers for evanescent wave absorption spectroscopy are the studies of DeGrandpre and Burgess.[13,18] They used polymer-clad silica-core fiber to construct a near-infrared evanescent wave absorption probe. They constructed their probe by coiling approximately 1.5 meters of 400 micrometer core-diameter fiber onto supports of varying radii, small enough so that bending does affect the magnitude of the evanescent field. Their experiments covered the near infrared spectral range. The siloxane fiber cladding provided a protective layer for the fiber core. Sensor selectivity was obtained because only certain solvents penetrated the cladding, reaching the fiber core and absorbing the evanescent field.

Katzir et al.[19] used unclad infrared transmitting silver halide optical fiber as ATR elements for optical fiber FTIR evanescent wave absorption spectroscopy. These fibers cover the spectral range from 1 to 20 micrometers wavelength. Their first experiments demonstrated the feasibility of performing ATR absorption experiments with unclad silver halide fiber. They recorded spectra of selected liquids, including water, acetone, and glycine. In subsequent experiments[20,21] they made quantitative measurements of relatively well known materials, studying absorption features with known transition intensities.

Known spectroscopic features were qualitatively recognized with sample quantities as small as six nanograms. This demonstrates that the technique is very sensitive. They found that sample absorbance was linear up to sample coating thicknesses around the core of about 0.9 micrometers. This corresponds approximately to the limit of the penetration depth of the evanescent wave.

Katz et al.[22] have also used chalcogenide optical fiber to make evanescent wave absorption measurements of isopropanol. They also performed calculations of the evanescent wave attenuation by the isopropanol, under several restrictive assumptions. In particular they assumed that all of the radiation was launched into the fiber at small angles to the fiber optical axis, so that the penetration depth is not great and the attenuation is small, and is thus a linear function of the absorber amount. They also assumed a uniform distribution of radiation intensity within the numerical aperture of the fiber. Under these conditions they were able to obtain qualitative but not quantitative agreement with the observed spectral data. Their results confirm that additional research is still needed before quantitative analyses of evanescent wave absorption spectral data using optical fibers is possible.

2.2 SCOPE OF THIS RESEARCH

The purpose of this research is to demonstrate that the technique of Attenuated Total Reflectance (ATR) spectroscopy using a combined optical-fiber-FTIR-interferometer spectrometer can be applied to the study of powdered solid samples. In particular, the technique has been used to collect spectra of powdered samples of natural corrosion of aluminum alloy. Also, spectra of pure powdered aluminum hydroxide, which is a principal corrosion product of aluminum, has been collected using this technique.

The research has three major objectives : first, is to demonstrate that consistent, reproducible spectral data of powdered samples can be obtained using optical-fiber-FTIR-ATR spectroscopy. This step is essential in establishing that the technique may in the future be applied in practical applications with confidence in obtaining consistent results. ATR spectroscopy using an optical-fiber-FTIR spectrometer has been demonstrated in qualitative studies of liquids. Some simple quantitative results have also been reported. However, there is no record in the literature of the technique being applied to solids or solid powdered samples. Aluminum hydroxide, $Al(OH)_3$, and naturally occurring corrosion of aluminum alloy has been investigated.

Second, the dependence of the spectral transmittance or absorbance as a function of the instrumental and optical fiber parameters will be demonstrated. This aspect of the study is necessary to establish that instrumental effects can be accounted for and will not bias, with systematic errors, results inferred from the spectral data. The absorbance depends on several experimental parameters, including the fiber diameter, the angle of the acceptance cone, and the length of fiber in contact with the sample. Spectral data will be collected to confirm that the dependence of the absorbance on the instrumental parameters is as predicted by theory.

As an aid in quantitative analyses and also as a reference, spectral data will be collected using a seven bounce zinc selenide crystal as an ATR element. Since the crystal ATR element has a simple geometry and the radiation optical path is the same for all rays and is well defined, this application of the technique can serve as a standard. The experimental results from the two different applications of the technique, using optical fiber and zinc selenide crystal ATR elements, will be compared. From the data collected using the zinc selenide crystal ATR element, a frequency dependent absorption index for aluminum hydroxide and natural corrosion will be obtained. The inferred absorption index

can then be used to predict the absorbance that will be obtained using an optical fiber: the predicted absorbance will be compared with the experimental absorbance data. Because samples of natural corrosion can be mixed with contaminants such as sealer, glue, primer, and paints, the portion of the analyses using pure powdered aluminum hydroxide will serve as a reference standard.

To support data analyses theoretical expressions have been derived, that describe the absorbance as a function of the refractive index, absorption index of a sample, and the experimental parameters. The theoretical results are useful in two ways: first, applying the theoretical result to the two different geometries, using a crystal ATR optical element and using optical fibers as ATR elements, allows the two ways of collecting data to be compared. This will enhance the usefulness of the conventional ATR method (using a crystal optical element) as a reference and calibration technique for the method employing an optical fiber. Also, in applications by comparing the measured absorbance using optical fiber to the derived expression, an experimental estimate of the absorber amount of sample material can be obtained. This means that identification of the sample and determination of sample amount could be obtained in situ without bring the sample to the lab to use the conventional (crystal) ATR method.

Third, new results will be obtained from the spectral data which is collected for aluminum hydroxide and natural corrosion. These two compounds are important in industrial monitoring of corrosion. These new results will be in the form of spectra, absorbance data and experimental absorption coefficient data over the spectral range of significant sample absorption, from approximately two to twelve micrometers.

Two other important empirical quantities will be determined. One is the minimum amount of sample that can be detected, given the instrumental sensitivity or signal to noise ratio (SNR) of the experiment. The other is the dependence of the sample absorbance as a

function of the length of optical fiber in contact with the sample. Of particular importance is the slope of the curve which determines how the sample absorbance changes with the length of fiber covered, the sample amount, and whether or not the curve is linear and has zero intercept. A positive intercept would indicate experimental uncertainty. A negative intercept would indicate an instrumental bias, in addition to the possibility of experimental uncertainty.

Also, it should be noted that the ability to collect spectra of solid powdered samples using optical-fiber-FTIR evanescent wave absorption spectroscopy will demonstrate, by itself, that the technique can be employed for the purpose of continuous, real-time, in-situ remote chemical sensing.

CHAPTER 3

CORROSION CHEMISTRY

Corrosion is a material deterioration process of metallic structures. Deterioration occurs in the form of mechanical damage such as abrasion, galling, wear or fatigue, which depends primarily on the design of the structure. Also, deterioration depends on the design of the structure, the materials used for fabrication, and on the chemical nature of the operating environment. Corrosion manifests itself in many ways including rusting, pitting, tuberculation, cracking, and so on. It is a costly and wasteful process. Even though knowledge of engineering design, material science, and corrosion theory has improved, corrosion costs have continued to escalate in industry. Especially for the airline industry, corrosion is a major concern of operational safety.

Metals are seldom found in their elemental state in nature. They usually exist as compounds, such as oxides, hydroxides, carbonates, and nitrates which are fairly stable. Most pure metals and alloys are not stable and tend to revert back to natural state by combining with elements in the atmosphere to form stable compounds. The chemical reactions by which metals revert back to their natural states are known as corrosion reaction.

Corrosion reactions can be understood if the system is fully described in terms of the thermodynamics, electrochemistry, physical chemistry, and metallurgical conditions of the metal involved.[23] Thermodynamics is based on the knowledge of the equilibrium conditions of the system and can be used to see whether a chemical change is energetically feasible. Electrochemistry can be used to describe the transfer of electrons in the system and to predict reaction products that will be produced. Metallurgy is able to describe the internal structure of the metal involved, in terms of alloying elements and alloy phase that may affect local electrochemical conditions at an exposed surface. Finally physical

chemistry can provide information on the surface conditions of the reactant and can describe the physical sites where the electrochemical reactions may occur.

Climate is one of the major factors affecting corrosion since it introduces the two important variables of temperature and humidity. High temperature generally increases the rate of corrosion attack on metal surface since corrosion reactions are thermally activated. Water vapor in the atmosphere can lead to a formation of thin films of water on metal surfaces. The moisture will provide an electrically conducting medium to create electrolytic cells which allow rapid corrosion to occur. This is known as the atmospheric corrosion. According to the mechanism of corrosion processes, which depend on the nature of the surrounding media with which metals react, corrosion can also be simplified into wet and dry corrosion.[23]

3.1 DRY CORROSION

Dry corrosion involves a metal/gas or metal/vapor reaction, where non metals such as oxygen or halogens lead to the formation of a film or scale on the metal surface without intervention of a liquid electrolyte. When a metal combines with the atoms or molecules of a gas it loses electrons and an oxidation reaction has occurred. At the same time the electrons must be accepted by the non-metal involved, which is said to be reduced. Therefore oxidation involves a transfer of electrons and may be considered as a electrochemical process. The overall reactions can be described by two separate reactions occurring simultaneously:[23,24]

Metal $\rightarrow M^{n+} + n$ electrons	oxidation
Oxygen $O_2 + n$ electrons $\rightarrow (n/2)\ O^{2-}$	reduction
$M + O_2 \rightarrow MO_{n/2}$	combination

These are called oxidation-reduction reactions. The films or scales produced by corrosion will affect the corrosion process, since they will tend to form a barrier between the metal and the corrosive environment.

Various results may occur if the oxides or other corrosion products fail to protect the underlying metals. The oxides may react chemically or combine with water to produce films that are not impervious to the passage of oxygen. If the volume of oxide is less than the volume of the metal, then the oxide may not give proper protection from the start. If the volume of oxide is much higher than the volume of the metal, large stresses will be set up in the oxide and cracking may occur. Also the oxide may volatilize as the temperature increases, or the protective film may be mechanically damaged due to impact from foreign objects, such as stone or sand. As a result of the above considerations, corrosion rates may not decrease with time as expected after the formation of the oxidation.

3.2 WET CORROSION

Wet corrosion involves a liquid phase where electrically conducting solution is present to assist in the transfer of metal ions and electrons between the oxidizing or anodic site of metal and reducing or cathodic site.[23,24] The corrosion reaction is therefore an electrochemical process and is called wet corrosion. For corrosion to occur, the presence of all the components of an electrochemical cell are required. These components are an anode, a cathode, a metallic path for the conduction of electrons, and conducting solution (electrolyte) between anode and cathode. An anode and cathode are sites on metals that have a potential difference between them. If any one of these components is absent, a corrosion cell does not exist and no corrosion will occur. Figure 3 shows a very simple illustration of a corrosion cell. Corrosion cell can also be produced by the interaction of small, local adjacent anode and cathodes on the same piece of metal.

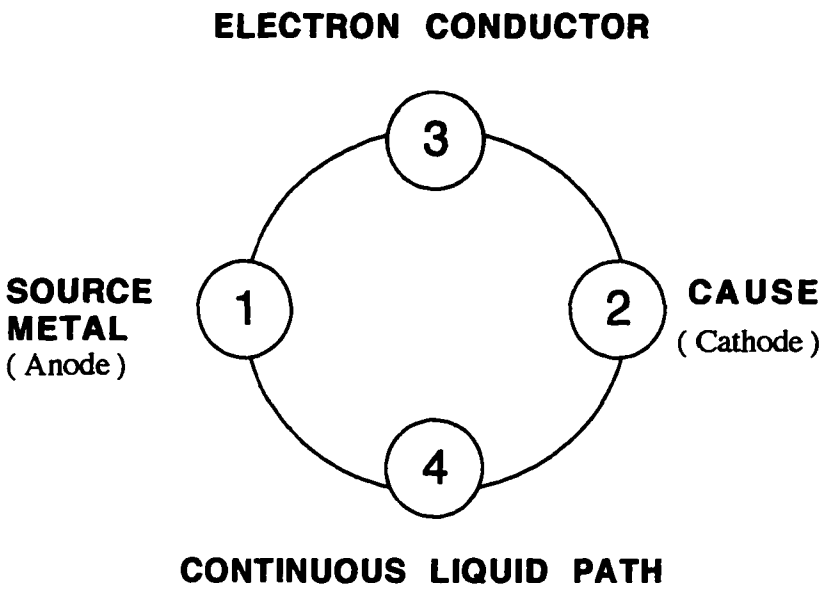

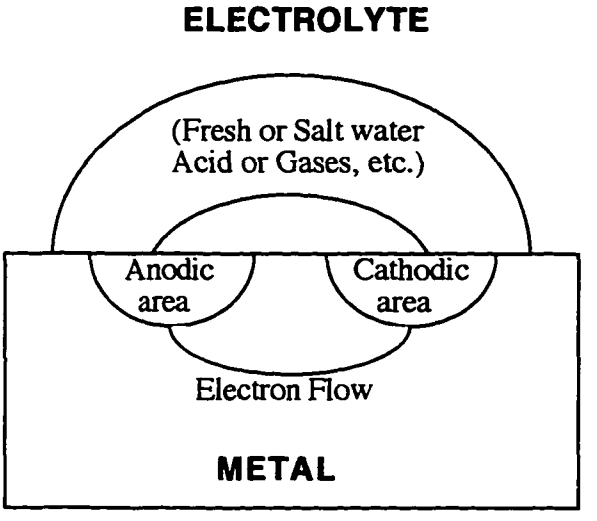

Figure 3. Simplified corrosion cell.

Electrochemical corrosion processes with balanced anodic and cathodic reactions occur in acidic electrolytes or neutral electrolytes such as water. The anodic reaction will involve oxidation (corrosion) of the metal with lower galvanic potential, but the cathodic reaction will usually be the reduction of oxygen dissolved in the electrolyte. Figure 4 illustrates the general features of a galvanic cell indicating the direction of current and electron flow. The electrode processes can be expressed chemically as: [23]

Anode reaction $M \rightarrow M^{2+} + 2\,e^-$

where M is divalent metal,

Cathode reaction in acidic electrolyte $2H^+ + 2\,e^- \rightarrow H_2$

Cathode reaction in a neutral electrolyte $O_2 + 2H_2O + 4\,e^- \rightarrow 4\,OH^-$

The net direction of the reaction depends on the electrode potentials generated by each electrode for the reactions that they sustain. A knowledge of electrode potential of a metal or alloy, relative to another in a given solution may be sufficient to provide an indication of corrosion susceptibility. Table 4 shows some examples of the relative potentials of metals and alloys in sea water.[23,25] A metal appearing high in the table would generate a high (negative) electrical potential with respect to a second metal standing lower in the table. Therefore it would behave anodically and would corrode when coupled to the second metal and immersed sea water. It should be noted that the term ' high potential end', in this table indicates a high negative potential.

One of the purposes of this research is to detect corrosion in aluminum structures which are major components of aircraft. Corrosion in aircraft is directly related to its operational safety so early detection of corrosion is a major concern of airline industry. Corrosion damage generally increases with time and, as aircraft becomes older the effect of

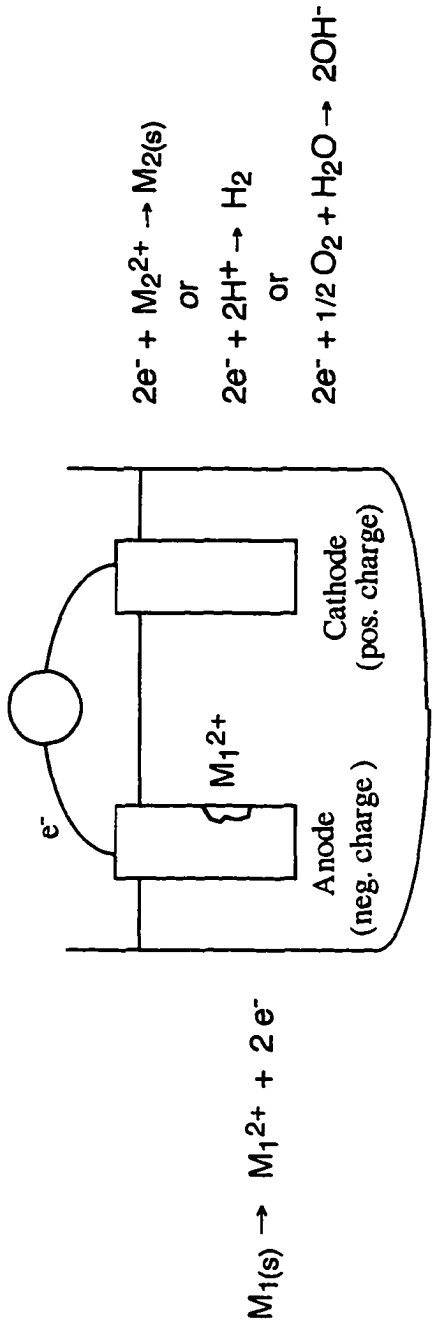

Figure 4. Features of a galvanic cell.

Table 4. Grouping of materials and alloys

Anode
Magnesium Magnesium alloys Beryllium Aluminum Zinc Galvanized steel Aluminum alloys Chromium Gallium High Potential end ▲ Cadmium Indium Cast Iron lead Tin Solder Lead Tin Cobalt Nickel Inconel (Ni, Cr, Fe) Brass Antimony Copper ▼ Low Potential end Titanium Monel (Ni, Cu) Bronze (Cu,Zn,Sn) Silver Solder Nickel Copper (70-30) Stainless steel (passive) Silver Palladium Gold Rhodium Platium Carbon
Cathode

corrosion will become more severe. If corrosion damage is not detected early and repaired, it may eventually become a serious hazard to the structural integrity of the aircraft.

3.3 CORROSION IN ALUMINUM

Aluminum possesses extremely valuable physical properties such as good electrical and thermal conductivity, and good corrosion resistance. Pure aluminum is soft and lacks strength but it can be alloyed with other elements to increase strength and impart a number of useful properties. Table 5 shows some of physiochemical properties of pure aluminum. With its low density, aluminum is used in many structural applications and in transportation where weight saving is an important consideration. Even though aluminum is one of the most reactive metals, it is often resistant to corrosion in practice since it is protected by oxide films which form rapidly in most environments.

Corrosion resistance of pure aluminum depends on the conditions under which corrosion occurs. Aluminum is corrosion resistant to media in which the protective oxide film can persist; it is not resistant to media in which this protective oxide layer is destroyed or can not be formed. Pure aluminum is corrosion resistant to a normal atmosphere and can be used without additional protection, but it corrodes in the heavily polluted atmospheres of industrial towns many times faster than in pure air and should not be used unprotected. In most of cases, aluminum alloys possess a lower corrosion resistance than pure aluminum. With these enhancement of properties, aluminum alloys are used in industry to a much greater extent than pure aluminum.

The corrosion behavior of aluminum alloys is strongly influenced by the chemical composition of the alloys as determined by impurity elements and alloy additions, since these affect the electrolytic solution potential of the alloys. The aluminum alloys most widely used in aircraft structures are Al-Cu-Mg type (2xxx series) or Al-Zn-Mg type (7xxx

Table 5. Physiochemical properties of pure aluminum

Property	Value
Atomic number	13
Atomic weight	26.98
Crystal structure	Face-centered Cubic
Density at 25° C	2.698 g/cm^3
Melting point	660.37 ° C
Boiling point	2494°C
Specific Heat at 25 °C	0.215 cal/g°C
Thermal conductivity	0.566 cal/(cm s °C)
Thermal Expansion Coefficient	23 x10^{-6}/°C
Thermal diffusivity	0.969 cm^2/s
Electrical resistivity	2.7 μΩ-cm
Reflectivity	85-90%
Hardness	2-2.9 Mohs

series) alloys.[23] Alloys of the 6xxx series , Al-Mg-Si systems, such as 6061 are also used to a lesser extent. The reactive element of zinc and magnesium decreases the solution potential of aluminum while copper has the opposite effect on the solution potential. The rate of corrosion is proportional to the amount of current that flows in the corrosion cell, which depends on the solution potential.

A great deal of information has been collected in recent years to demonstrate that environmentally induced failure process may often be the result of hydrogen damage rather than oxidation. Due to small size and mass, atomic hydrogen has high diffusivity in most metals. Therefore it will penetrate most clean metal surfaces quite easily and migrate rapidly to favorable sites where it may react with base metals or with its alloying element to form hydrides. The corrosion products of aluminum, aluminum oxide and its hydrates are given in Table 6.[26,27]

The natural form of aluminum oxide, Al_2O_3, is called corundum. This mineral occurs in various colors and crystallizes in hexagonal structure. Ruby and sapphire are the gem varieties of this material. Hydragillite, one of the natural forms of aluminum trihydrate, is a white or tinted mineral crystallizing in a monoclinic system. It can be written as $Al_2O_3 \cdot 3\ H_2O$ or $Al(OH)_3$. Bayerite has similar structure as hydragillite. In bayerite the layers are arranged closely so density is higher than in the case of hydragillite. Boehmite, one of the natural forms of aluminum oxyhydrate which is expressed $Al_2O_3 \cdot H_2O$ or AlO(OH), is an orthorhombic mineral and comes with grey, brown or red color. Aluminum hydroxide, $Al(OH)_3$, is a white powder and a major corrosion material of aluminum.

Many alloys used in airframe and engine construction are affected by hydrogen embrittlement, including steels, aluminum, and titanium. And evidence shows that

Table 6. Aluminum Oxide and its Hydrates

Name	Symbol
Hydragillite	$Al_2O_3 \cdot 3H_2O$
Bayerite	$Al_2O_3 \cdot 3H_2O$
Boehmite	$Al_2O_3 \cdot H_2O$
Corundum	Al_2O_3
Aluminum Hydroxide	$Al(OH)_3$

hydrogen embrittlement contributes to the stress corrosion cracking.[23] The source of hydrogen in these embrittlement studies is believed to be the reaction between aluminum and water, which produces a duplex film consisting of aluminum oxyhydride (AlOOH) and aluminum hydroxide [$Al(OH)_3$]. This reaction has been written: [23,28]

Anode $$Al + \begin{Bmatrix} 3\,H_2O \\ 2\,H_2O \end{Bmatrix} \rightarrow \begin{Bmatrix} Al\,(OH)_3 \\ Al\,OOH \end{Bmatrix} + 3H^+ + 3\,e$$

Cathode $$3\,H_2O + 3\,e \rightarrow (3/2)\,H_2 + 3\,OH^-$$

Many different ways of inspecting corrosion have been developed depending on the materials including visual inspection. The appearance of corrosion on unpainted surfaces may be in the form of deposits or spots. This occurs around skin seams, either lap and butt joints, areas where sand and dirt collect, and in crevices or joints where traces of chemicals such as cleaning compounds or corrosion removal compounds have collected.[23,25] Particular attention must be paid where moisture does not rapidly evaporate. For aluminum alloys, white or greyish powder is the proof where corrosion exist and means aluminum hydroxide is present.

CHAPTER 4

THEORY

The propagation of radiation through an optical fiber and absorption of evanescent field energy by a sample surrounding a fiber core is described in this chapter. It is assumed that the fiber diameter is large compared to the wavelength of the propagating radiation, so that ray optics are applicable and diffraction effects do not have to be considered. This is a very good approximation for the results reported here. In addition, it will also be assumed that the rays entering a fiber are meridional rays only. The rays which cross the fiber axis between reflections are known as meridional rays and the rays which never cross the fiber axis are called as skew rays.[29,30]

4.1 ACCEPTANCE CONE HALF ANGLE

The use of a fiber as a waveguide is based on the phenomenon of total internal reflection. An example of meridional ray path along the optical fiber is illustrated in Figure 5a. Radiation can propagate by total internal reflection only if the sine of the angle of incidence θ at the fiber core and cladding interface exceeds the index ratio of core n_{Cl} to cladding n_{CO}, (see reference 30):

$$\text{Sin}\ \theta \geq (n_{Cl}/n_{CO})\ . \qquad (5)$$

This means that n_{CO} should be greater than n_{Cl} for propagation along the fiber. Figure 5b illustrates the maximum angle launched at the boundary between air and fiber core, which is called acceptance cone half angle, in which radiation may propagate through the fiber as a wave guide.

Radiation can be launched into an optical fiber only within an acceptance cone of half-angle θ_{AC} measured with respect to the optical axis of the fiber. This angle may be

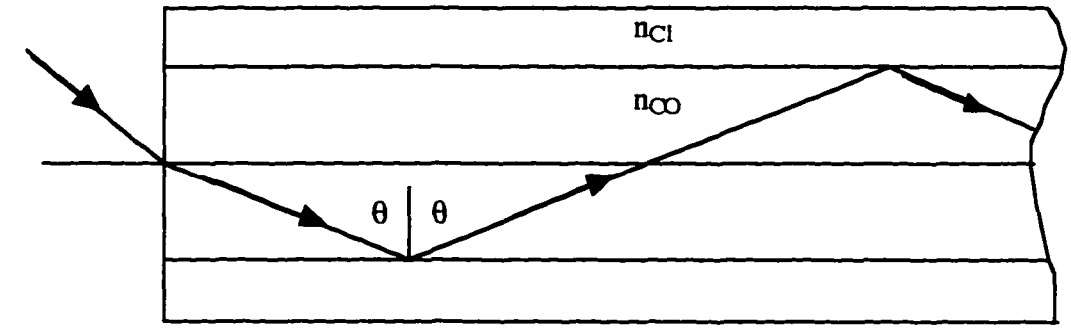

(a)

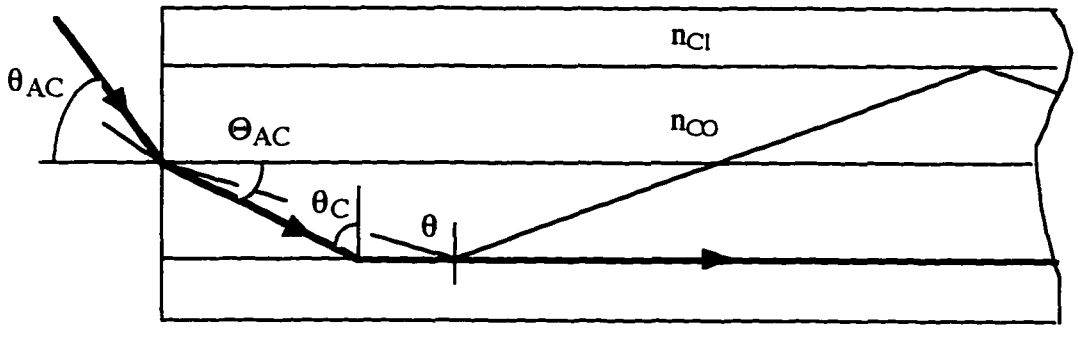

(b)

Figure 5. Meridional ray in a uniform cylindrical fiber.

estimated by first determining the critical angle θ_C for total internal reflection in the fiber at the fiber core-sample interface. This angle measured with respect to a normal to the fiber core-cladding interface is determined from Snell's law and the indices of refraction of the fiber core n_{CO} and protective cladding n_{CL}. From Snell's law, the critical angle θ_C is given from $n_{CO} \bullet \mathrm{Sin}\theta = n_{Cl} \bullet \mathrm{Sin}\theta_2$ when θ_2 is equal to 90°:

$$\theta_C = \mathrm{Sin}^{-1} (n_{Cl}/n_{CO}) . \tag{6}$$

Measured with respect to the optical axis, the critical angle is $(90°-\theta_C)$. This angle is the acceptance cone half angle Θ_{AC} within the fiber core:

$$\Theta_{AC} = 90 - \mathrm{Sin}^{-1} (n_{Cl}/n_{CO}) . \tag{7}$$

Only radiation having a wave vector k making an angle Θ (with respect to the fiber optical axis) smaller than Θ_{AC} will propagate.

At the end of the fiber, where radiation is launched into the fiber, at the fiber core-air interface, the acceptance cone half angle θ_{AC} in air is determined from Snell's law as:

$$n_0 \bullet \mathrm{Sin}\,\theta_{AC} = n_{CO} \bullet \mathrm{Sin}\,\Theta_{AC} = n_{CO} \bullet \mathrm{Sin}\,(90 - \theta_C) \tag{8}$$

where n_0 is the refractive index of air, which is approximately one, $n_0 \approx 1$. By employing trigonometric identities to rewrite $n_{CO} \bullet \mathrm{Sin}\,(90 - \theta_C) = n_{CO} \bullet (1 - \mathrm{Sin}^2\theta_C)^{1/2}$, and the condition for the critical angle, $\mathrm{Sin}\,\theta_C = (n_{Cl}/n_{CO})$, this expression of Snell's law may be rewritten:

$$n_0 \bullet \mathrm{Sin}\,\theta_{AC} = n_{CO} \bullet [1 - n^2_{Cl}/n^2_{CO}]^{1/2} = (n^2_{CO} - n^2_{Cl})^{1/2} . \tag{9}$$

This gives the acceptance cone half angle, in air, at the fiber end, into which radiation may be launched and propagate along the fiber. The quantity, $(n^2_{CO} - n^2_{Cl})^{1/2}$, is often referred to as numerical aperture of the fiber.

4.2 OPTICAL FIBER RADIATION THROUGHPUT

The amount of radiation energy entering the fiber is determined by the radiance of the source $I_\nu(r,\omega)$ and the radius of the optical fiber core (ρ). The amount of radiation entering the fiber is also determined by the acceptance cone half angle θ_{AC} of the fiber core, which determines the solid angle into which radiation must enter in order to propagate through the fiber.

The radiance of a source is usually given as a specific intensity $I_\nu(r,\omega)$ with units of [energy per unit (time, area, solid angle)] at a given frequency ν. The product of area and solid angle $A \bullet \Omega$ is referred to as throughput. Throughput is a geometrical factor, and in a properly designed optical system the optical throughput is a conserved quantity.

For an optical fiber of cross sectional area $A = (\pi\rho^2)$ and solid angle $\Omega = 2\pi\ (1 - \text{Cos}\ \theta_{AC})$, the amount of specific radiant energy $I^0_\nu(r,\omega)$ entering the fiber core per unit of time is given by:

$$I^0_\nu(r,\omega) = I_\nu(r,\omega) \bullet (A \bullet \Omega) = I_\nu(r,\Omega) \bullet (\pi\rho^2) \bullet 2\pi\ (1 - \text{Cos}\ \theta_{AC})\ . \qquad (10)$$

If absorption by the fiber core and coating is ignored, and the fiber is considered as a perfectly transmitting optical element, then the expression for $I^0_\nu(r,\omega)$ gives the amount of radiant energy propagating through the optical fiber. This expression assumes that radiation uniformly fills the acceptance cone of the fiber core.

4.3 FRESNEL REFLECTION COEFFICIENTS

Assume that the wavelength of the radiation propagating along the optical fiber is small compared to the radius of the fiber core. Then the theoretical results for the Fresnel reflection coefficients which are applicable to the interface of a planar wave guide should be applicable to a curved fiber core sample interface. That assumption will be made here.

At the fiber-sample interface, which is now assumed to be planar, the magnitude of the incident (E_i), reflected (E_r), and transmitted (E_t) waves is given from the general expression:

$$E = E_0 \exp [\, i\,(\omega t - k \bullet r)] \,. \tag{11}$$

The magnitude of the wave vector k is $2\pi n/\lambda$, where n is the magnitude of the (complex) refractive index $n^c = n(1+i\kappa)$.

From the Figure 6 showing the propagation vectors,

$$E_i = E_0 \exp [\, i\,(\omega t - k_1 \bullet (X \operatorname{Sin}\theta + Z \operatorname{Cos}\theta)] \,, \tag{12}$$

$$E_r = |E_r| \exp [\, i\,(\omega t - k_1 \bullet (X \operatorname{Sin}\theta - Z \operatorname{Cos}\theta)] \,, \tag{13}$$

$$E_t = |E_t| \exp [\, i\,(\omega t - k_2 \bullet (X \operatorname{Sin}\theta_2 + Z \operatorname{Cos}\theta_2)] \,. \tag{14}$$

In this Figure, the index of refraction of fiber core is n_1 and the index of refraction of a sample is n_2, which is aluminum hydroxide or natural corrosion in this experiment.

In the spectral range in which aluminum hydroxide and natural aluminum corrosion absorb radiation, the refractive index n_2^c of the sample is complex, $n_2^c = n_2(1+i\kappa_2)$, with absorption index κ_2. In this same spectral region the refractive index for the cladding n_{Cl}^c, and fiber core n_{CO}^c ($\Rightarrow n_1^c$) are approximately real, with very small absorption indices κ_{Cl} and κ_{CO} ($\Rightarrow \kappa_1$), so that $n_{Cl}^c \approx n_{Cl}$ and $n_{CO}^c \approx n_{CO}$ ($\Rightarrow n_1$).

The Fresnel equations for the reflection and transmission coefficients at the interface between the fiber and sample, are derived from the continuity of the normal component of the electric field vector E and the tangential component of the magnetic field vector H which in magnitude is proportional to E. Referring to the Figure 7, and following after the

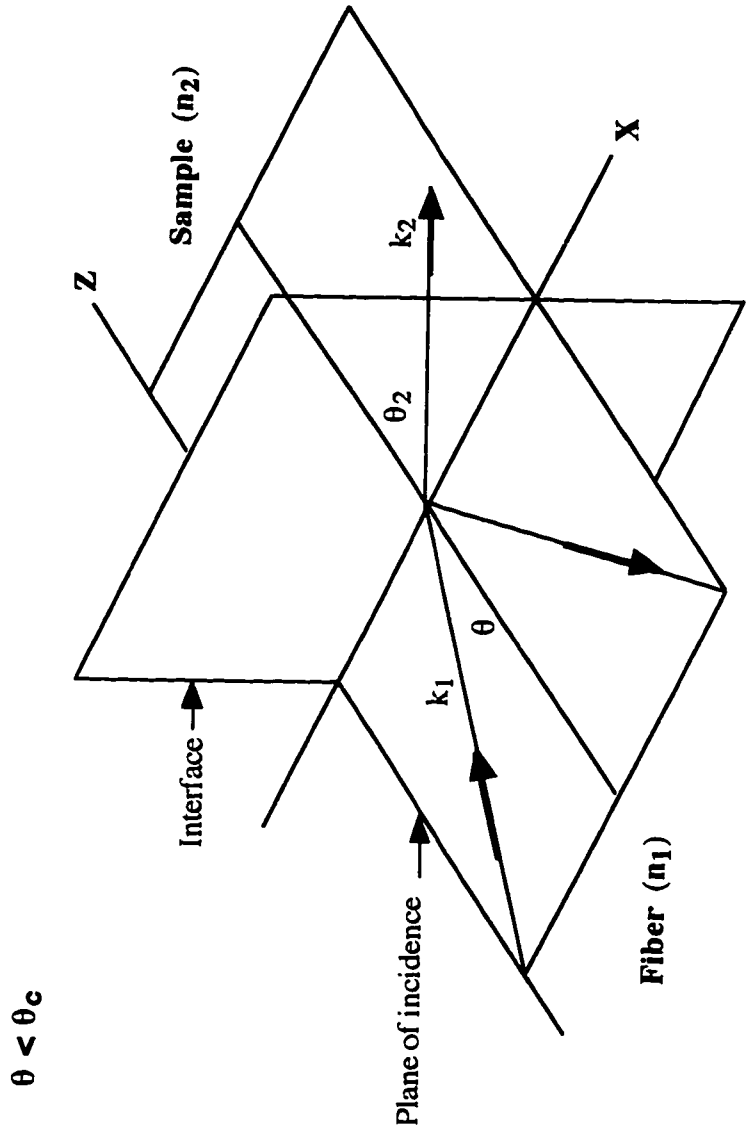

Figure 6. Wave vectors of the incident reflected and transmitted waves.

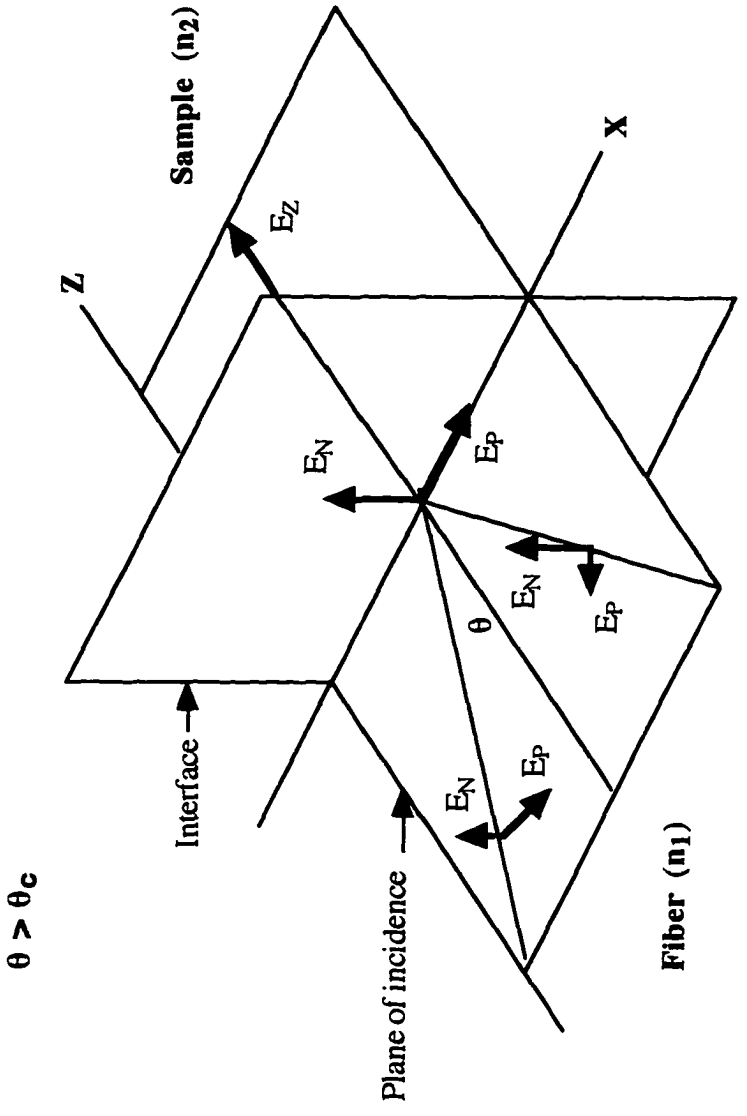

Figure 7. The incident, reflected, and transmitted waves for perpendicular and parallel polarization.

standard derivation given by Lorrain and Corson,[31] the expressions for the Fresnel reflection (r_N, r_P) and transmission (t_N,t_P) coefficients for polarizations perpendicular (N) and parallel (P) to the plane of incidence are the following:

$$r_N \equiv (E_r/E_0)_N = \frac{[\,(n_1/n_2{}^c)\,\mathrm{Cos}\,\theta - \mathrm{Cos}\,\theta_2)\,]}{[\,(n_1/n_2{}^c)\,\mathrm{Cos}\,\theta + \mathrm{Cos}\,\theta_2)\,]}\,, \tag{15}$$

$$t_N \equiv (E_t/E_0)_N = \frac{[\,2\,(n_1/n_2{}^c)\,\mathrm{Cos}\,\theta\,]}{[\,(n_1/n_2{}^c)\,\mathrm{Cos}\,\theta + \mathrm{Cos}\,\theta_2)\,]}\,, \tag{16}$$

and

$$r_P \equiv (E_r/E_0)_P = \frac{[\,-\mathrm{Cos}\,\theta + (n_1/n_2{}^c)\,\mathrm{Cos}\,\theta_2)\,]}{[\,\mathrm{Cos}\,\theta + (n_1/n_2{}^c)\,\mathrm{Cos}\,\theta_2)\,]}\,, \tag{17}$$

$$t_P \equiv (E_t/E_0)_P = \frac{[\,2\,(n_1/n_2{}^c)\,\mathrm{Cos}\,\theta\,]}{[\,(n_1/n_2{}^c)\,\mathrm{Cos}\,\theta + \mathrm{Cos}\,\theta_2)\,]}\,. \tag{18}$$

These expressions give the amplitudes of the reflected and transmitted fields for the two polarizations, at the interface between the fiber and the sample.

4.4 EVANESCENT FIELD IN THE SAMPLE; PENETRATION DEPTH

The amplitude of the evanescent field in the sample is found as follows. Using Snell's law $n_1\mathrm{Sin}\theta = n_2{}^c\,\mathrm{Sin}\theta_2$, the trigonometric identity $\mathrm{Cos}\theta_2 = (\pm)\,\sqrt{(1-\mathrm{Sin}^2\theta_2)}$ may be rewritten as $\mathrm{Cos}\theta_2 = (\pm)\,\sqrt{[\,1-(n_1/n_2{}^c)^2\,\mathrm{Sin}^2\theta\,]}$. The argument under the square root

sign is negative, with $(n_1/n_2^c)^2 \, Sin^2\theta > 1$, for incident angles greater than the critical angle, $\theta > \theta_c$. However, $Cos\theta_2$ may be rewritten in the following form:

$$Cos\ \theta_2 = (\pm)\ i\ (n_1/n_2^c)\ [Sin^2\ \theta - (n_2^c/n_1)^2\ ]^{1/2}\ . \qquad (19)$$

Following Lorain and Corson the negative sign is chosen. With this expression for $Cos\theta_2$ the equation for the transmitted amplitude E_t becomes the following:

$$E_t(\lambda, X, Z) = |E_t|\ exp(i\omega t) \bullet E(\lambda, X) \bullet E(\lambda, Z) \qquad (20)$$

where, E_t is given from the Fresnel transmission coefficients (t_N, t_P). Also the amplitude factors $E(\lambda, X)$ and $E(\lambda, Z)$ are given by:

$$E(\lambda, X) = exp\ [-i\ (2\pi n_1/\lambda_0)\ Sin\theta\ X]\ , \qquad (21)$$

$$E(\lambda, Z) = exp\{-(2\pi n_1/\lambda_0)\ [Sin^2\ \theta - (n_2^c/n_1)^2\ ]^{1/2}\ Z\}\ . \qquad (22)$$

The amplitude factors $E(\lambda, X)$ and $E(\lambda, Z)$ are independent of polarization and apply to both parallel and perpendicular polarizations. The factor $E(\lambda, X)$ is a surface wave propagating along the interface between the fiber and the sample. This surface wave propagates in the same direction as the radiation within the fiber, parallel to the fiber optical axis, along the x direction in Figure 6. The factor $E(\lambda, Z)$ is the evanescent field which penetrates, but does not propagate, into the sample perpendicular to the fiber-sample interface.

In the general case, for an absorbing sample with non-zero κ_2, the field amplitude $E(\lambda, Z)$ takes the following form:

$$E(\lambda, Z) = exp\ (i\ Z/\Lambda_P) \bullet exp\ (-Z/D_P)\ . \qquad (23)$$

Here Λ_P and D_P are given by the following expressions:

$$\Lambda_P = \sqrt{2}\,(\lambda_0/2\pi n_1)\;\left[\left[\nu^2 + \mu^2\right]^{1/2} - \nu\right]^{-1/2}\,, \tag{24}$$

$$D_P = \sqrt{2}\,(\lambda_0/2\pi n_1)\;\left[\left[\nu^2 + \mu^2\right]^{1/2} + \nu\right]^{-1/2}\,, \tag{25}$$

and the quantities ν, and μ are given by:

$$\nu \equiv \mathrm{Sin}^2\,\theta - (n_2/n_1)^2\,(1 - \kappa^2)\,, \tag{26}$$

$$\mu \equiv 2\,(n_2/n_1)^2\,\kappa\,. \tag{27}$$

The quantity D_P is the penetration depth of the evanescent field into the material surrounding the fiber core. the dependence of D_P as a function of the incident angle θ, and for several values of the sample absorption index κ, is shown on the Figure 8. The curves in Figure 8 were calculated for this research, using the refractive index of fiber core $n_1 = 2.8$ and the refractive index of corrosion sample $n_2 = 1.6$. The evaluation of the complex square root in the expression for $E(\lambda, Z)$, for the general case of an absorbing sample, is recorded in Appendix I, since the result differs slightly from that which is found in the literature.

If the absorption index of the sample goes to zero, $\kappa_2 \rightarrow 0$, so that $\mu \rightarrow 0$, then the length $\Lambda_P \rightarrow \infty$ and $(Z/\Lambda_P) \rightarrow 0$ for all practical values of Z. The field amplitude may then be written as follows:

$$E(\lambda, Z) = \exp\,(-Z/D_P) \qquad ;\kappa \Rightarrow 0 \tag{28}$$

where the penetration depth D_P goes to the expression which is most frequently found in the literature:

$$D_P = (\lambda_0/2\pi n_1)\;\left[\mathrm{Sin}^2\,\theta - (n_2/n_1)^2\right]^{-1/2} \quad ;\kappa \Rightarrow 0\,. \tag{29}$$

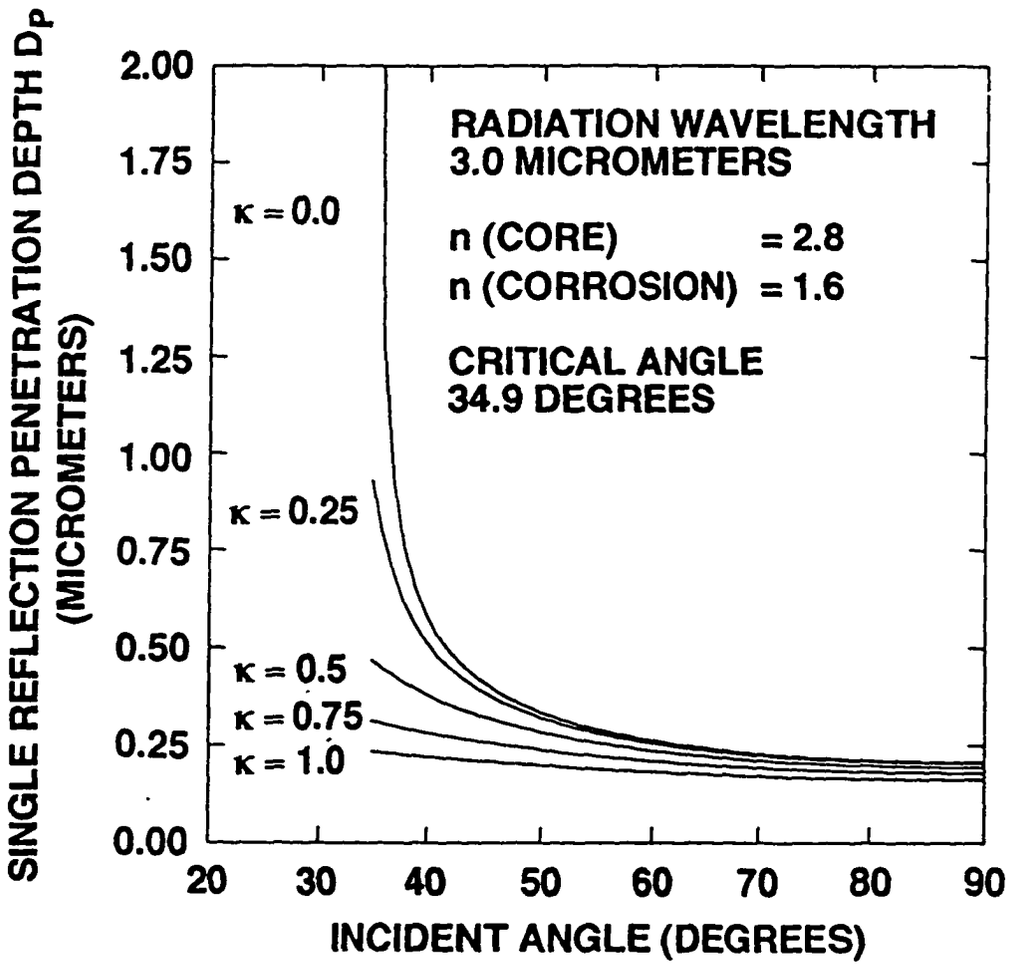

Figure 8. Single reflection penetration depth as a function of incident angle θ for various values of absorption index κ.

4.5 REFLECTIVITY

Using the complex equation for $\mathrm{Cos}\theta_2$ given above, and the result for the evaluation of the square root given in Appendix I, the expressions for r_N, and r_P are evaluated as follows. For the perpendicular polarization the reflection coefficient r_N for single reflection is given by:

$$r_N = \frac{(n_1/n_2^c)\,\mathrm{Cos}\,\theta - (n_1/n_2^c)\,[\,-i\,(\mathrm{Re} + i\,\mathrm{Im})\,]}{(n_1/n_2^c)\,\mathrm{Cos}\,\theta + (n_1/n_2^c)\,[\,-i\,(\mathrm{Re} + i\,\mathrm{Im})\,]}, \tag{30}$$

or

$$r_N = \frac{[\,(\mathrm{Cos}\,\theta - \mathrm{Im}) + i\,\mathrm{Re}\,]}{[\,(\mathrm{Cos}\,\theta + \mathrm{Im}) + i\,\mathrm{Re}\,]}\,. \tag{31}$$

From this expression the reflectivity for single reflection $R_N = r_N^* \bullet r_N$ is found, after some simple algebra, to be the following:

$$R_N = \frac{(\xi - \eta)}{(\xi + \eta)} \tag{32}$$

where $$\xi = \mathrm{Cos}^2\theta + [\,\nu^2 + \mu^2\,]^{1/2}\,, \tag{33}$$

$$\eta = \sqrt{2}\,\mathrm{Cos}\,\theta\,[\,[\,\nu^2 + \mu^2\,]^{1/2} - \nu\,]^{1/2}\,. \tag{34}$$

This expression has the same form as given in the literature by Muller et al.[32] However μ is equal to $2(n_2/n_1)^2\,\kappa$ here. If $\kappa \rightarrow 0$, so that $\mu \rightarrow 0$, then $R_N \rightarrow 1$. This means that if no energy is absorbed from the evanescent field by the sample, then all of the radiant energy is reflected. No radiant energy propagates into the sample.

For the parallel polarization, again using the complex expression for $Cos\theta_2$ and the results of Appendix I, the expression for r_P becomes:

$$r_P = \frac{-\ Cos\,\theta - (n_1/n_2{}^c)^2 \bullet [\,(-i)\,(\,Re + i\,Im\,)\,]}{Cos\,\theta + (n_1/n_2{}^c)^2 \bullet [\,(-i)\,(\,Re + i\,Im\,)\,]}. \qquad (35)$$

Employing the complex expression for $n_2{}^c$, this equation becomes:

$$r_P = \frac{-(n_2/n_1)^2 \bullet (1+ i\,\kappa)^2\ Cos\,\theta + [\,(-i)\,(\,Re + i\,Im\,)\,]}{(n_2/n_1)^2 \bullet (1+ i\,\kappa)^2\ Cos\,\theta + [\,(-i)\,(\,Re + i\,Im\,)\,]}. \qquad (36)$$

The single reflection reflectivity for this polarization $R_P = r_P{}^* \bullet r_P$ yields:

$$R_P = \frac{[\,-(n_2/n_1)^2\ (1-\kappa^2)\ Cos\,\theta + i\,Im\,]^2 + [\,(n_2/n_1)^2\ 2\kappa\ Cos\,\theta - Re\,]^2}{[\,(n_2/n_1)^2\ (1-\kappa^2)\ Cos\,\theta + i\,Im\,]^2 + [\,(n_2/n_1)^2\ 2\kappa\ Cos\,\theta - Re\,]^2}. \qquad (37)$$

This leads to an equation of the form:

$$R_P = \frac{(\,u-v\,)}{(u+v)} \qquad (38)$$

in which (u) and (v) are given by the following equations:

$$u = Cos^2\theta\,[\,(Sin^2\,\theta - v)^2 + \mu^2\,] + [\,v^2 + \mu^2\,]^{1/2} \qquad (39)$$

and

$$v = \sqrt{2}\ Cos\theta\,\{\,(Sin^2\,\theta - v)\,[\,[\,v^2 + \mu^2\,]^{1/2} - v\,]^{1/2} + \mu\,[\,[\,v^2 + \mu^2\,]^{1/2} + v\,]^{1/2}\}. \qquad (40)$$

This expression for R_P has a similar but not identical form as the expression given by Muller et al.[32] The two exceptions are $(Sin^2\,\theta - v)^2$ here, instead of $(Sin^2\,\theta - v^2)^2$ given by

Muller, and again μ is equal to $2\,(n_2/n_1)^2\,\kappa$ here. If $\kappa \rightarrow 0$, so that $\mu \rightarrow 0$, then $v \rightarrow 0$, and $R_P \rightarrow 1$. Again, if no energy from the evanescent field is absorbed by the sample, then all of the radiant energy is reflected. No radiant energy propagates into the sample.

4.6 APPROXIMATION FOR SMALL κ AND LARGE θ

Since the detection technique must be concerned with the situation in which only a small amount or concentration of the sample is present, or the sample is weakly absorbing, the case of small absorption index κ is particularly of interest.

4.6.1 APPROXIMATION FOR SMALL κ

Expressions for single reflection reflectivity R, or the single reflection Fresnel loss (= 1-R), in the approximation of small absorption index κ, are derived in Appendix II.

Consider first the polarization perpendicular to the plane of incidence. From the expression for R_N given above, the single reflection Fresnel loss ($1-R_N$) is:

$$1-R_N = \frac{\sqrt{2}\,\mathrm{Cos}\theta\,[\,[\,v^2+\mu^2\,]^{1/2}-v]^{1/2}}{\mathrm{Cos}^2\theta+[\,v^2+\mu^2\,]^{1/2}+\sqrt{2}\,\mathrm{Cos}\theta\,[\,[\,v^2+\mu^2\,]^{1/2}-v]^{1/2}}\,. \qquad (41)$$

The approximation for this expression in the case of small κ, from Appendix II, is the following:

$$(1-R_N) = \frac{4\,n_{21}^2\,\mathrm{Cos}\,\theta\,\kappa}{(1-n_{21}^2)\,(\mathrm{Sin}^2\,\theta-n_{21}^2)^{1/2}}\,. \qquad (42)$$

A very similar but slightly different expression , derived within the same approximation, has been reported by Katz et al.[33]

For the polarization parallel to the plane of incidence, the single reflection Fresnel loss (1-R_P), from the expression for R_P given above is:

$$(1\text{-}R_P) = 1 - \frac{(u\text{-}v)}{(u+v)} = \frac{2v}{(u+v)} \qquad (43)$$

where (u,v) are given above, or in Appendix II. Approximations for (u,v) in the case of small κ, are also given in Appendix II. The result is the following approximation for (1-R_P):

$$(1\text{-}R_P) \approx \frac{[(4\, n_{21}^2 \cos\theta\, \kappa) \bullet (\sin^2\theta - n_{21}^2)^{1/2}]}{[(n_{21}^2 \cos^2\theta) + (\sin^2\theta - n_{21}^2)]} \bullet \left[2 + \frac{n_{21}^2}{(\sin^2\theta - n_{21}^2)} \right] . \qquad (44)$$

If the approximation may be made that ($4\, n_{21}^4 \bullet \cos^2\theta$) is much smaller than $(\sin^2\theta - n_{21}^2)^{1/2}$, then this expression becomes:

$$(1\text{-}R_P) \approx \frac{4\, n_{21}^2 \cos\theta\, \kappa}{(\sin^2\theta - n_{21}^2)^{1/2}} \bullet \left[2 + \frac{n_{21}^2}{(\sin^2\theta - n_{21}^2)} \right] . \qquad (45)$$

This is similar to the expression, derived within the same approximations, which has been reported by Katz et al.[33] This expression may also be rewritten as :

$$(1\text{-}R_P) = \frac{4\, n_{21}^2 \cos\theta\, \kappa}{(\sin^2\theta - n_{21}^2)^{3/2}} \bullet [\, 2\sin^2\theta - n_{21}^2 \,] . \qquad (46)$$

4.6.2 APPROXIMATION FOR LARGE INCIDENT ANGLE θ

In practice it is often possible to make the additional assumption that the angle of incidence is large, so that $\sin\theta \approx 1$. In this study this approximation is applicable because

the spectrometer optics used to focus the beam radiation on to the fiber is an f/1 zinc selenide lens. Lens which are faster (have small f /numbers) are very thick in the center and introduce frequency dependent aberrations onto the radiation beam. This causes a frequency dependent loss of focus, as an example.

With this additional assumption, that the angle of incidence θ is large, so that $\mathrm{Sin}^2 \theta \approx 1$, the expression for $(1\text{-}R_N)$ becomes:

$$(1\text{-}R_N) = \frac{4\, n_{21}^2 \,\mathrm{Cos}\,\theta\, \kappa}{(1\text{-}n_{21}^2)^{3/2}} . \tag{47}$$

This can be written as:

$$(1\text{-}R_N) = M_N \,\mathrm{Cos}\,\theta\, \kappa \tag{48}$$

which defines a refractive index-matching factor M_N:

$$M_N \equiv \frac{4\, n_{21}^2}{(1\text{-}n_{21}^2)^{3/2}} . \tag{49}$$

In the additional approximation that the angle of incidence is large, the approximation for $(1\text{-}R_P)$ becomes:

$$(1\text{-}R_P) \approx \frac{4\, n_{21}^2 \,\mathrm{Cos}\,\theta\, \kappa}{(1 - n_{21}^2)^{3/2}} \bullet (2 - n_{21}^2) . \tag{50}$$

This expression may be put into this form:

$$(1\text{-}R_P) = M_P \,\mathrm{Cos}\,\theta\, \kappa \tag{51}$$

with

$$M_P \equiv \frac{4\, n_{21}^2}{(1 - n_{21}^2)^{3/2}} \bullet (2 - n_{21}^2) . \tag{52}$$

It may be noted that, within the current approximations of small absorption index κ and large incident angles θ, the Fresnel losses of the perpendicular and parallel polarizations are related as:

$$(1-R_P) = (2 - n_{21}^2) \cdot (1-R_N) . \tag{53}$$

For propagation of unpolarized radiation through an optical fiber, an average Fresnel loss may be given, as the average of the contributions from the parallel and perpendicular polarizations. This will be represented as (1-R) and is equal to (1/2)[(1-R_N)+(1- R_P)], or:

$$(1-R) = M \cos\theta \, \kappa \tag{54}$$

which defines an average index-matching factor M. As a result of the relationship between the Fresnel losses for the perpendicular and parallel polarizations, the refractive index-matching factors are related in the same way; $M_P = (2 - n_{21}^2) \cdot M_N$. This leads to the following expression for M:

$$M = (M_N/2) \cdot (3 - n_{21}^2) = \frac{n_{21}^2 \, (3 - n_{21}^2)}{(1 - n_{21}^2)^{3/2}} . \tag{55}$$

4.7 EFFECTIVE THICKNESS

The interaction of the evanescent wave with the absorbing sample and absorption of energy in the evanescent wave by the sample is given exactly as the single reflection Fresnel loss (1-R), when the reflectivity R is given in terms of the Fresnel single reflection coefficients (r_N,r_P). The Fresnel loss for single reflection is given by (1-R) = (1- $r^* \cdot r$), where r is either of (r_N,r_P) for the perpendicular and parallel polarizations respectively. The Fresnel reflection loss described by the expressions for R given above clearly do not have a

simple form and are described only by computer calculations. As an alternative, several researchers (Herrick, Hansen, Muller) have suggested an approximation applicable for small absorption, in terms of an effective thickness d_{eff}.

In conventional transmission spectroscopy, radiation propagates through a sample of concentration (c), thickness (d) and having an absorption coefficient (α). The transmittance is given by an exponential law, called the Beer-Lambert law:

$$T \equiv (I/I_0) = e^{-\alpha c d} \approx (1 - \alpha c d) \ . \qquad (56)$$

I_0 is the intensity entering the sample and I is the intensity at a distance d inside the sample. The approximation of exponential is applicable for small values of the quantity (αcd). The quantity (αcd) is called the optical depth and has no units. Since d has units of length and c has units of [molecules/volume] the absorption coefficient α has units of [area/molecule] which are the units of a cross section. The absorption coefficient α and the absorption index κ are related in the following way:

$$c\alpha = (4\pi/\lambda)\, n\kappa \ . \qquad (57)$$

Radiation absorptance (A_p) is defined as one minus the transmittance, which in the approximation of small optical depth is equal to the optical depth:

$$A_p \equiv (1-T) \approx \alpha c d \ . \qquad (58)$$

A related quantity which is often used in applications and in the presentation of results is radiation Absorbance (A) which is defined as:

$$A \equiv -\mathrm{Log}_{10}(I/I_0) = (\alpha^{o}\, cd) \ . \qquad (59)$$

This expression defines an absorption coefficient α^o which is related to the absorption coefficient α in the Beer-Lambert law as:

$$\alpha^o = \alpha /(\mathrm{Log_e}10) = 0.434\,\alpha \ . \tag{60}$$

By analogy with the above description, for internal reflection spectroscopy, an effective thickness (d_{eff}) is defined such that the Fresnel single reflection loss can be described by:

$$(1\text{-}R) \equiv \alpha c d_{eff} \ . \tag{61}$$

This expression defines the effective thickness. In the approximation of small absorption ($\alpha c d_{eff} << 1$) the effective thickness represents the film thickness required to give the same absorption as that obtained in a transmission measurement. From this definition for the single reflection loss, the single reflection power will be:

$$R \equiv (1 - \alpha c d_{eff}) \ . \tag{62}$$

For multiple reflections with number of bounces b, the total reflected power, the transmittance T, will given by:

$$T = R^b = (1\text{-}\alpha c d_{eff})^b \tag{63}$$

while the total loss, the absorptance A_p will be:

$$A_p = (1\text{-}R^b) = [\ 1\text{-}\ (1\text{-}\ \alpha c d_{eff})^b\ ] \ . \tag{64}$$

In the approximation of small absorption R^b and $(1\text{-}R^b)$ become:

$$R^b \approx (1\text{-}b\alpha c d_{eff}) \approx e^{-b\alpha c d_{eff}} \tag{65}$$

and

$$(1\text{-}R^b) \approx b\alpha c d_{eff} \ . \tag{66}$$

This establishes the analogy with conventional transmission experiments, which is applicable only in the case of small ($\alpha c d_{eff}$): R^b is analogous to the transmittance T, and $b \bullet d_{eff}$ is analogous to the sample thickness d.

In the approximation of small single reflection Fresnel loss, the expression for R^b may also be written as:

$$R^b \approx [1 - b\,(1-R)] = e^{-b(1-R)} \quad . \tag{67}$$

This gives the reflectivity R^b, which is analogous to transmittance T, in terms of the number of reflections (b) and the single reflection Fresnel loss (1-R). In analogy with conventional transmission spectroscopy, R^b will be referred to as the ray transmittance. The expression may be rearranged as $(1-R^b) \approx b\,(1-R)$ which say that the total Fresnel loss after b reflection is b times the single reflection Fresnel loss. This approximation is applicable only in the case of small absorption, that is small ($\alpha c d_{eff}$).

An expression for the effective thickness may be obtained from the general expressions for the single reflection Fresnel loss (1-R) given above. Consider the perpendicular polarization ($1-R_N$). Follow Appendix II and approximate the square root factor $((\nu^2+\mu^2)^{1/2}-\nu)^{1/2}$ in the numerator as $(\mu/\sqrt{(2\nu)})$. In addition, employ the relation between the absorption coefficient α and the absorption index κ given above, $c\alpha=(4\pi/\lambda)(n\kappa)$, and the relation defining the effective thickness, $(1-R) = \alpha c d_{eff}$. Then from the general expression for $(1-R_N)$ the following expression for the perpendicular component of the single reflection effective thickness $(d_{eff})_N$ is obtained:

$$(d_{eff})_N \approx \frac{\dfrac{\cos\theta\, n_{21}\, \lambda_0}{2\pi n_1} \bullet (\sin^2\theta - n_{21}^2)^{-1/2}}{\cos^2\theta + [\nu^2 + \mu^2]^{1/2} + \sqrt{2}\cos\theta\,[[\nu^2 + \mu^2]^{1/2} - \nu]^{1/2}} \quad . \tag{68}$$

This expression was obtained by writing $(1-R_N)$ so that it is proportional to $c\alpha$ $(=4\pi n\kappa/\lambda)$. The factor which multiplies α is then $(d_{eff})_N$. The presence of terms proportional to μ^2 (proportional to κ^2) is ignored. The effective thickness is a function of the incident angle θ, the sample absorption index κ_2, penetration depth, refractive indices n_1 and n_2 Harrick and Hansen have separately derived expressions for effective thickness under different assumptions. Their results agree with the result given above. This expression for the effective thickness d_{eff} may be rewritten, in the approximation of small absorption index, $(\kappa<<1)$, in terms of the small κ penetration depth D_P $(\kappa<<1)$, and (ξ,η) given above as follows:

$$(d_{eff})_N \approx \frac{\text{Cos}\,\theta\; n_{21} \bullet D_P\,(\kappa<<1)}{(\xi+\eta)} \; . \tag{69}$$

For the parallel polarization $(1-R_P)$ and again following the approximations given in appendix II for the numerator (v), the effective thickness will be:

$$(d_{eff})_P \approx \frac{\dfrac{\text{Cos}\,\theta\; n_{21}\,\lambda_0}{2\pi n_1} \bullet (\,2\,\text{Sin}^2\theta - n_{21}{}^2\,)}{(u+v) \bullet [\,\text{Sin}^2\theta - n_{21}{}^2\,]^{1/2}} \tag{70}$$

or

$$(d_{eff})_P \approx \frac{\text{Cos}\,\theta\; n_{21} \bullet D_P\,(\kappa<<1)}{(u+v)} \bullet [\,2\,\text{Sin}^2\theta - n_{21}{}^2] \; . \tag{71}$$

The effective thickness is shown in the Figure 9 as a function of the incident angle θ, for several values of the sample absorption index κ. The curves in Figure 9 were calculated for this research with the same conditions as the penetration depth shown in Figure 8. Perpendicular and parallel polarizations have different magnitudes. In Figure 9, the average

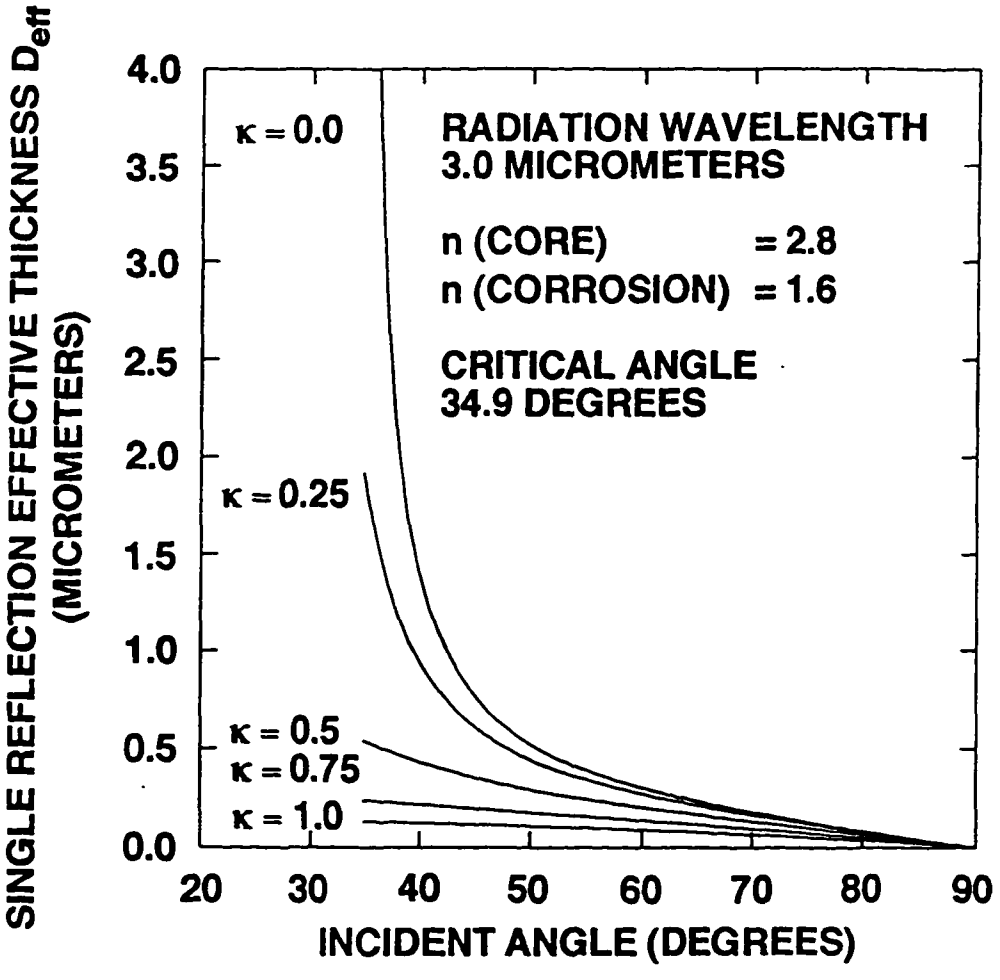

Figure 9. Single reflection effective thickness as a function of incident angle θ for various values of absorption index κ.

of the two polarization is given, which is applicable to the case of unpolarized radiation. Notice that the effective thickness approaches zero as the angle of incidence approaches 90 degrees.

4.8 TOTAL FRESNEL LOSS FOR SMALL κ

The expressions for single reflection Fresnel loss given above vary as a function of the incident angle θ. The total Fresnel loss will depend on the number (b) of bounces of the radiation over a length of fiber (L) which is in contact with the sample, and the solid angle (Ω) of the cone of propagation of the radiation within the fiber. The distance (l) between two reflections, or bounces, of the radiation within a fiber of core diameter (d) for a given incident angle θ is $l = d \bullet \mathrm{Tan}\theta$. Then the total number of bounces over a fiber segment of length (L) will be $b = (L/l) = (L/d) \bullet \mathrm{Cot}\ \theta$. In the approximation of small single reflection loss, the Fresnel loss for radiation incident at an angle θ will be the single reflection Fresnel loss (1-R) times the number of reflections (b).

Assume that the cone through which the radiation is propagating within the fiber is uniformly filled with unpolarized radiation. Then the total Fresnel loss will be the Fresnel loss for a particular incident angle θ integrated over the solid angle of the cone of propagation of the radiation:

$$(1- R^b) = \int_\Omega b (1-R) \, d\Omega \ . \qquad (72)$$

Relative to the optical axis the solid angle increment $d\Omega$ is given by $(\mathrm{Sin}\Theta \, d\Theta \, d\phi)$. Since the angle of incidence θ and the complementary angle Θ are related as $(\Theta+\theta) = 90°$, the solid angle increment with respect to θ will be $(\mathrm{Cos}\theta \, d\theta \, d\phi)$. The limits of integration on θ will be $(90,\theta_0)$. In practice, and in the study reported here, the angle θ_0 will be much larger than the critical angle θ_C.

The general expressions for the single reflection Fresnel loss given above, for the perpendicular and parallel polarizations, are not easily integrated over θ in closed analytical form. Adopting the assumptions of small sample absorption index κ, large incident radiation angle θ, and unpolarized radiation propagating through the fiber, the expression for the total Fresnel loss becomes:

$$(1-R^b) = (L/d)\, M\, \kappa \left\{ (1/2\pi) \int_{\theta=90}^{\theta=\theta_0} \int_{\phi=0}^{2\pi} (\mathrm{Cos}^3\theta/\mathrm{Sin}\theta)\, d\phi\, d\theta \right\} . \qquad (73)$$

Notice that the solid angle average is normalized to 2π for propagation only in the forward direction. This integral is easily performed and the result is the following:

$$(1-R^b) = (L/d)\, M\, \kappa\, [\, (1/2)\, \mathrm{Cos}^2\theta_0 + \log\ \mathrm{Sin}\, \theta_0\,] . \qquad (74)$$

In the approximation of large θ_0, $\mathrm{Sin}\theta_0$ will be approximately one, and $\mathrm{Log}(\mathrm{Sin}\,\theta_0)$ will be approximately zero. Also, the angle θ_0 is measured relative to a normal to the fiber-sample interface. This angle may be replaced with the complementary angle Θ_0 measured relative to the fiber optical axis, through the relations $\theta_0+\Theta_0=90°$, and $\mathrm{Cos}^2\theta_0 = \mathrm{Sin}^2\Theta_0$. With the additional approximation that $\mathrm{Sin}^2\Theta_0 \approx \Theta_0^2$ for small Θ_0 (θ_0 large), the expression for the total Fresnel loss, absorptance A_p, becomes:

$$A_p = (1-R^b) = (1/2)\, (L/d)\, M\, \kappa\, \Theta_0^2 . \qquad (75)$$

It should be emphasized that this is the lowest order approximation to $(1-R^b)$ in the quantities κ and θ, and applies only to the case of unpolarized radiation.

4.9 RETRIEVAL OF ABSORPTION INDEX κ

Absorptance A_P of the propagating radiation is described in general as mentioned above:

$$A_P = (1-R^b) = [\ 1-(1-\alpha c d_{eff})^b] \qquad (64)$$

where R is the Fresnel single reflection reflectivity and b is the number of reflections of the radiation in the fiber at an incident angle θ.

For the approximation of small κ, radiation absorptancs A_p can be expressed as below:

$$A_p = (1-R^b) \approx \alpha \bullet b c d_{eff} = \alpha c D_{eff} \quad . \qquad (76)$$

Total effective thickness D_{eff} is equals to single reflection effective thickness d_{eff}, times the number of bounces (b) of the radiation. The absorption coefficient α and the absorption index κ are related as mentioned before:

$$n\kappa = (\lambda c \alpha / 4\pi) \ . \qquad (77)$$

The general expressions for the reflectivity R and the effective thickness is a complicated functions, as explained in detail at sections 4.5 and 4.7, depending on both instrumental properties and physical properties of the sample. It depends on the indices of refraction (n_{CO}, n) of fiber core and surrounding sample, the incident angle θ, the wavelength of the probing radiation λ, and the absorptive index κ. If all the quantities in the expression for R are known except the absorption index κ, then κ may be inferred by adjusting its value until the calculated absorptance agrees with the experimentally measured absorptance.

As the penetration depth increases, the effective thickness increases and with it the Fresnel reflection loss. This connection has been given in theory (section 4.7) mathematically for the general case of evanescent wave absorption. Those results are general, and are applicable to experiments employing either crystals or optical fibers as ATR elements.

A simple expression for the absorptance as a function of ($n\kappa$) can be obtained from the expression of total Fresnel loss, in the approximation of small absorption κ and large incident angle θ, which is applicable in particular to experiments employing optical fibers. The result can be rewritten from equation (75) as below:

$$A_p = (1-R^b) \approx (1/2)\,(L/d)\,M\,\kappa\,\Theta_0^2 \quad . \tag{78}$$

Since the largest angle $\Theta_0 \Rightarrow \theta_{AC}$, and $M' \Rightarrow M/n$ for convenience of the retrieval of ($n\kappa$)

$$A_p \approx (1/2) \bullet (L/d) \bullet n\kappa \bullet M' \theta_{AC}^2 \quad . \tag{79}$$

Here L is the length of the decoated fiber in contact with the material to be detected, d is the diameter of the fiber core, and θ_{AC} is the half angle of the acceptance cone of the radiation propagating through the fiber. The quantity M' is the index matching factor. It depends on the value of the real parts of the refractive indices of the fiber core n_{CO} and the material surrounding the core n. From equations 76, 77 and 79, we may write for this special case an approximate expression for the effective thickness:

$$D_{eff} \approx (\lambda/8\pi) \bullet (L/d) \bullet M' \theta_{AC}^2 \quad . \tag{80}$$

This approximation of the effective thickness depends only on experimental properties. From Figure 9 it may be seen that for the case of radiation propagation at high angles of incidence, the calculated effective thickness is approximately the same with and without accounting for the absorptive index. For these angles equation (80) should be applicable.

In the approximation of small absorption κ the absorption index may be determined from the approximation for A_P given above:

$$(n\kappa) = \frac{(\lambda/4\pi) \bullet (A_p)_{exp}}{D_{eff}} \tag{81}$$

where $(A_p)_{exp}$ is the experimentally measured absorptance.

CHAPTER 5

EXPERIMENTAL SETUP AND PROCEDURE

The main purpose of the experiment is to integrate optical fibers into an FTIR interferometer spectrometer. The interferometer spectrometer can be located away from the sensing area where the sensing fiber can be embedded. Using a small flexible optical fiber, radiation can reach almost any location and be returned to the detector without any disturbance. Integration of optical fiber into the interferometer spectrometer and possible instrumental setup for the best signal result are the main objective of this experiment.

5.1 MICHELSON INTERFEROMETER

The Michelson interferometer is a device that can divide the amplitude of a beam of radiation into two paths and then recombine the two beams after a path difference has been introduced. A condition is thereby created under which interference between the beams can occur. The intensity variations of the beam emerging from the interferometer can be measured by a detector as a function of path difference which is varied in a controlled way. The simplest form of the Michelson interferometer is shown in Figure 10 referenced from P.R. Griffiths.[34]

The Michelson interferometer consists of two mutually perpendicular plane mirrors, one of which can move along an axis that is perpendicular to its plane. The movable mirror is moved at a constant speed. Between the fixed mirror and the movable mirror is a beam splitter, where a beam radiation from an external source can be partially reflected to the fixed mirror and partially transmitted to the movable mirror. After the two beams return to the beam splitter, they interfere and are again partially reflected and partially transmitted. Because of the effect of interference, the intensity of the beam reaching the detector depends on the difference in path of the beam in the two arms of the interferometer. The

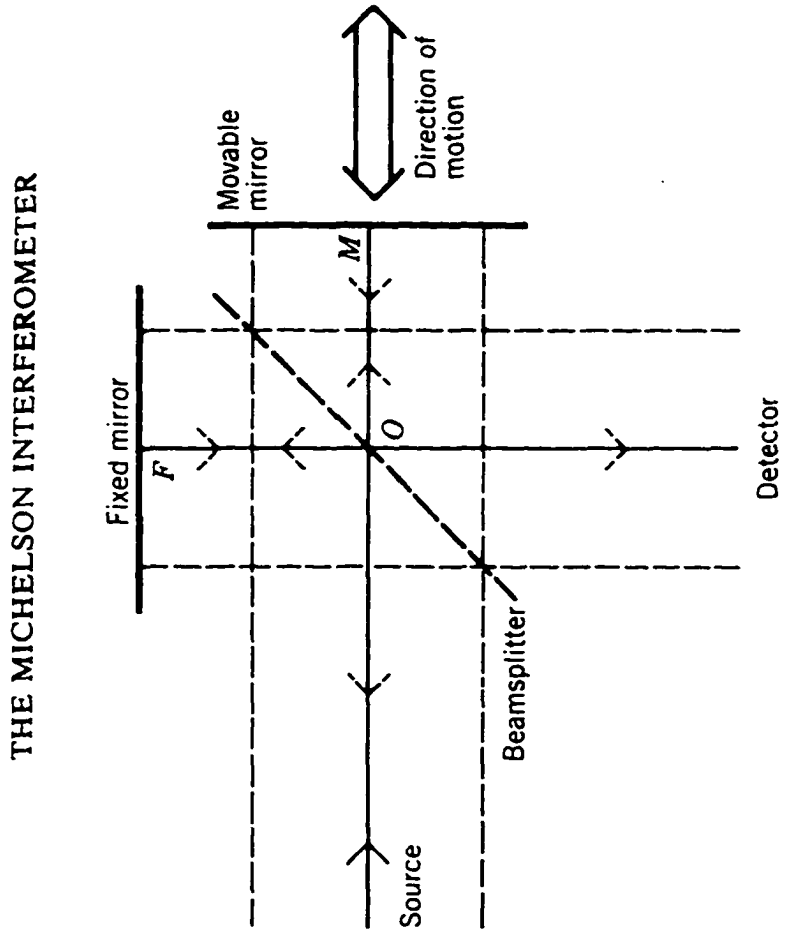

Figure 10. Schematic representaion of a Michelson interferometer

variation in the intensity of the beam reaching the detector as a function of path difference yields the spectral information in a Fourier Transform Spectrometer (FTS).

Assuming that a source of monochromatic radiation produces an infinitely narrow and perfectly collimated beam, the path difference between the beams traveling to the fixed and moving mirror is called the retardation δ. When the fixed and moving mirrors are equidistant from the beam splitter (zero retardation), the two beams are perfectly in phase. At this point, the beams interfere constructively, and the intensity of the beam reaching the detector is the intensity of the combined beams. If the movable mirror is displaced by $(1/4)\lambda$, the retardation is now $(1/2)\lambda$. The pathlengths to and from the fixed and movable mirror are exactly one half wavelength difference. On recombination at the beam splitter, the beams are out of phase and interfere destructively. At this point all the light returns to the source and none passes to the detector.

If the mirror is moved at constant velocity, the signal at the detector can be seen to vary sinusoidally, a maximum being registered each time that the retardation is an integral multiple of λ. The intensity of the beam at the detector measured as a function of retardation is given the symbol $I'(\delta)$. The intensity at any point where $\delta = n\lambda$ (where n is an integer) is equal to source $I(\nu)$. At other values of δ , the intensity of the beam at the detector is given by:[34]

$$I'(\delta) = (1/2)\, I(\nu)\, \{1 + \cos 2\pi\nu\delta\} \qquad (82)$$

assuming that the reflectance and transmittance are both 50 % at the beam splitter. Only the ac component is recorded in spectrometric measurement, and it is this modulated component that is generally referred to as an interferogram. So, the interferogram from a monochromatic source measured with an ideal interferometer is given by the equation:

$$I(\delta) = (1/2)\, I(\nu) \cos 2\pi\nu\delta. \qquad (83)$$

In practice, it is impossible to find a beamsplitter having the ideal characteristics of 50 % reflectance and 50 % transmittance. Also with the wavenumber-dependent beamsplitter efficiency, the equation of interferogram can be modified as below.

$$I(\delta) = B(\nu) \cos 2\pi\nu\delta \,, \tag{84}$$

where $B(\nu)$ gives the intensity of the source at a wavenumber ν as modified by the instrumental characteristics. Mathematically $I(\delta)$ is said to be the cosine Fourier transform of $B(\nu)$. The spectrum is calculated from the interferogram by computing the cosine Fourier transform of $I(\delta)$. This spectrometric technique is called Fourier transform spectrometry.

In most commercially available Michelson interferometers, the movable mirror is scanned at a constant velocity v (cm /sec). For these instruments, the interferogram varies as a function of time, I(t), rather than as a function of retardation , $I(\delta)$. The retardation t seconds after the zero retardation point is given by:

$$\delta = 2vt \ \text{(cm)} \tag{85}$$

and the intensity of interferogram as a function of time I(t) is given by

$$I(t) = B(\nu) \cos 2\pi\nu \bullet 2vt \,, \tag{86}$$

$$= B(\nu) \cos 2\pi f t \,, \tag{87}$$

where v is the velocity of moving mirror and 2vt is the retardation after t seconds. The frequency, $f=2v\nu$ is called the modulation frequency of the interferogram.

When the source is a continuum, the interferogram can be represented by the integral:

$$I(\delta) = \int B(\nu) \cos 2\pi\nu\delta \bullet d\nu \tag{88}$$

and the spectrum can be calculated as below:

$$B(\nu) = \int I(\delta) \cos 2\pi\nu\delta \bullet d\delta \ . \qquad (89)$$

In practice, the signal must be digitized at finite sampling intervals and computing the Fourier transform is done using a Fast Fourier Transform algorithm at the end of data collection.

Sampling the interferogram at equal intervals of retardation is one of the important steps of this interferometer. The Fourier transform spectrometer used in this study involved a reference laser beam for this purpose. When monochromatic light is passed through the same interferometer to a separate detector, a sinusoidal signal is measured. Since each zero crossing of the laser interferogram is found at equal intervals of retardation, they can be used to trigger the Analog to Digital Converter (ADC) sampling of the signal from the main interferometer.

Several studies have demonstrated that FTIR spectrometers have some advantages in comparison with grating spectrometers.[34,35] The maximum allowed optical throughput, which is defined as the product of area of a beam at a focus and its solid angle, of a Fourier spectrometer is far greater than a grating spectrometer. This is called Jacquinot's advantage. The multiplex advantage of Fourier spectrometers can be expressed the following way. The signal to noise ratio (SNR) of spectra measured on a Fourier spectrometer will be greater than SNR of the spectrum measured in the same time and at the same resolution on grating spectrometer with the same source, detector, optical throughput, optical efficiency, and modulation frequency. This is called Fellgett's advantage. One other advantage of interferometer is that stray radiation can be filtered out while second-order radiation is extremely difficult to filter out without severely attenuating first-order radiation in grating spectrometry.

5.2 EXPERIMENTAL SETUP

A Digilab FTS-45 spectrometer was used in this study [36] . The arrangement of components is shown schematically in Figure 11. The interferometer is a 60 degree Michelson interferometer, which means the angle between the beamsplitter and optical axis of the each mirror. The interferometer moving mirror has an air-bearing which uses the same source of dry nitrogen that is used to purge the interferometer chamber and sample compartment. The beam splitter is a potassium bromide substrate with a germanium coating. The source of infrared radiation is a water-cooled ceramic filament heated to approximately 1800 °C. A 632.8 nm Helium-Neon laser was used as a reference laser for sampling at each zero-crossing.

An optical fiber accessory designed and built by Digilab, was used to match the optical sensing fiber and the interferometer; see Figure 11. This accessory, which fits into the spectrometer sample compartment, includes a flat mirror and a pair of rigidly mounted zinc selenide lenses which focus the radiation onto the input end of the fiber and onto the detector. The lenses are f/1, fifteen millimeters in diameter. The two ends of the fiber are mounted, with SMA connectors, to L-brackets which are attached to x,y,z alignment stages. Two detectors were used; either a liquid nitrogen cooled InSb or a liquid nitrogen cooled narrow-band MCT detector. The detector is mounted in the sample compartment but the sample can be situated outside the sample compartment depending on the length of the sensing fiber. The experimental components were chosen to study the 2 to 12 μm wavelength spectral range. Most of the data reported here was collected at the highest resolution available, which was four wavenumber. However, the effect of resolution on the spectral data at lower resolutions was investigated.

A horizontal crystal ATR accessory obtained from Digilab was used to make the reference measurements, in comparison with the spectral data using optical fiber, which are

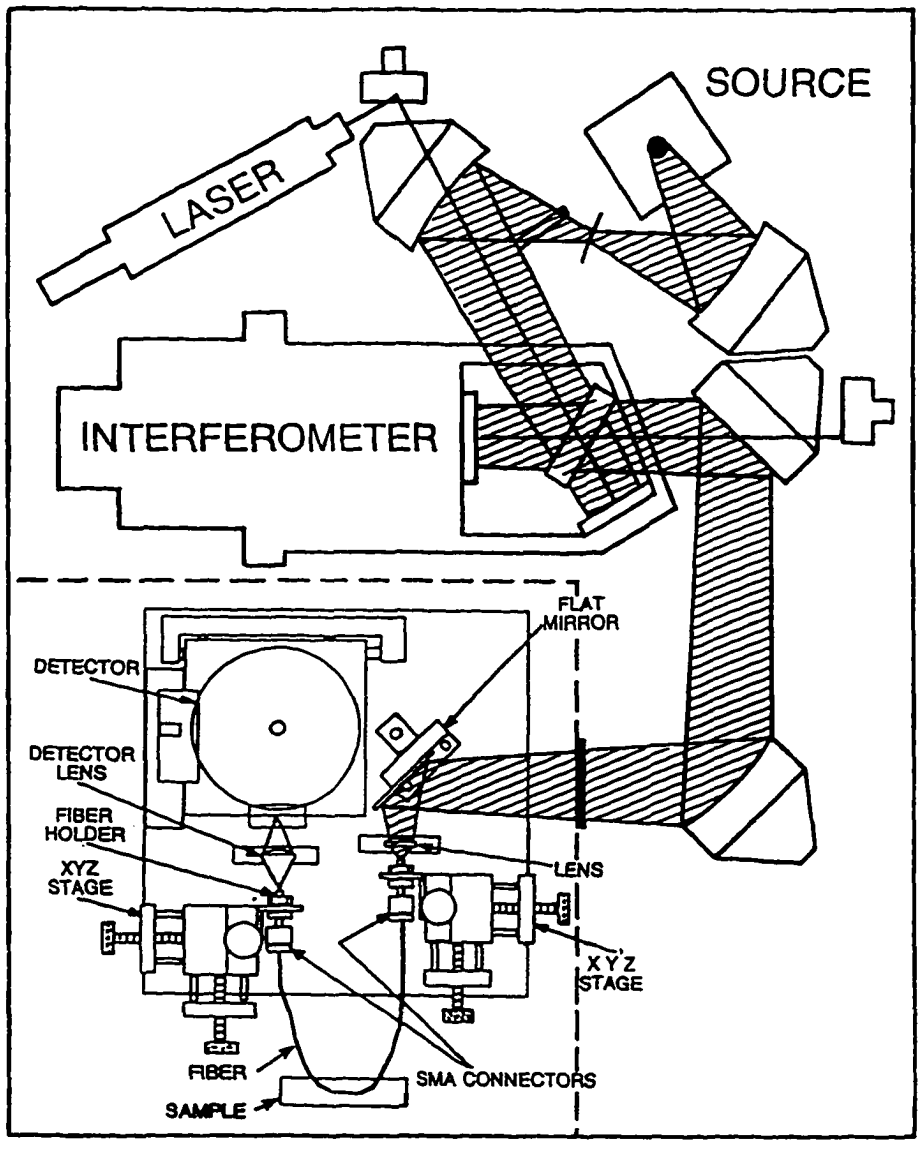

Figure 11. Experimental setup, including interferometer spectrometer and optical fiber accessory.

also reported here. The optics of this accessory were designed to fit within the sample compartment of the interferometer spectrometer, so that the optical path may be purged. The optical path of the radiation through the seven-bounce zinc selenide ATR crystal and optical accessory is indicated in Figure 12. The sample surface area of the ATR crystal was 8 mm x 70 mm or 5.6 cm^2. The liquid nitrogen cooled MCT detector mounted within the spectrometer, outside the sample compartment, was used with the zinc selenide crystal as the ATR element. Also, the sample is situated outside the sample compartment as shown in Figure 12.

When an optical fiber, and associated optical accessory, are part of the optical path of the spectrometer, the throughput is reduced and some radiation is lost. The interferometer throughput without the optical fiber is approximately 0.06 (cm^2•Ster). The transmission characteristics of an optical fiber depends on the fiber material, core diameter, and the composition of coating and cladding. The throughput of an optical fiber may be computed from the core diameter and the fiber numerical aperture.[37] However the zinc selenide lenses of the optical fiber accessory are the limiting elements when this accessory is in the optical path of the interferometer spectrometer. These lenses are f/1 and have a numerical aperture of 0.4 corresponding to an acceptance cone with half angle of approximately 26.5°. This is smaller than the numerical aperture of the chalcogenide fibers, approximately 0.5. Assuming the fibers are perfectly transmitting optical elements, the throughput of the optical fiber and optical accessory may be computed from the cross sectional area of the fiber core, and the numerical aperture of the f/1 zinc selenide focusing lens. For the experiments reported here, the radius of fiber core is approximately 250 micrometers, and the numerical aperture of the zinc selenide focusing lens is approximately 0.4. From the expression given above, the throughput is approximately 0.0013 (cm^2•Ster). This is about 45 times smaller than the spectrometer throughput. The cross

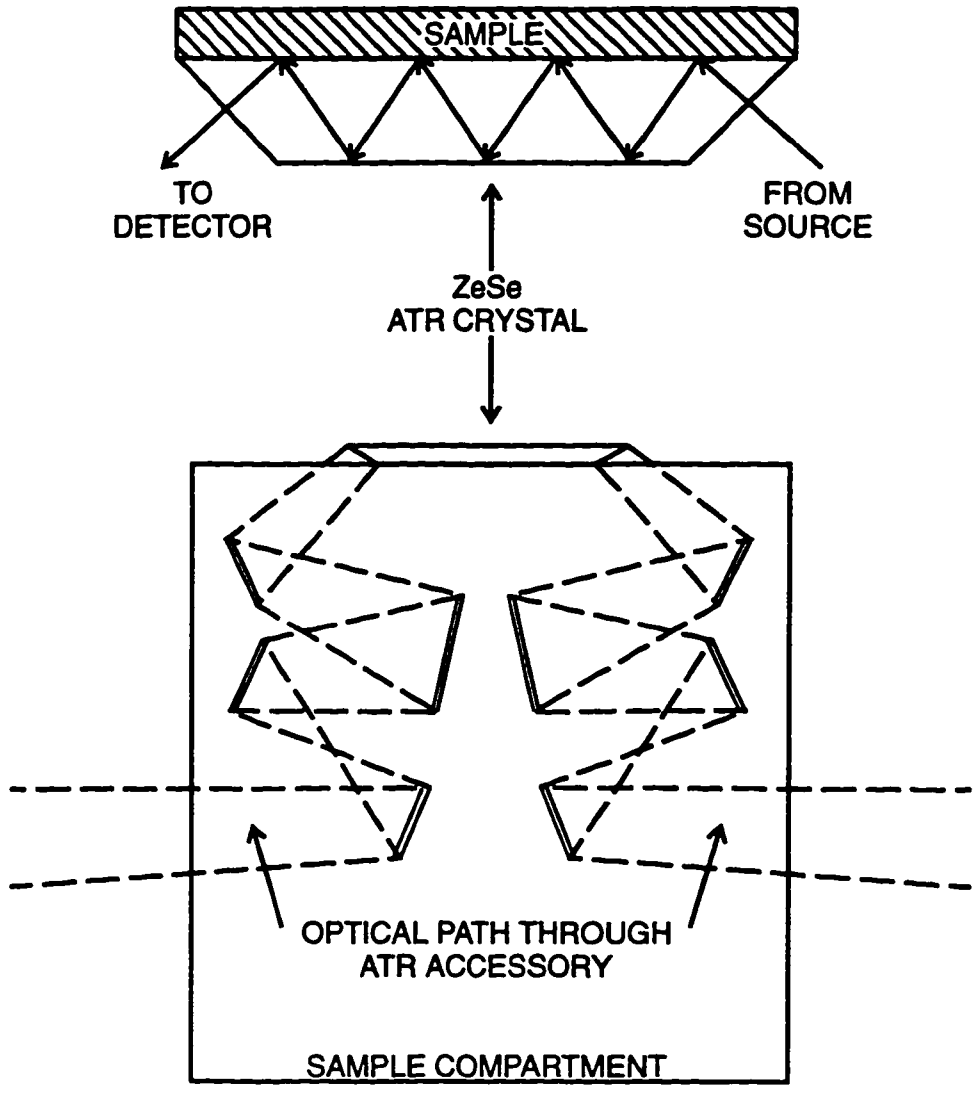

Figure 12. Optical path through the seven-bounce zinc selenide ATR crystal.

section of the ATR zinc selenide crystal is 6 mm by 9mm and does not suffer a loss of throughput.

Loss of throughput reduces the sensitivity of the combined optical fiber interferometer spectrometer. In addition, there are reflection losses at the input and output faces of the polished fiber ends. And finally, the chalcogenide fiber has a characteristic pattern of infrared absorption which depends on the core and coating materials. These losses, due to reflection and absorption, also reduce the sensitivity of the combined optical fiber interferometer spectrometer. Sensitivity may be improved by reducing the resolution and increasing the data collection time. The latter is achieved by increasing the number of scans of the moving mirror and with it the total number of coadded interferograms.[34,35] Typically, to obtain signal to noise ratios of at least 100 to 1, at 4 cm^{-1} resolution, it was necessary to collect and coadd approximately 512 scans in the background and sample spectra.

5.3 CHALCOGENIDE OPTICAL SENSING FIBER

One to four meter lengths of plastic coated 250 and 500 micrometer core diameter chalcogenide optical fibers were used for the experiments discussed here. These fibers were obtained from Amorphous Materials.[10] These fibers have acceptable loss, approximately 1 dB per meter, and transmits in the mid infrared spectral region in which $Al(OH)_3$ absorbs radiation. Also, the fiber is relatively easy to decoat and handle after it has been decoated. The fiber must be decoated because the material to be detected has to be in contact with the fiber core or in very close proximity to the core. This is because the evanescent wave penetrates only a few micrometers beyond the core boundary into the plastic coating. For example, with n_{co} equal to 2.81 for the chalcogenide fiber core and n_{Cl} equal to 2.18 for the plastic coating, the minimum penetration depth for radiation with

wavelength of 3 μm, $D_{p,min}$, is approximately 0.25 μm. The plastic coating, which has a minimum thickness of approximately 40 μm, absorbs the evanescent wave and prevents the evanescent field from reaching the aluminum hydroxide.

Decoating was accomplished by immersing the coated fiber in acetone for fifteen minutes to one hour. This softens the plastic and loosens the coating from the core. The fragments of the coating may then be removed by gently rubbing the coating away from core with a cotton swab. After decoating, careful handling of the fiber is necessary, to avoid breaking the exposed fragile fiber core. Most of the data reported here were obtained using 500 micrometer core diameter chalcogenide fiber, with 10 to 300 centimeters of the fiber decoated. The smaller, 250 micrometer core diameter, fibers produce greater evanescent wave absorption,[38] when compared to the 500 micrometer core diameter fibers. This is because more bounces of the propagating wave occur within a given length of the smaller diameter fiber. But the smaller diameter fibers break easily. Consequently, the largest data set was obtained using the larger, 500 micrometer, diameter fibers.

5.4 SAMPLE MATERIALS

Pure powdered aluminum hydroxide, $Al(OH)_3$ was obtained from the J.T. Baker chemical company.[39] Aluminum hydroxide powder was used in a pure powdered form and also as a paste mixed either with water or acetone. Using a paste allows the powder to be made more compact and as a result brought into closer contact with the fiber core. This increases the uniformity of the coating of the powder on the fiber core and increases the effective thickness of the sample for absorption of the evanescent wave. To collect data a paste of aluminum hydroxide was packed around the decoated fiber core. Then the mixture, either with water or acetone, was allowed to dry before spectral data was collected. The example of the sensing fiber and sample arrangement is shown on Figure 13.

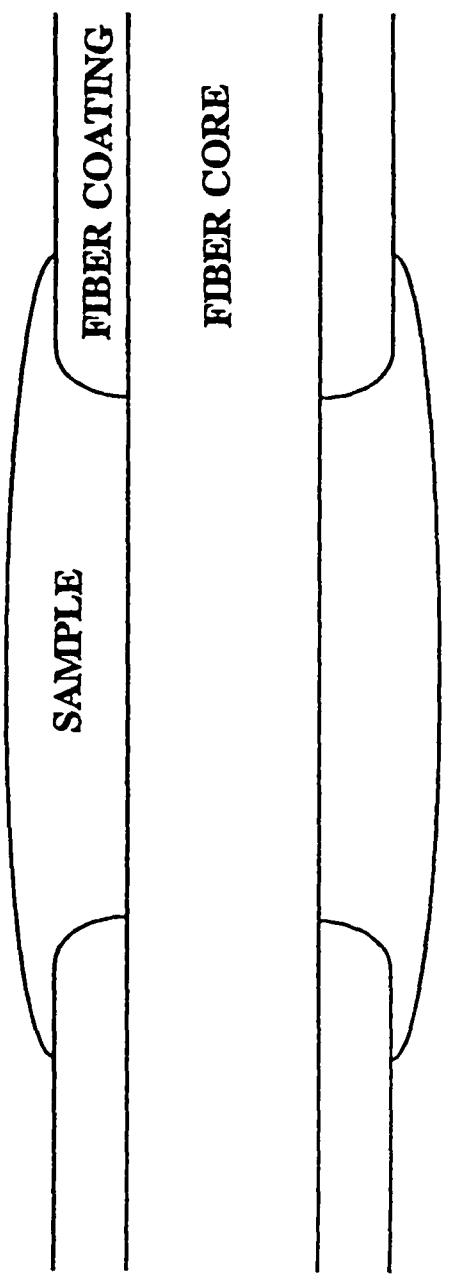

Figure 13. Optical sensing fiber and sample arrangement

Samples of naturally corroded aluminum alloy were obtained through the Naval Air Station at Norfolk Virginia. The corroded samples were from discarded aircraft parts; so the color, texture and composition were different from sample to sample. The samples were collected by scraping the accumulated natural corrosion from a portion of an aluminum alloy aircraft frame component. However, it was not possible to document the exact alloy of the aircraft component. The corrosion samples were prepared by grinding the corrosion sample to form a fine powder. The powder was then mixed with acetone to form a paste. The paste was placed around the fiber core and allowed to dry before the spectral data was collected.

5.5 EXPERIMENTAL PROCEDURE

Background spectra were collected with the decoated fiber as an integral part of the optical path, but without the presence of the sample. Inclusion of the optical fiber in the optical path influences the background in two particular ways. The background spectral response depends on both the extent to which the fiber has been decoated and to a lesser extent the configuration of the fiber, the number of bends and the radii of the bends. The fiber must be decoated before the background spectra are collected, because the plastic coating (or cladding) absorbs some of the evanescent wave.

The effect of decoating the fiber is seen in Figure 14, which includes two spectra. The lower spectrum was collected before and the upper spectrum was collected after a one meter piece of chalcogenide fiber was decoated over 25 cm, or about one fourth of the total length. The strong absorption feature at 2190 cm^{-1}, marked CO, results from absorption of radiation propagating within the core by the core material. This feature does not change after the fiber is decoated. The absorption features centered near 2450, 2850, 2920, 3100 and 3290 cm^{-1}, marked Cl, are due to absorption of the evanescent wave by the plastic

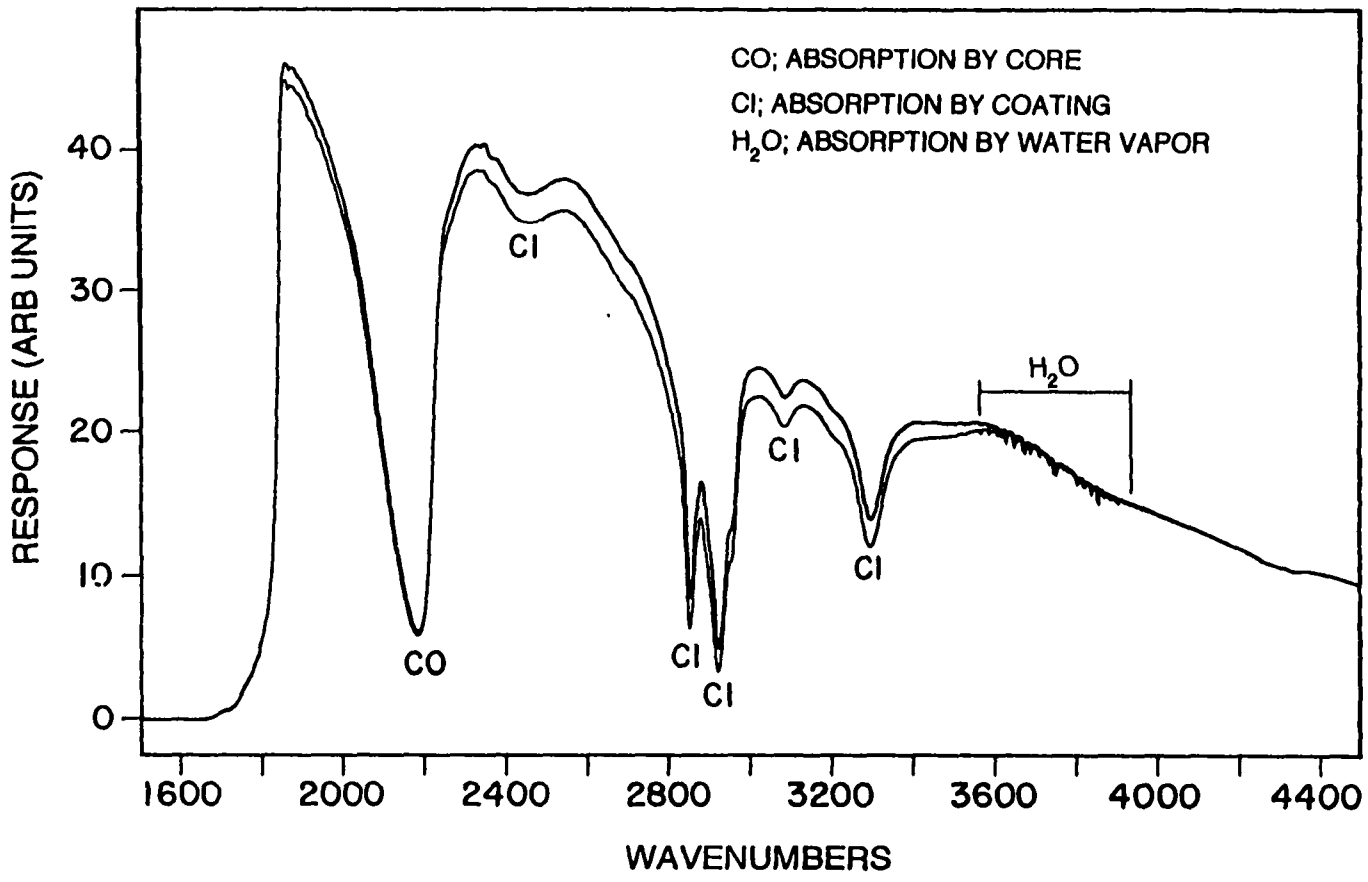

Figure 14. Interferometer instrument response, with coated and decoated sensing portion of optical fiber. Absorption features are marked as CO and Cl for core and cladding respectively.

coating. A significant portion of the spectral range is affected by decoating the fiber. The magnitude of the change depends on how much of the fiber is decoated. Consequently it is essential to experimentally obtain background spectral data at the beginning of an experiment, after the fiber has been decoated and placed in the position and the configuration for which the experimental measurements will be made. Absorption by a small amount of water vapor in the optical path within the spectrometer chamber is seen between 3600 and 3900 cm^{-1}. Although the spectrometer chamber was continuously purged with gaseous nitrogen, a small amount of water vapor is always present.

Before taking the data of the evanescent wave absorption spectra by aluminum hydroxide, the background spectra were collected with the decoated fiber as an integrated part of the optical path, but without the presence of a sample. Figure 15 shows two curves with and without aluminum hydroxide sample. A two meter length of chalcogenide optical fiber was used for this background spectrum with 15 cm of its length decoated. Several features of this curve are noteworthy. The sharp cutoff near 1700 cm^{-1} is due to the response of the InSb detector. The slow decline from 2000 cm^{-1} toward larger wavenumbers is a result of the combined response of the detector and beamsplitter. As mentioned above, the strong absorption feature, marked A, results from the core and the weaker absorption features, marked B, are due to absorption of the evanescent wave by the plastic coating. Absorption by a small amount of water vapor is also shown in this Figure 15.

Once background spectra were obtained, spectra with the decoated portion of the fiber embedded in aluminum hydroxide, $Al(OH)_3$, was collected. Figure 15 also shows a spectrum with pure aluminum hydroxide powder covering about 15 cm of the decoated optical fiber. To insure that the aluminum hydroxide powder covered the decoated portion of the fiber uniformly, a paste composed of acetone and aluminum hydroxide was packed

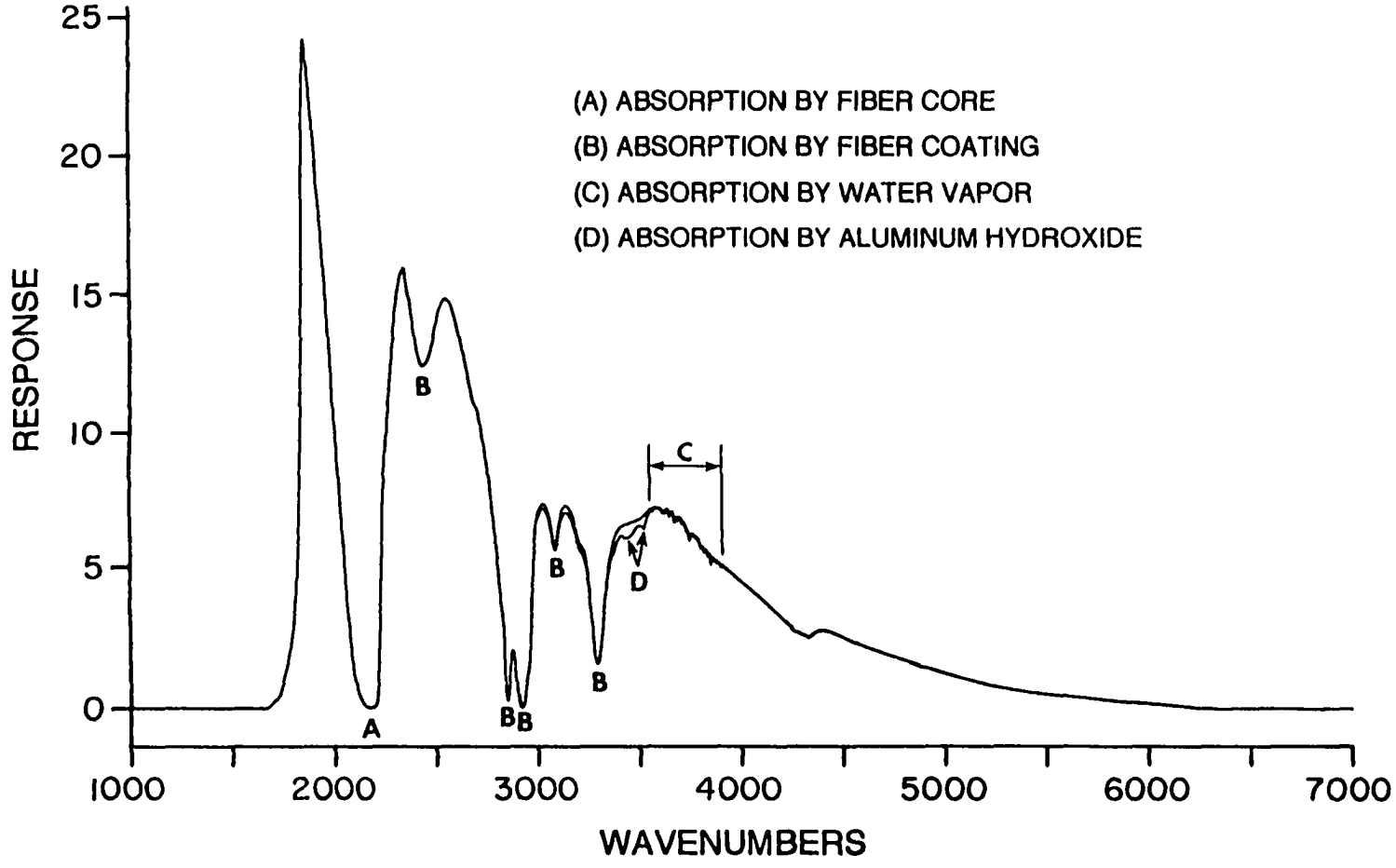

Figure 15. Interferometer, optical fiber instrument response, with and without the aluminum hydroxide.

around the fiber core. Spectral data was collected after the acetone had evaporated. The two relatively small absorption features near 3440 and 3525 cm^{-1}, marked D, are $Al(OH)_3$ spectral features.

In the spectral region above 4000 cm^{-1} there is no absorption by the core, the coating or water vapor. Therefore the spectral response above 4000 cm^{-1}, may be used to judge the stability of the experimental setup over time. A small changes in response may be associated with instrumental drift, such as changes in source temperature or flow rate of the cooling water for the infrared source, which may occur over time. This is useful to note, because in field applications instrumental effects are harder to control than in laboratory situations. Consequently, the background spectrum and the spectrum collected with the sample in place should be the same in this region. As may be seen in Figure 15, the two curves coincide in this spectral range.

With the same procedure, spectra of pure powdered aluminum hydroxide were collected by varying some experimental parameters:

(a) different resolution; 4, 8, 16, and 32 cm^{-1},

(b) data collecting time to increase the number of coadded scans of moving mirror,

(c) length of fiber core covered by sample.

Signal to noise ratio was investigated depending on the data collecting time and resolution to find suitable setting required for minimum data collection time, while preserving the shape of the spectral features and achieving sufficient instrumental sensitivity.

Figure 16 shows the spectra collected with and without a powdered sample of natural corrosion of aluminum in contact with approximately 15 cm of decoated fiber core, with a total fiber length about one meter. The sample was obtained from an aircraft component corroded by the natural environment. As mentioned in section 5.4, the sample was prepared by grinding the corrosion to form a fine powder, mixing the powder with

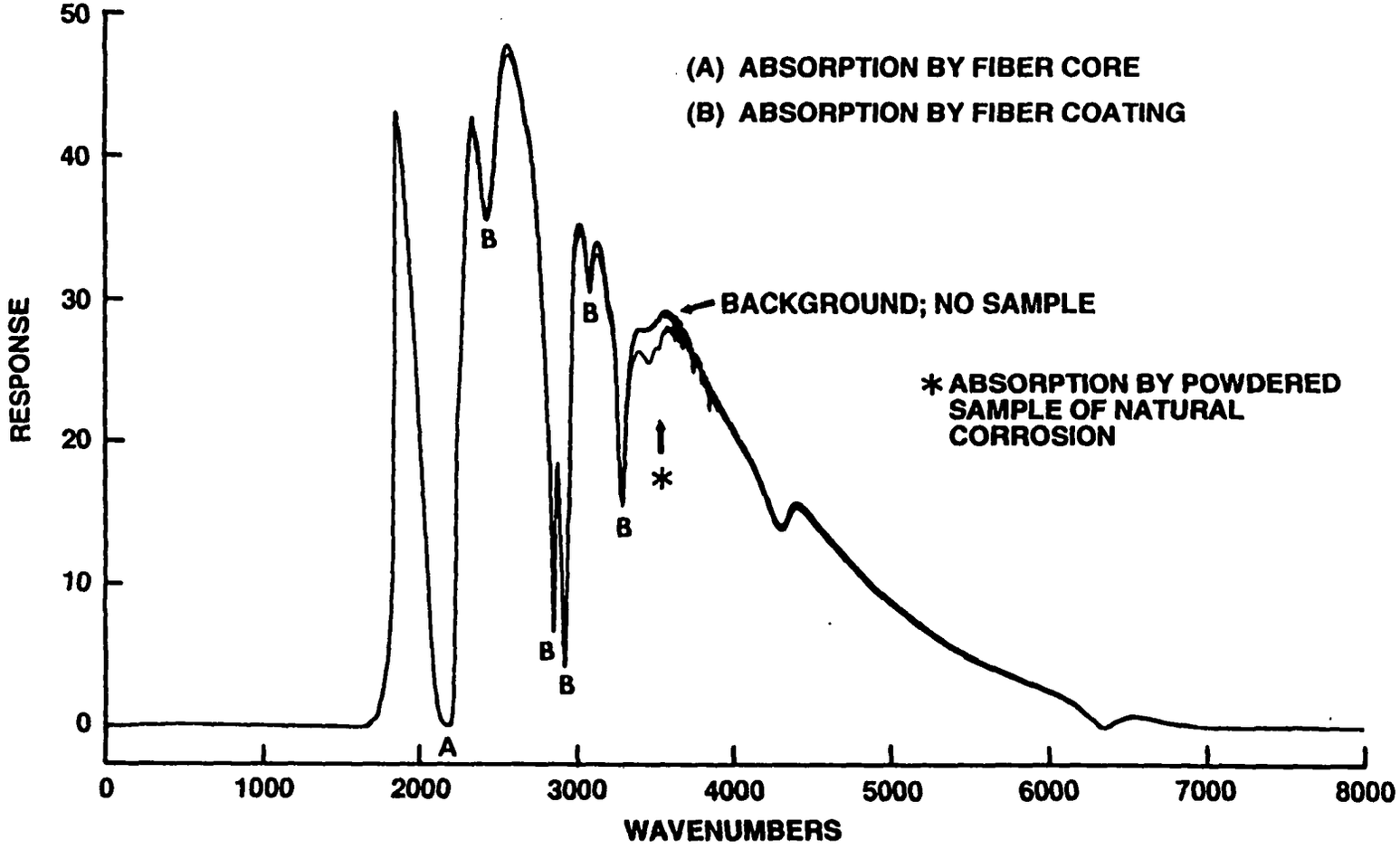

Figure 16. Interferometer, optical fiber instrument response, with and without a powdered sample of natural corrosion of aluminum

acetone to form a paste and packing the paste around the core. The spectral data was collected after the paste was dry. Absorption by the corrosion products covers a very broad spectral range, from about 3650 cm^{-1} and extending to shorter wavenumber, and has a continuum-like character. However there are two relatively strong absorption peaks which are clearly associated with the corrosion sample, located near 3463 and 3525 cm^{-1}. Repeated experiments suggest that the very small absorption in the spectral regions at approximately 1900 cm^{-1} and between 2400 and 2600 cm^{-1} is also due to the corrosion products in the sample.

For comparison and as a reference technique for quantitative analyses, spectral data of the same samples with a zinc selenide ATR element were collected. Figure 17 is the spectrometer response recorded using the liquid nitrogen cooled MCT detector. The broad features at the low wavenumber decline is by the zinc selenide crystal and the high wavenumber decline is the response of the beamsplitter and detector. Absorption by a small amount of water vapor and gaseous carbon dioxide within the spectrometer is also indicated.

The lower curve in Figure 17 shows a spectrum of a pure powdered sample of aluminum hydroxide. The powdered aluminum hydroxide was mixed with acetone to form a paste and placed on the zinc selenide ATR element. As the figure shows the $Al(OH)_3$ absorption covers a broad spectral range, from near 800 cm^{-1} up to about 3650 cm^{-1}. There are several clearly identifiable $Al(OH)_3$ absorption peaks in this spectral range. At the low wavenumber end of the spectrum there is an absorption peak near 750 cm^{-1}, as well as a slightly larger peak near 1000 cm^{-1} and a much larger peak near 1031 cm^{-1}. At high wavenumber end of the spectrum there are several identifiable $Al(OH)_3$ peaks in the range

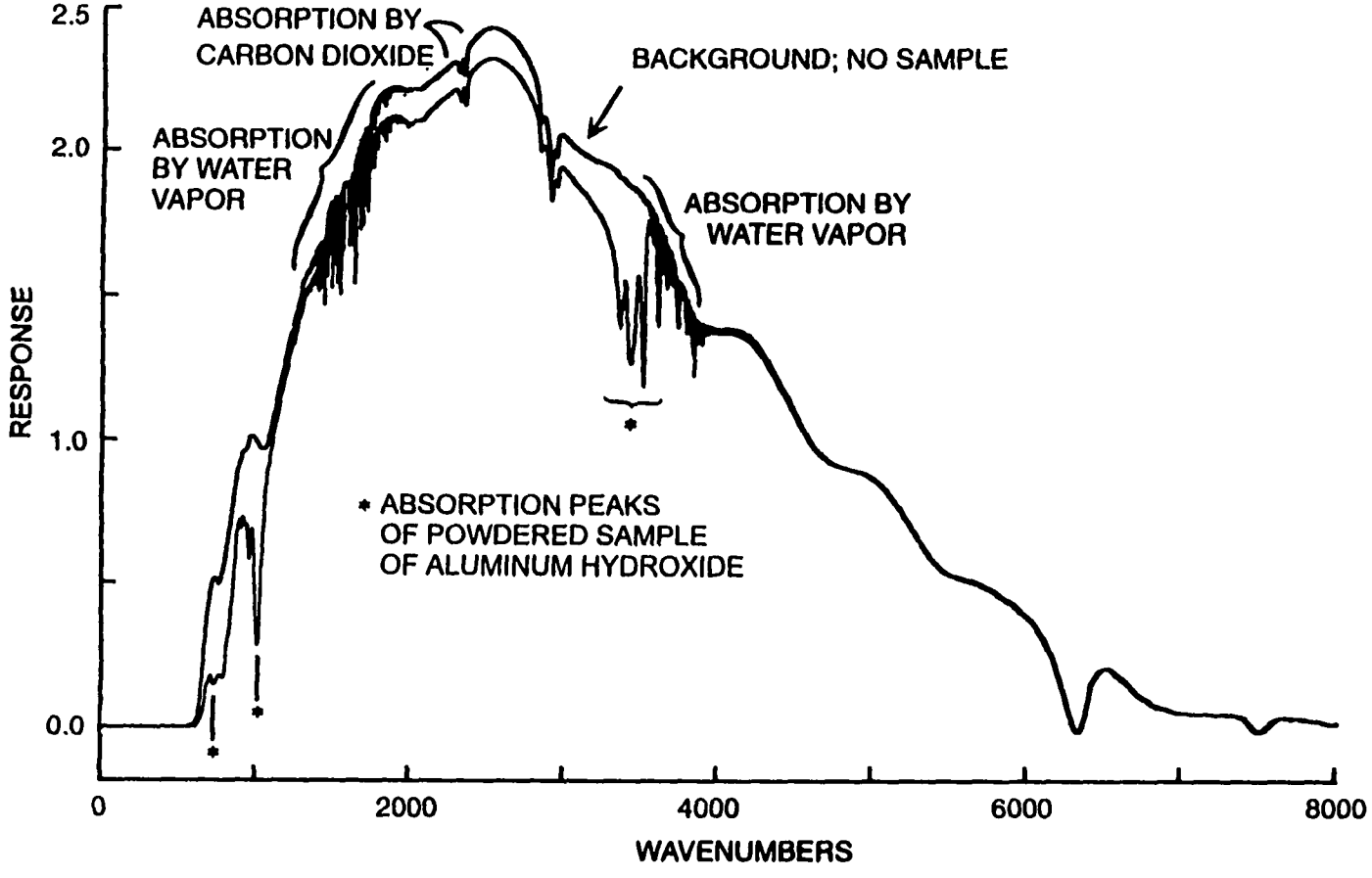

Figure 17. Interferometer, zinc selenide ATR crystal instrument response, with and without a powdered sample of aluminum hydroxide.

of 3300 to 3650 cm^{-1}. The strongest peaks, at 1031 and 3525 cm^{-1} are also identifiable in the data in Figure 17.

The lower curve in Figure 18 was collected with the same powdered sample of natural corrosion which was used to collect the data in Figure 16. The powdered sample was again mixed with acetone to make a paste and placed in contact with the exposed face of the zinc selenide ATR crystal. The strong absorption by the broad overlapping bands of the powdered corrosion products covers the spectral range between 800 and 3650 wavenumbers. In particular there are three clearly identifiable absorption peaks which are attributable to the corrosion products. The first peak is found near 1060 cm^{-1}. In addition the same two peaks which are seen in Figure 16, near 3463, and 3525 cm^{-1} are also found in Figure 18.

The absorption due to the sample of natural corrosion shown in Figure 18 is much greater than that shown in Figure 16. This is largely a result of the difference between the penetration depth and surface areas of the two ATR elements, the zinc selenide crystal and the decoated chalcogenide optical fiber. The data in Figure 16 was collected with the corrosion sample in contact with a decoated portion of the 500 micrometer diameter fiber core, over approximately 35 cm of its length. This gives a surface area of about 2.2 cm^2. The sample surface area of the zinc selenide crystal is approximately 8 by 70 mm or 5.6 cm^2 or approximately 2.5 times larger than the sample surface area of the optical fiber.

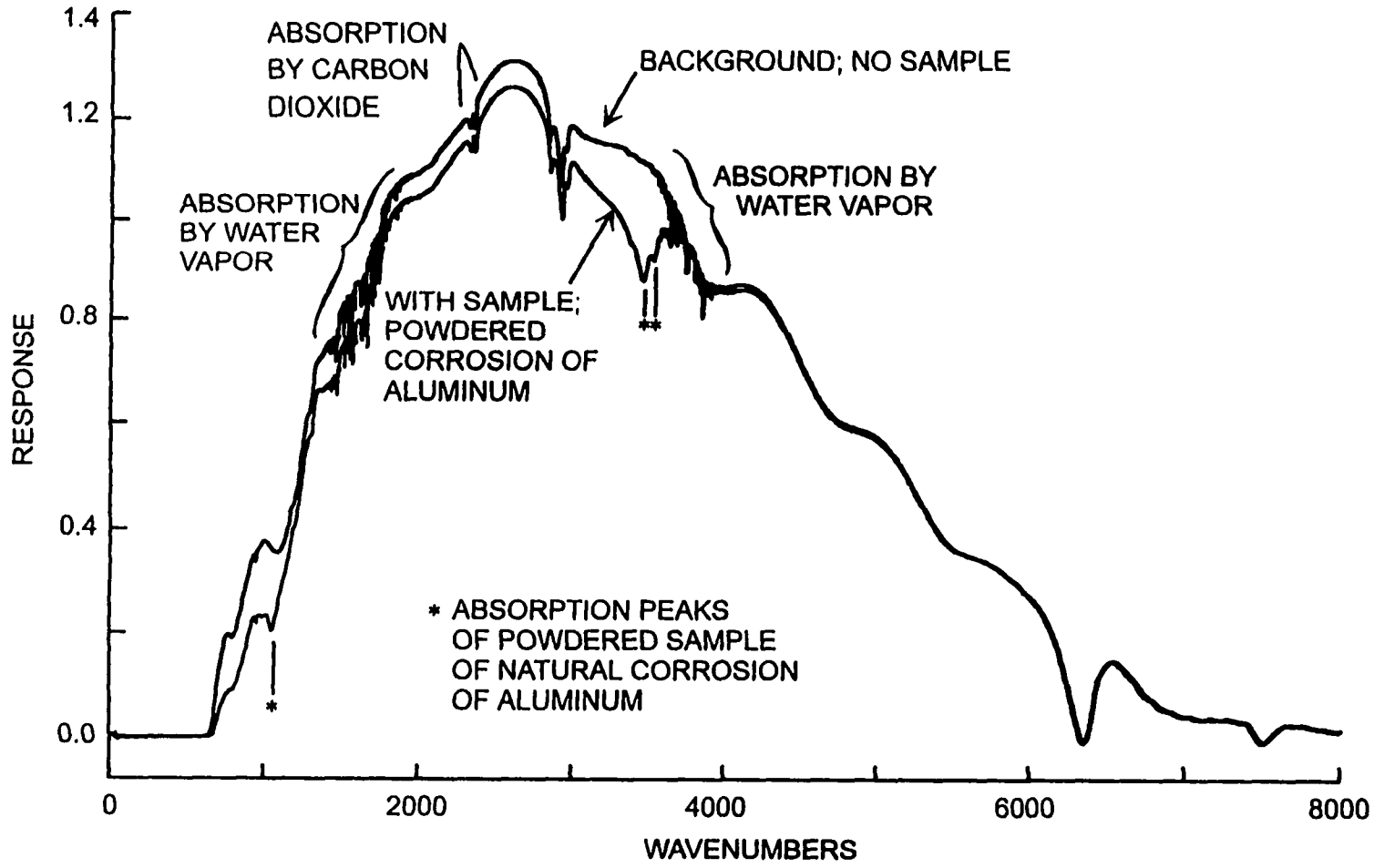

Figure 18 Interferometer, zinc selenide ATR crystal instrument response, with and without a powdered sample of natural corossion.

CHAPTER 6

RESULTS AND DISCUSSION

Results are presented in this chapter to demonstrate that optical fiber FTIR techniques may be used to detect corrosion in industrial applications of aluminum and aluminum alloys. The technique is able to detect small amounts of corrosion in contact with the fiber core. Instrumental sensitivity of detection of aluminum hydroxide for corrosion sensing and retrieval of absorption index for quantitative analyses using optical fibers are described. Comparison of the spectral data collected using optical fiber and a zinc selenide ATR crystal element, as a reference or standard technique is presented.

6.1 ABSORPTION FEATURES OF ALUMINUM HYDROXIDE

Evanescent wave absorption spectra were collected with a decoated fiber core embedded in pure powdered aluminum hydroxide.[40] An example of a spectrum collected with approximately 15 cm of the decoated portion of the fiber embedded in dried $Al(OH)_3$ is shown in Figure 19. The upper curve is the background and the lower curve shows absorption by $Al(OH)_3$. Both spectra were collected at 4 cm^{-1} resolution with the coaddition of 512 scans. The strong absorption features at 3440 and 3525 cm^{-1} mark the band centers of two of the $Al(OH)_3$ vibrational transitions. In this region the signal to noise ratio of the measurement is greater than 200 to 1. Weak absorption in the wings of the vibrational transitions may also be seen over the spectral range from 3000 cm^{-1} to 3650 cm^{-1}. for example at 3130 cm^{-1}. There are five identifiable $Al(OH)_3$ vibrational transitions with band centers in the range from 3350 cm^{-1} to 3650 cm^{-1}. Two weaker vibrational bands are centered near 3400 cm^{-1}. They are located on the steep slope of the absorption

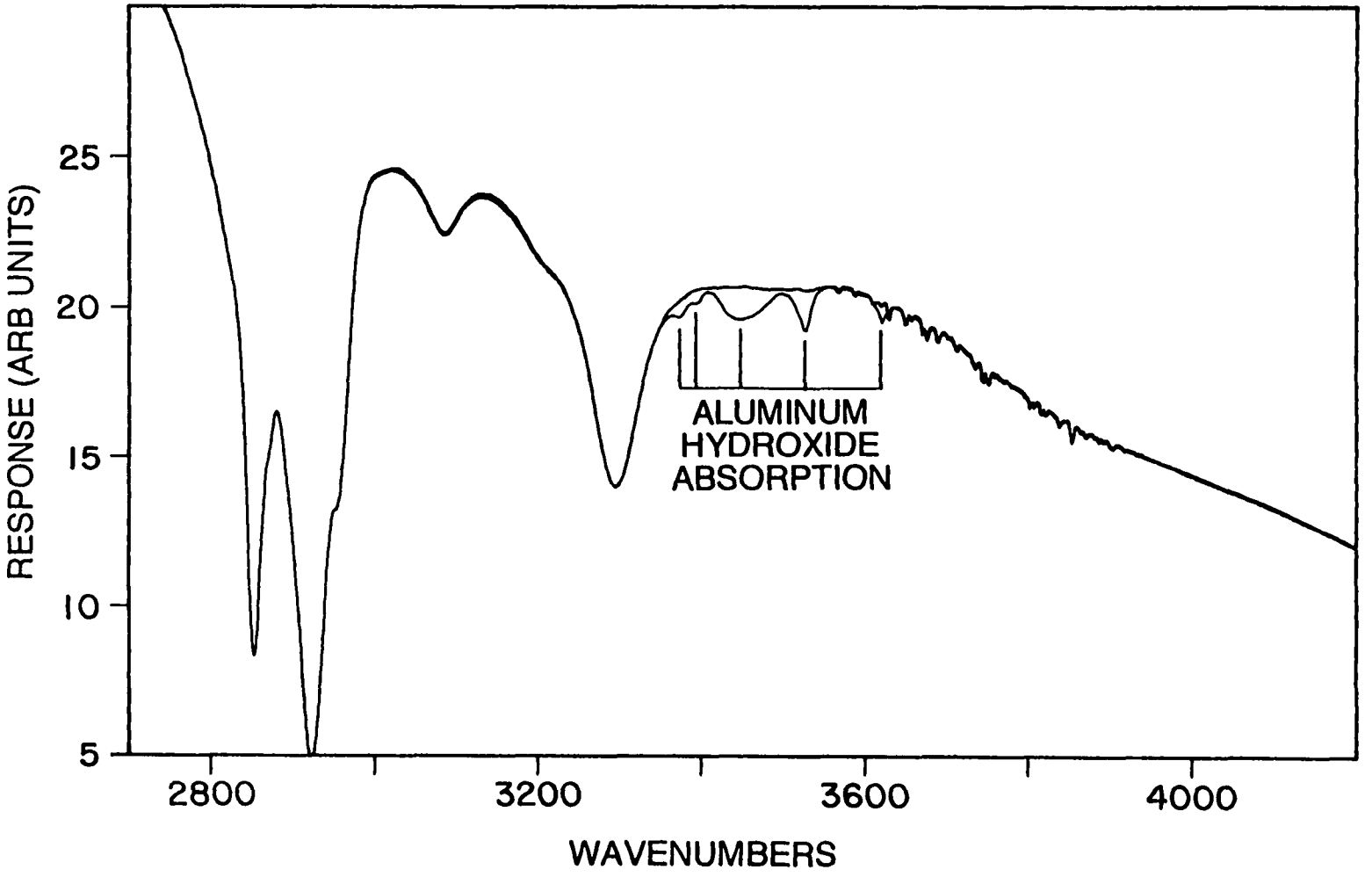

Figure 19. Evanescent wave absorption spectra, instrument response with and without a pure aluminum hydroxide sample.

feature centered at 3300 cm^{-1}. This feature is due to evanescent wave absorption by the coating. The other $Al(OH)_3$ absorption band is partially hidden by the water vapor absorption and is located at 3620 cm^{-1}. Since the $Al(OH)_3$ absorption features are not very strong, the background instrument spectral response must be well characterized so that accurate transmittance spectra can be computed. This means that the background spectrum must be collected after the fiber has been decoated and positioned to make the remote measurements.

Transmittance spectra of dry powdered aluminum hydroxide are shown in Figure 20, including absorption data of five resolvable $Al(OH)_3$ absorption features, at 3374, 3394, 3440, 3525 and 3620 cm^{-1}.[41] The relative positions, transition strengths and widths of these absorption features qualitatively agree with the reference spectral data which is found in the Sadtler Spectra.[42] The bottom curve in Figure 20 was collected with 4 cm^{-1} resolution, the highest resolution possible with the interferometer. The signal to noise ratio of this spectrum is greater than 200 to 1. The effect of spectral resolution may be seen in this figure, which includes data collected at 4, 8, and 16 cm^{-1} resolution. The background for each curve was collected at the same resolution, so that the absorption by water vapor in the spectral range 3600 to 3900 cm^{-1} would ratio out. To keep the instrumental sensitivity the same at all three resolutions, the spectral data at 8 cm^{-1} was collected by coadding 256 scans, and the data at 16 cm^{-1} was collected by coadding 128 scans. The shape and degree of overlap in the spectral data at 4 and 8 cm^{-1} are almost the same. At 16 cm^{-1}, the two weak $Al(OH)_3$ features at 3374 and 3394 cm^{-1} are more blended as a result of the lower resolution. This suggests that for field applications, approximately 8 cm^{-1} is adequate to accurately record the $Al(OH)_3$ absorption features. One practical advantage in using a low

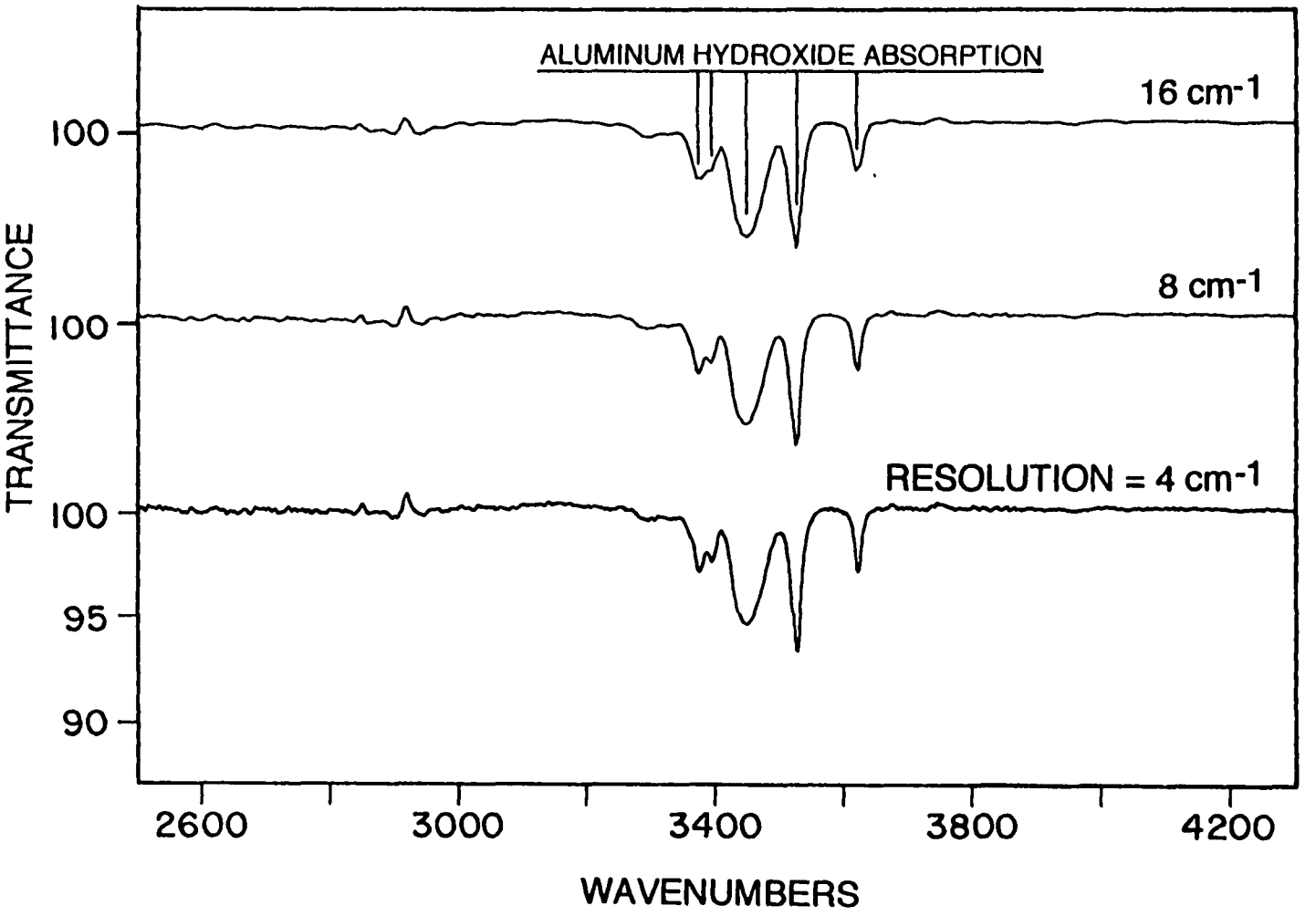

Figure 20. Transmittance spectra of dry powdered aluminum hydroxide in contact with decoated fiber.

resolution is that the sensitivity is improved while decreasing the total data collecting time.[37] Also, lower resolution smooths out the relatively sharp water vapor spectral lines that overlap and obscure the $Al(OH)_3$ spectral feature at 3620 cm^{-1}.

Absorption spectral data of water, aluminum hydroxide paste was collected to simulate in a controlled way the field application of this technique. In a field experiment, aluminum hydroxide as a corrosion product of aluminum occurs in the presence of water. Simply detecting the presence of liquid water may indicate the initiation of corrosion, which might then be prevented. Of course, once aluminum hydroxide corrosion has formed the water may subsequently evaporate. The spectral signatures of liquid water and aluminum hydroxide overlap, because in both H_2O and $Al(OH)_3$, absorption of the infrared evanescent wave is occurs in an OH stretch mode. This may hamper both qualitative detection and quantitative analyses of aluminum hydroxide spectral signatures. For quantitative analyses it then becomes necessary to know the strength and the spectral distribution of the liquid water transmittance, or absorptance (one minus the transmittance).

In addition, the spectral transmittance, or absorptance, of liquid water and aluminum hydroxide together is not a simple superposition of the absorptance of each.[41] This may be seen in the spectral data of Figure 21. This figure includes a time sequence of transmittance spectra, collected at approximately equal increments of time, over a period of several hours. The spectra have been separated for clarity. The increment of time between each spectrum was approximately one hour. The sequence begins with the bottom spectrum, curve 1, which was collected just after the water - aluminum hydroxide paste was placed around the fiber core. The sequence ends with the top curve, curve 9, which is a spectrum of dry aluminum hydroxide collected after all of the water had evaporated.

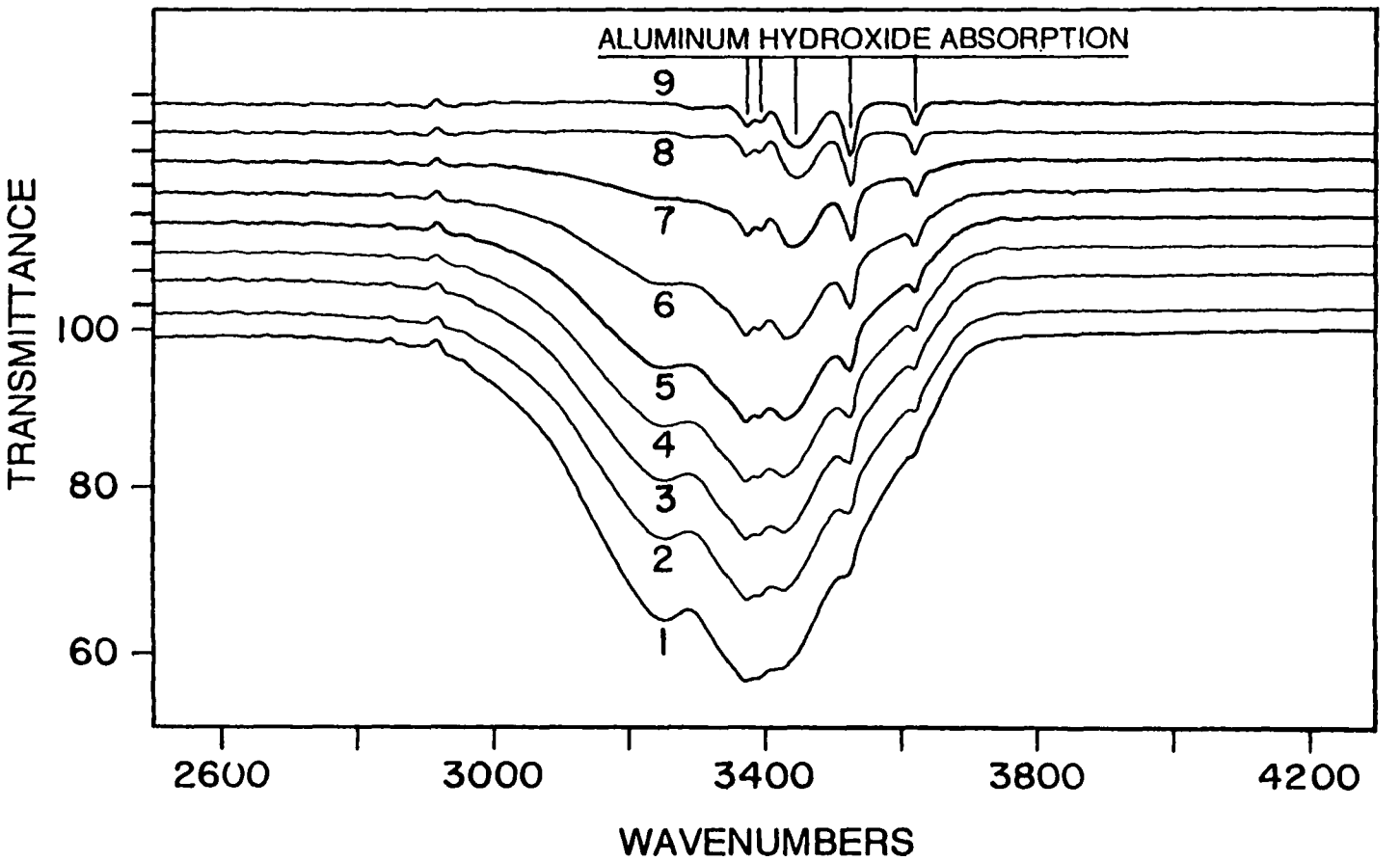

Figure 21. Time sequence of spectra of a paste of water and aluminum hydroxide in contactwith decoated fiber.

At the beginning of the experiment the absorptance of liquid water is large, and the absorptance of the aluminum hydroxide is small. As the water evaporates, the absorptance of the aluminum hydroxide increases. The data in Figure 22 reveals this effect (The discussion here is in terms of absorptance, which is easily observed and measured from Figure 22, rather than absorbance, a more common unit. However, the conclusion is unchanged). The data in Figure 22 are measurements of water and aluminum hydroxide absorptance made at the center of the $Al(OH)_3$ spectral feature at 3525 cm^{-1}. The presence of liquid water prevents the aluminum hydroxide from absorbing the evanescent wave. The water may hold the powdered sample of $Al(OH)_3$ in suspension away from the fiber core. Also the liquid water will change the index matching factor M and reduce the penetration depth of the evanescent field.

Data collected with the zinc selenide crystal as the ATR element is independently valuable in several ways. As mentioned before, section 1.3, the magnitude of evanescent field, using crystal ATR element can be more easily characterized mathematically than optical fibers and can be used as a reference technique.[43] Figure 23 is transmittance data collected using both a decoated chalcogenide optical fiber (upper curve) and the zinc selenide crystal (lower curve) as the ATR element. The five identifiable $Al(OH)_3$ peaks which have been reported before,[40] at 3374, 3394, 3440, 3525, and 3620 cm^{-1} are clearly recognizable from the both curves. The upper curve was collected with approximately 15 centimeters of the decoated 500 micrometer diameter fiber core in contact with pure powdered aluminum hydroxide. This gives a sample surface area of 2.4 cm^2. The sample area of the zinc selenide ATR crystal is about 5.6 cm^2. The ratio of the sample surface area is (5.6 cm^2/2.4 cm^2) or about 2.3. The ratio of the absorptance at the strong spectral feature at 3440 cm^{-1} is about (0.29/0.055) or about 5.3. The difference in the ratio of

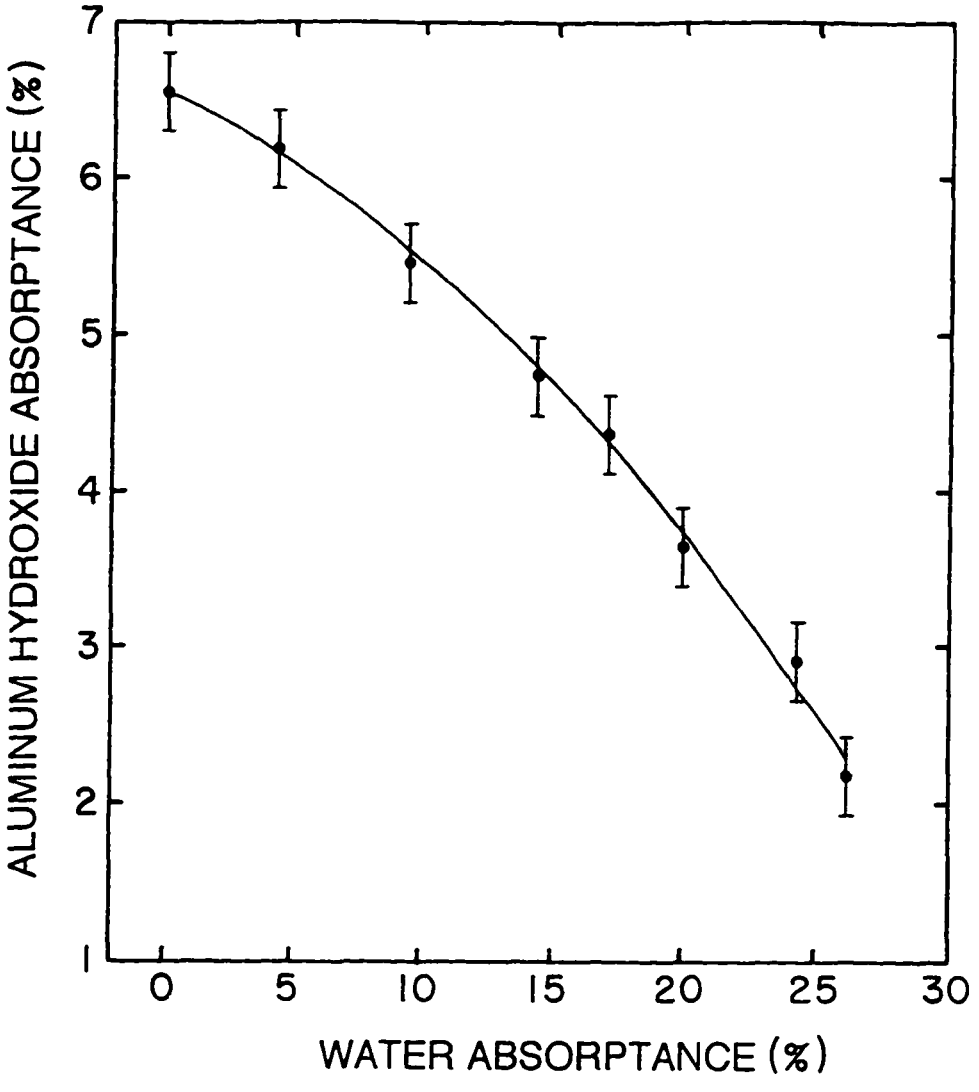

Figure 22. Absorptance of aluminum hydroxide and water.

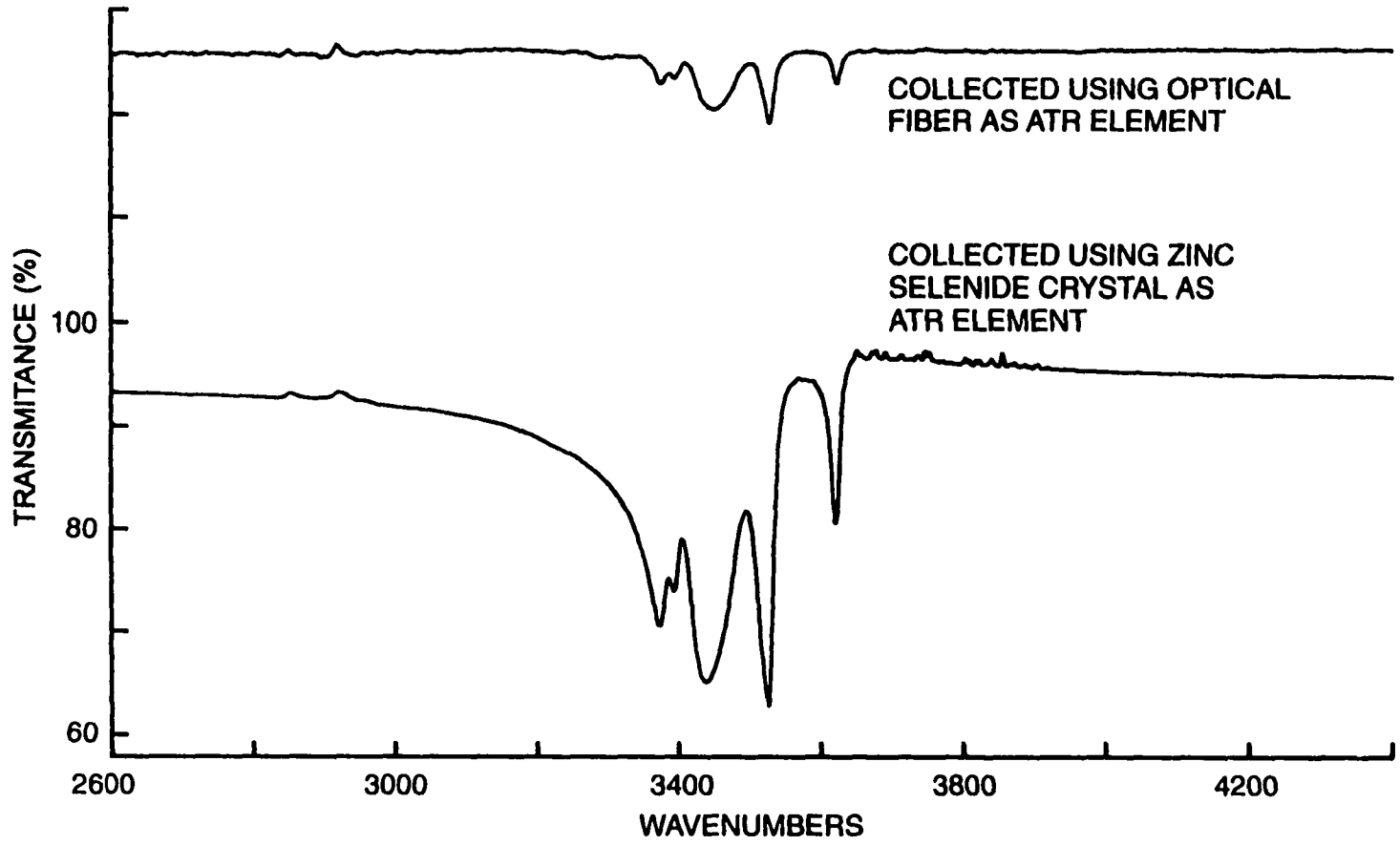

Figure 23. Transmittance spectra of aluminum hydroxide with optrical fiber and a zinc selenide crystal as an ATR element.

surface areas when compared to absorptance is the difference in angle of incidence and effective thickness. In the zinc selenide crystal the angle of incidence is much closer to the critical angle.

In the full transmittance spectrum collected with the zinc selenide crystal ATR element using MCT detector, two strong peaks at 750 and 1031cm^{-1} are detected (see Figure 17). These are not seen in the transmittance spectrum collected with the optical fiber because of the cutoff frequency of InSb detector (see Figure 15). So the comparison here is limited to the 3000 wavenumber region only. The $Al(OH)_3$ features in the lower wavenumber region also indicates that data collected with fibers covering a larger spectral range may be useful for quantitative analyses of $Al(OH)_3$ absorption. For this purpose, the evanescent wave absorption data with optical fiber was collected using narrow band MCT detector instead of InSb detector. The MCT detector has sufficient detectivity in the lower wavenumber region to record the absorption by aluminum hydroxide and natural corrosion products, but absorption by the fiber core and cladding in that spectral range prevents the data from being usable for quantitative analyses.

In the lower curve in Figure 23, the one-hundred-percent line is sloped slightly in the range 3600 to 4000 cm^{-1}. This effect results from a change in the amount of water vapor in the optical path and small instrumental changes during the period between the collection of the background spectrum and the sample spectrum. In practice monitoring will take place over a long period of time, during which the experimental conditions may change. Changes in the experimental conditions may cause shifts and distortions of the one-hundred-percent line. These effects will not interfere with qualitative analyses but quantitative spectral analyses may be affected by systematic errors. In Figure 23 the small perturbation of the one-hundred-percent line does not obscure the significant absorption on the low wavenumber side of the five aluminum hydroxide absorption peaks. The far wing

absorption is not noticeable in the upper curve collected with the optical fiber which has a smaller sample surface area. It is assumed that the powdered sample covers the same fraction of the crystal sample surface area and the optical fiber sample area.

6.2 EVANESCENT ABSORPTION BY LIQUID WATER

Evanescent wave absorption spectra of liquid water was collected with an optical fiber probe. Liquid water is studied because the liquid covers the sample surface area of the fiber completely and uniformly which may not be the case for solid powdered samples. To confine the water so that precise lengths of fiber was covered by the liquid, 6 mm x 6 mm grooves were machined into a block of aluminum to hold the liquid. Four grooves, 5,10,15, and 20 cm in length were used. Small openings at the end of each groove allowed the fiber to be placed into each groove submerged in the liquid in a straight configuration without touching the walls of the groove. Small rubber seals at the end of each groove prevented the liquid from leaking out of the groove around the fiber. This experimental arrangement, using a liquid as a sample and precisely controlling the length of the fiber in contact with the sample, provided the highest degree of control over the experimental parameters that was possible. Two sets of spectral measurements were made with this experimental setup using liquid water as the sample.

The spectral data are shown in Figures 24 and 25. The transition is the (100) transition which is an O-H stretch mode having characteristic P and R branches. In the gaseous form, this transition is centered at about 3652 cm^{-1}. No rotational line structure is possible in the liquid form, so that 4 cm-1 resolution is sufficient to faithfully record the spectral features. The spectra have good characteristics for determining absorptance and absorbance. The signal to noise ratio is high and the background (100% transmittance) is flat on both sides of the spectral features. This indicates that the experimental conditions

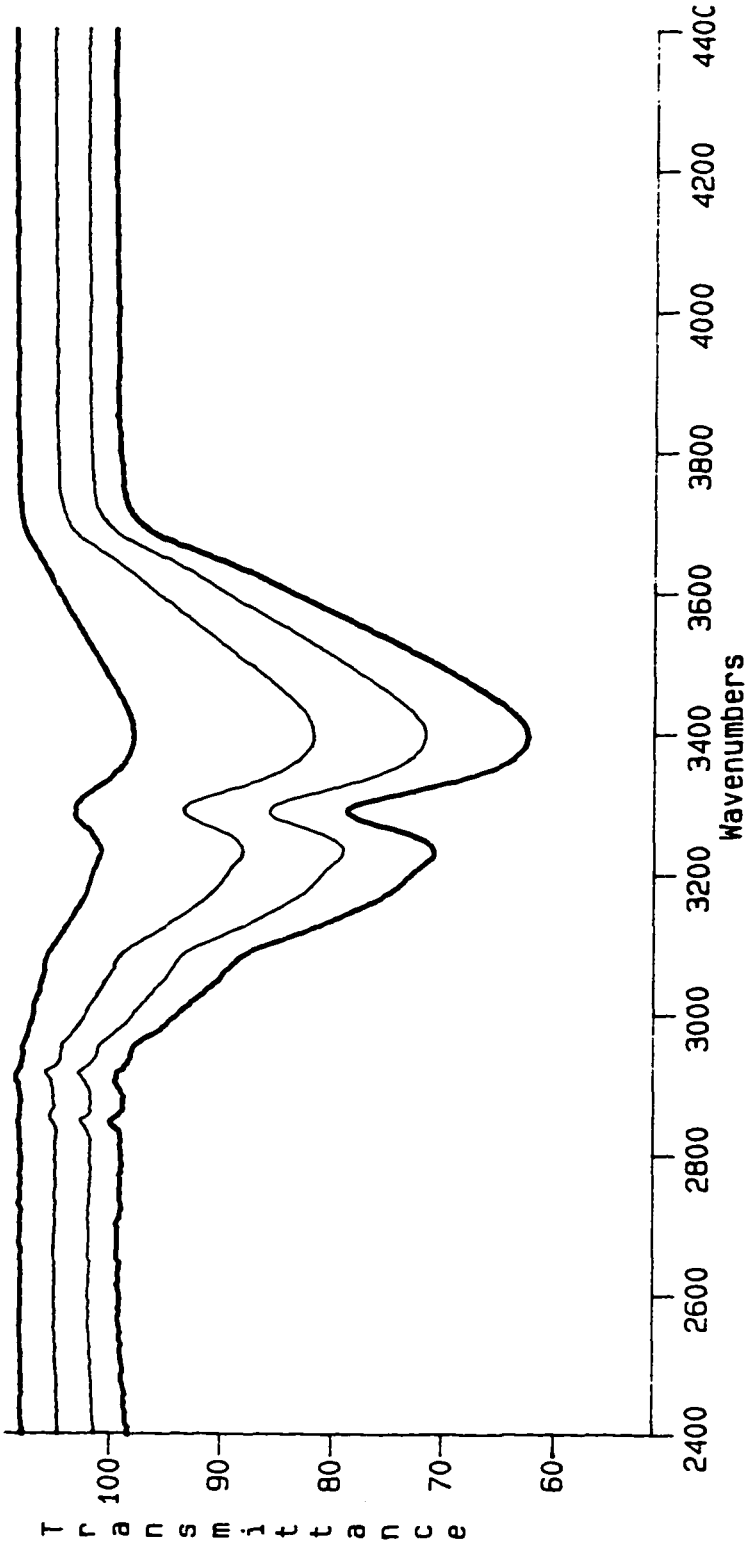

Figure 24. Transmittance spectra of liquid water collected with optical fiber.

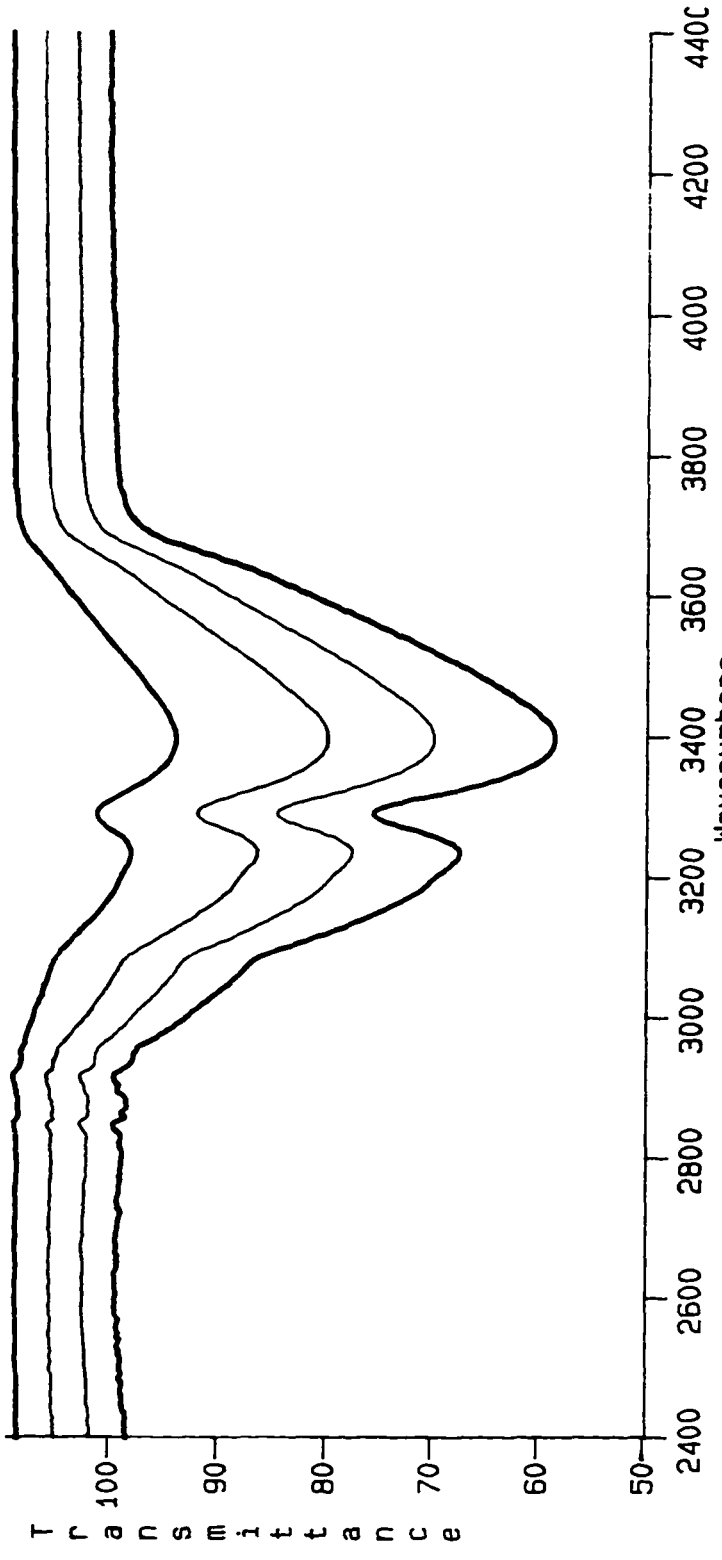

figure 25. Transmittance spectra of liquid water collected with optical fiber.

remained stable during the entire data collection. The magnitude of absorptance (1-Transmittance) is large enough to produce non-linear absorptance and therefore absorbance was also determined.

Figure 26 shows absorptance as a function of fiber length covered by the water sample. The pattern of absorptance verses fiber length is the same in the two data sets with a noticeable systematic shift in the absorptance values of one data set relative to the other. The origin of the systematic shift may result from differences in the way radiation is launched into the fiber in the separate experiments. This will change the sample effective thickness. Since the magnitude of the absorptance is not small and therefore may not be a linear function of the fiber length covered by the sample. To check this absorbance has also been determined as shown in Figure 27. The straight line in each case is a linear least square fit to the absorbance data. The data is approximately linear in each case and this is the behavior expected from Beer's law.

It should be noticed that from the Figures 26 and 27 for absorptance and absorbance that the ratio (absorptance/absorbance) is approximately 2.3 only for the first two points. This is the ratio expected from log(Transmittance) or optical depth if the transmittance data increases linearly as a function of the length of fiber covered by the sample. It can be concluded then that the spectral data, in Figure 24 and 25, are in the linear region of growth of absorptance as a function of fiber length covered by the liquid water sample only for the first two spectra.

6.3 ABSORPTION FEATURES OF NATURALLY CORRODED SAMPLE

Corrosion of aluminum alloys produces various amounts of corrosion products. The vibrating rotating O-H bonds may experience a very different environment in aluminum hydroxide than in natural corrosion. Figure 28 is an example of spectral data of

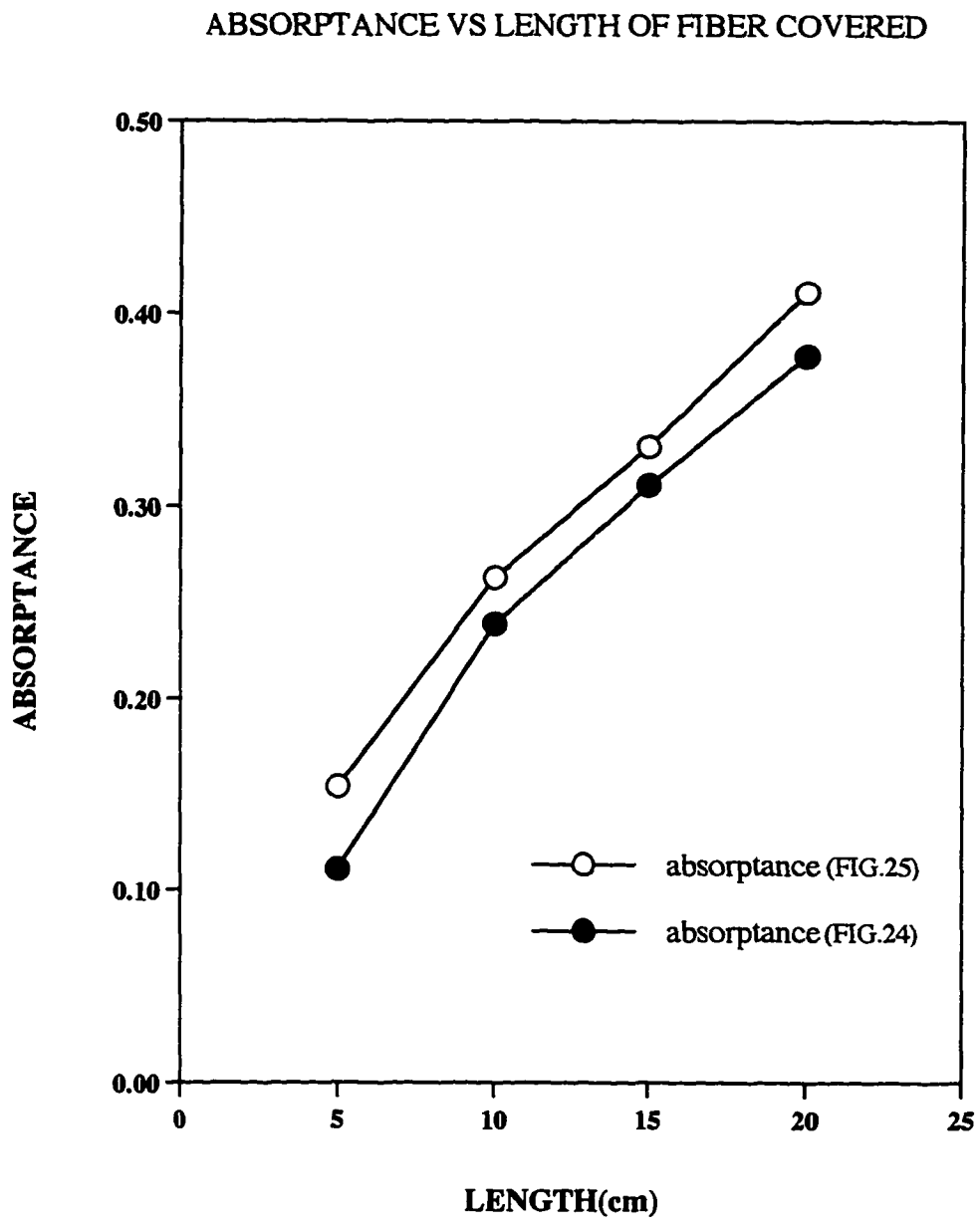

Figure 26. Absortance at 3400 cm^{-1} versus length of fiber covered by liquid water.

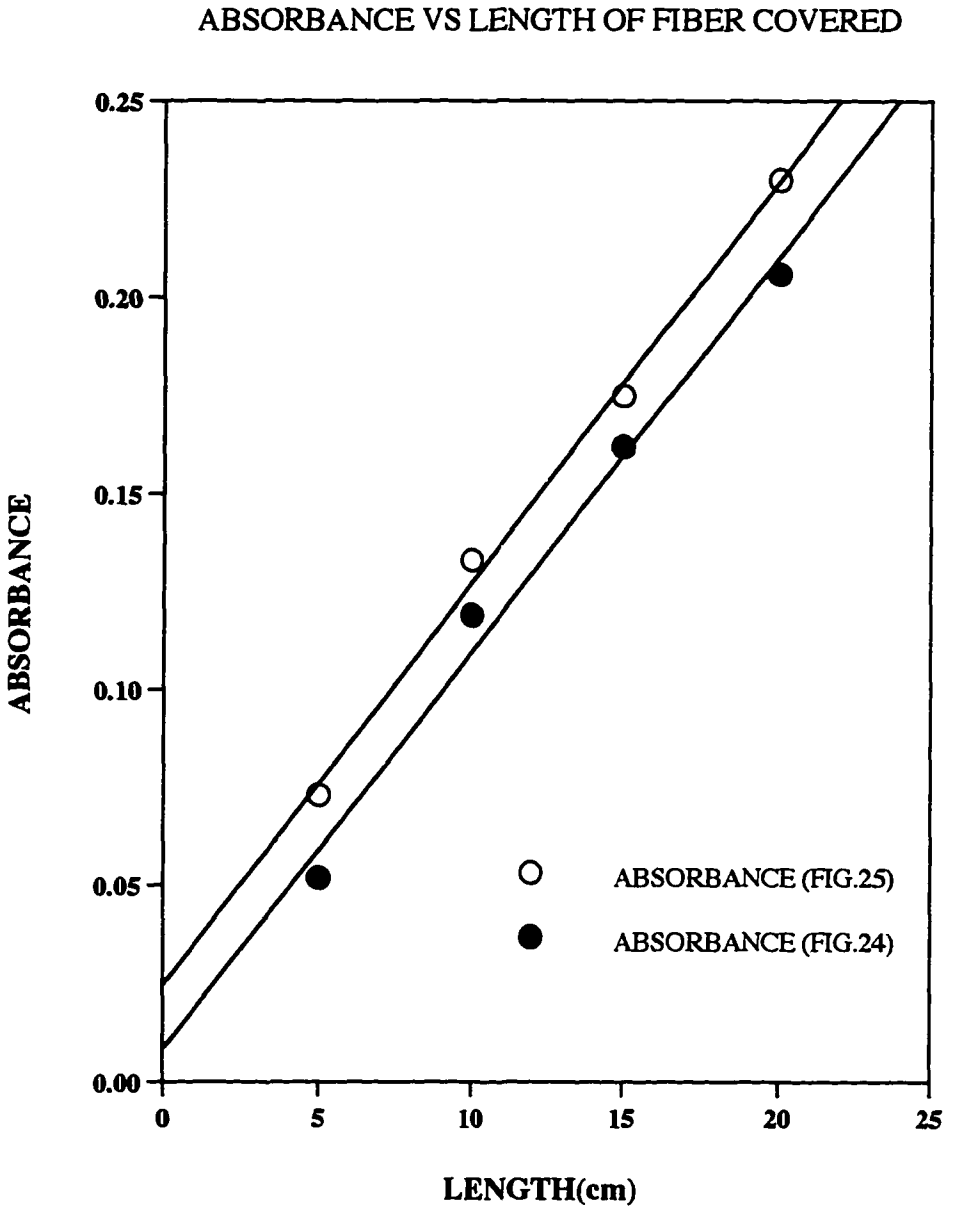

Figure 27. Absorbance at 3400 cm^{-1} versus length of fiber covered by liquid water.

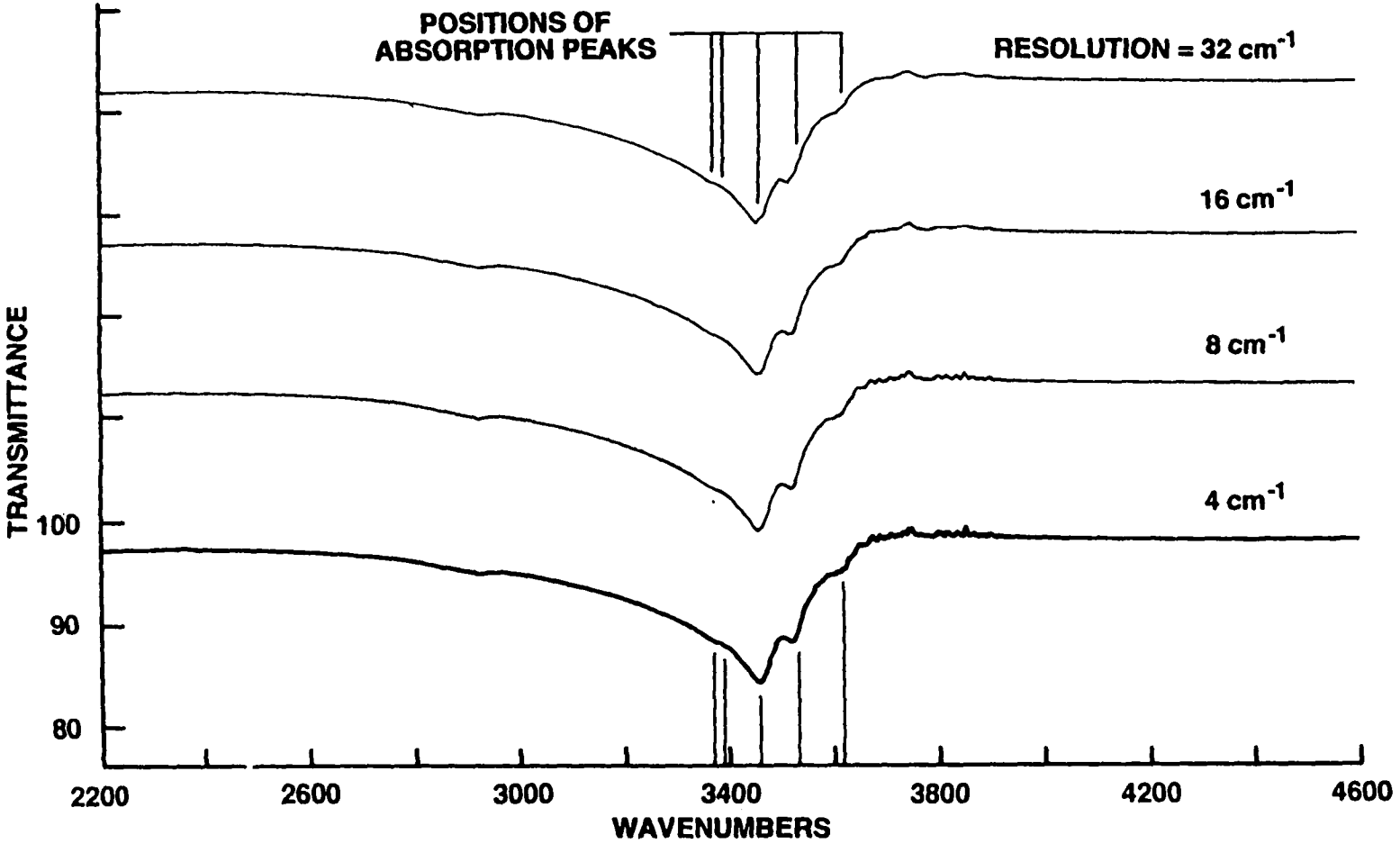

Figure 28 Transmittance spectra of natural aluminum corrosions collected using a zinc selenide crystal as an ATR element.

naturally corroded sample collected using the zinc selenide crystal ATR optical element.[44] The figure contains four spectra which have been separated vertically for clarity and ease of comparison. The same powdered sample of natural corrosion and the same experimental conditions were used. The data is recorded at four resolutions, 4, 8, 16, and 32 cm^{-1}. The spectra clearly shows that 16 cm^{-1} is adequate to faithfully record the details of the natural corrosion spectrum. Very little information is gained by using 8 cm^{-1}. However instrumental sensitivity is proportional to resolution[37], and a factor of four in instrumental sensitivity is gained by using 16 cm^{-1} compared to 4 cm^{-1} resolution. Consequently 16 cm^{-1} resolution should be adequate for field measurements of aluminum corrosion.

Figure 29 is transmittance data of natural corrosion sample of the aluminum alloy, which is the ratio of the single beam background and sample data (see Figure 16 and 18). The upper curve was collected with a powdered sample of natural aluminum corrosion using an optical fiber and the lower curve was collected using the zinc selenide ATR crystal with the same sample. Each spectrum has a residual water vapor signature. This causes a small perturbation of the transmittance of the corrosion product. Both transmittance spectra have a constant one-hundred-percent line beyond 4000 cm^{-1}. This indicates that the experimental conditions were stable over the time period between the collection of the background and the sample data. The strongest two peaks, at 3463 and 3525 cm^{-1} are identifiable in both spectra. The peak observed near 1060 cm^{-1} in Figure 18 can not be compared here due to the cutoff frequency of InSb detector.

With the current experimental setup for monitoring natural aluminum corrosion, as seen in Figure 18, the largest absorption by the corrosion sample occurs at the 2.9 micrometer wavelength spectral region. The presence of the fiber coating absorption feature

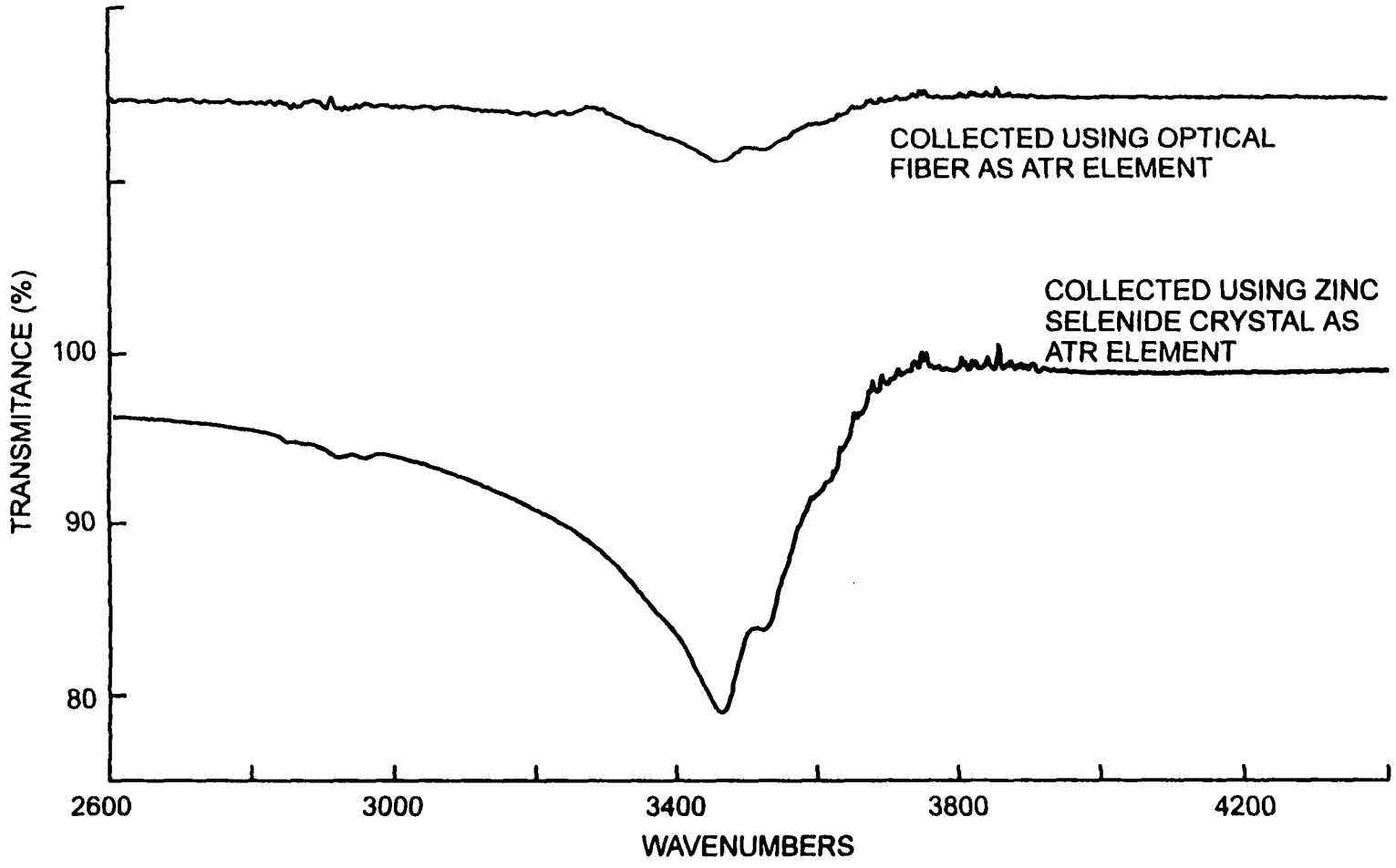

Figure 29. Transmittance spectra of natural corrosion sample with optical fiber and a zinc selenide crystal as an ATR element.

at 3290 cm^{-1} does not in general interfere with the signal and ratios out when a transmittance spectrum is calculated. However, there are two relatively strong water vapor transitions, v_1 and v_3 centered near 3652 cm^{-1} and 3756 cm^{-1} respectively.[45] As a result, residual water vapor in the purged spectrometer optical path will introduce a spectral signature. The water vapor amount often changes over time. Hence a residual water vapor spectral signature may be present in the transmittance spectrum near 3600 cm^{-1}.

A comparison of the spectral data of aluminum hydroxide and natural corrosion samples collected using zinc selenide ATR element is shown in Figure 30. The upper curve is from Figure 23 and the lower curve is from Figure 29. The shapes of the absorption profiles in the wings of the two spectra, below 3300 cm^{-1}, are quite different, suggesting different interaction molecular dynamics which causes the shape to be different. Also a shorter relaxation time causes the spectral features to be broader in the natural corrosion sample. This suggests the presence of other corrosion products in addition to $Al(OH)_3$ and the molecular interaction of these other products with aluminum hydroxide molecules.

Figure 31 compares the spectral data of the pure powdered sample of aluminum hydroxide (upper curve), and the powdered sample of natural corrosion of aluminum alloy (lower curve). Both spectra were collected with an optical fiber. The aluminum hydroxide spectrum is the same as Figure 23; the spectrum of the powdered natural corrosion is the same as Figure 29. The signal to noise ratio of both spectra is greater than 400 to 1. The absorptance is about four to six percent. This is a result of the small fiber sample surface area, about 2.4 cm^2 over 15 cm of the decoated fiber length. Consequently, the absorptance signal-to-noise ratios are about 30:1 for the aluminum hydroxide data and 20:1 for the data of the natural corrosion product. The experimental parameters, including resolution and data collection time were the same for both spectra. Each spectrum includes 512 coadded

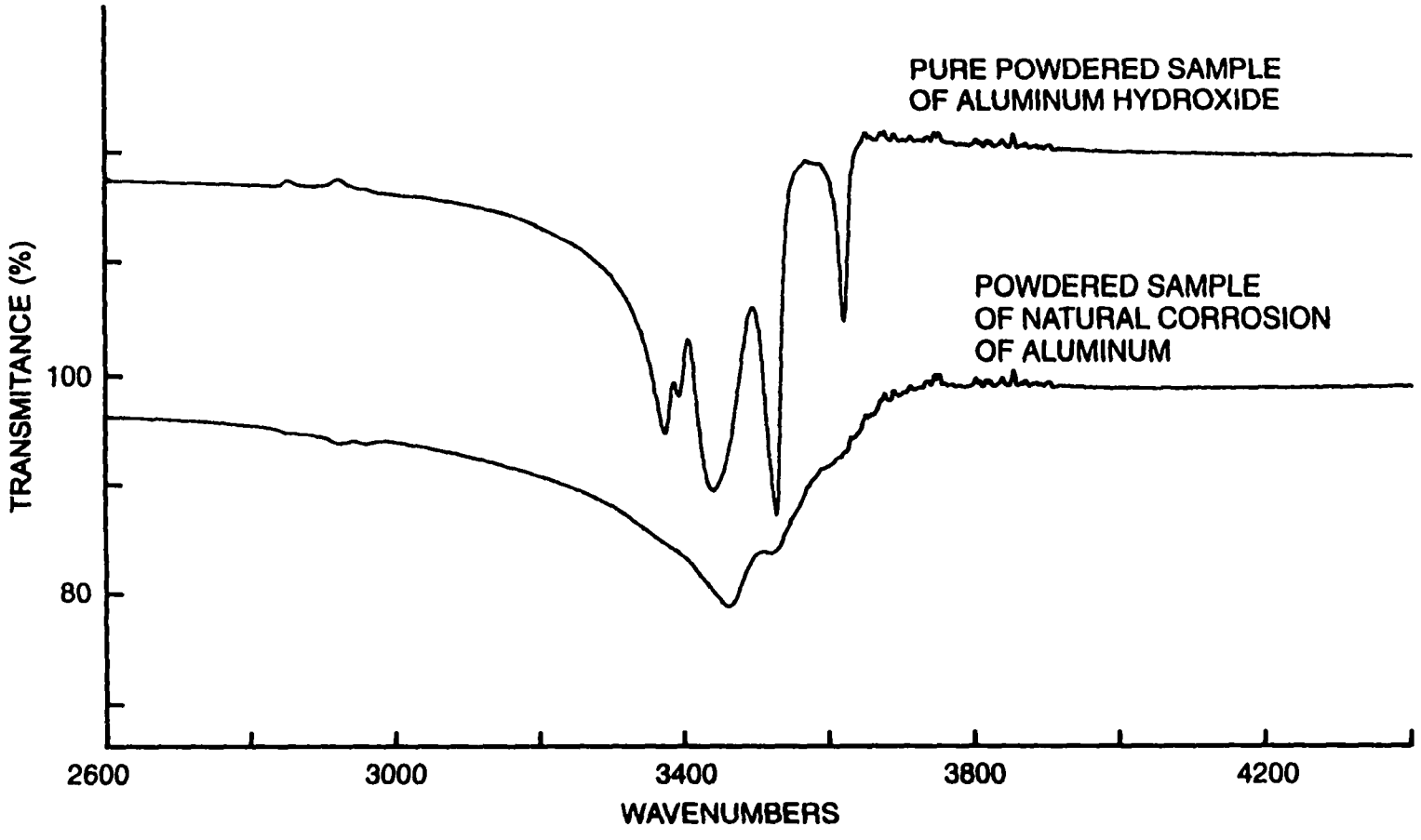

Figure 30. Transmittance spectra of aluminum hydroxide and natural corrosion collected with a zinc selenide crystal as an ATR element.

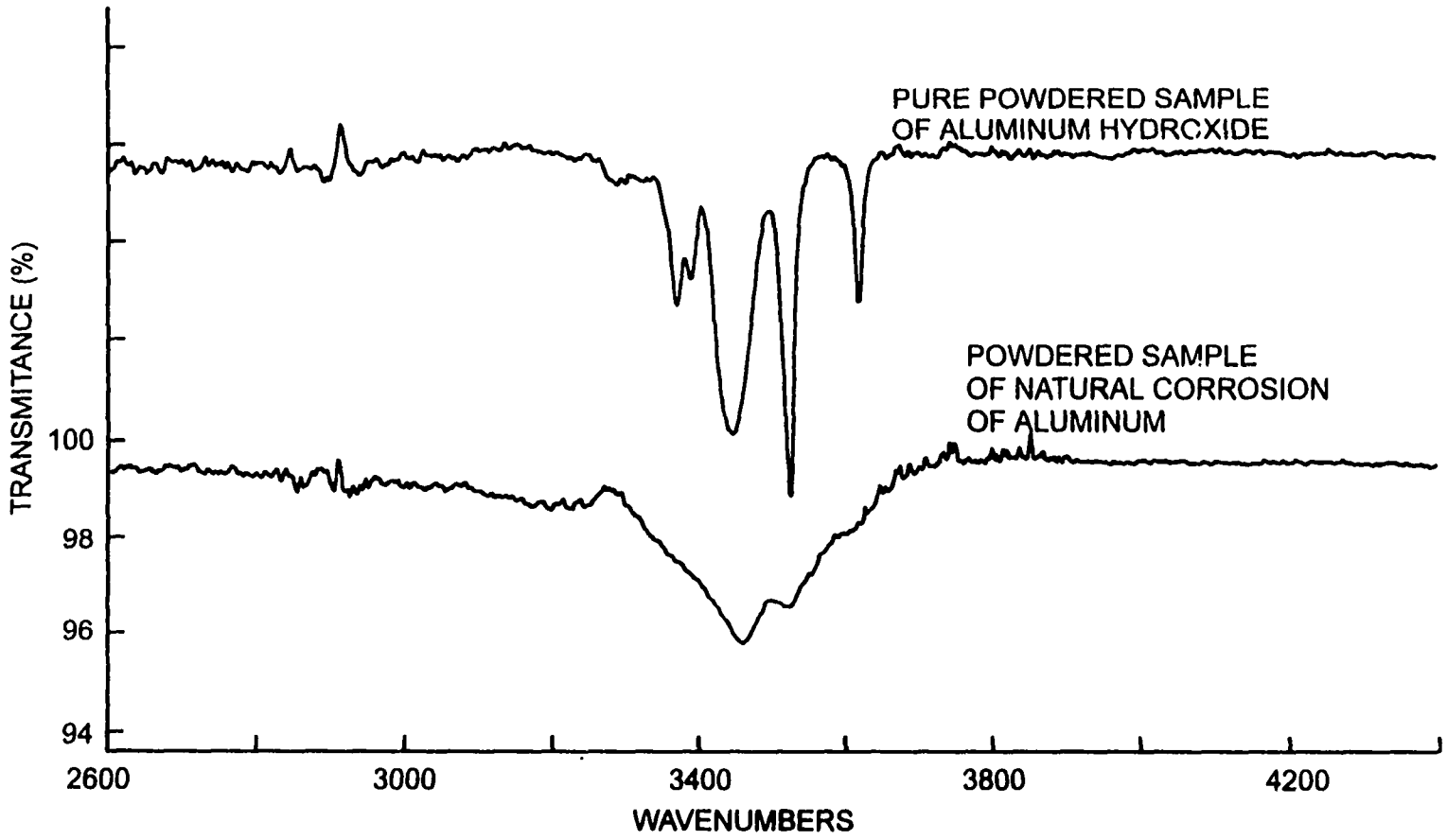

Figure 31. Transmittance spectra of aluminum hydroxide and natural corrosion collected with an optical fiber as an ATR element.

interferograms. In the two cases the length of decoated fiber and overall fiber length were the same. Therefore, the sensitivity of the two measurements were the same.

The spectra in Figure 31 suggest that it should be possible to detect aluminum hydroxide covering 8 mm^2 (= 2.4 $cm^2/30$) and natural corrosion covering 12 mm^2 (=2.4 $cm^2/20$) of the optical fiber. If 8 cm^{-1} resolution is used to detect aluminum hydroxide instead of 4 cm^{-1} then the sensitivity is doubled and aluminum hydroxide covering only 4 mm^2 of fiber could be detected. Similarly, if 16 cm^{-1} resolution is used natural corrosion may be detected covering 3 mm^2 of the fiber surface.

Figure 32 contains three spectra of different powdered samples of natural corrosion, collected under the same experimental conditions, obtained using the zinc selenide ATR element. The spectra are separated vertically for clarity. Spectrum (A) was collected with a sample scraped from an aircraft frame component. Spectra (B) and (C) were collected with samples from two separate locations on a large corroded wing section of another aircraft. Materials such as glue, sealer, primer and paint, were unavoidably collected with the corrosion samples. Consequently the samples are not pure samples of corrosion. This causes the magnitude of the absorptance to be different in each case. Also, the corrosion occurred on different aluminum alloys, and under different environmental conditions. However, the positions and the widths at half maximum of the spectral features are the same in all three spectra. This suggests that the corrosion product is the same in each case. This consistency suggests that spectral data of a pure sample of natural corrosion in which the amount of corrosion is known, may serve as a reference for quantitative analyses of any sample of natural corrosion, either in the laboratory or in-situ.

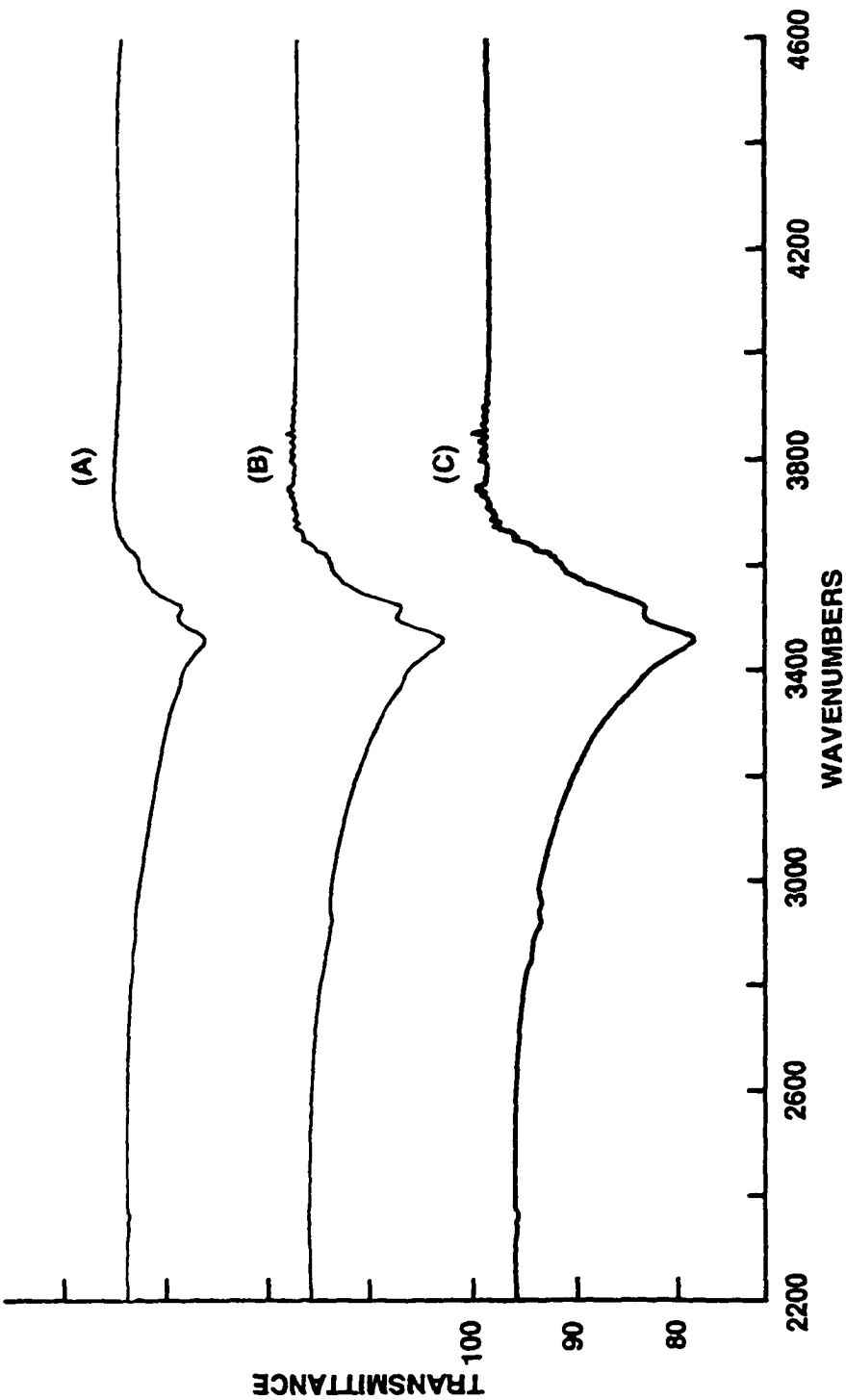

Figure 32. Transmittance spectra of various natural corrosion samples collected with a zinc selenide crystal.

6.4 CALCULATION OF EFFECTIVE THICKNESS D_{eff}

Effective thickness is defined as the film thickness of the sample material which would give the same absorbance as that obtained in a transmission measurement at normal incidence (see section 4.7). Effective thickness of each experimental case was calculated to compare the spectra of a natural corrosion sample collected using an optical fiber and a zinc selenide crystal ATR element.

As shown in Figure 33, Spectrum (D) of natural corrosion product was collected using an optical fiber and spectrum (E) of the same natural corrosion sample was collected using crystal ATR element. Both spectra were collected by coadding 512 scans at 4 cm^{-1} resolution. The powdered sample covered 35 centimeters of the fiber length, giving the same sample surface area as the zinc selenide crystal. The spectrum collected using the optical fiber shows approximately 3.6 percent absorptance, which is approximately ten times greater that the noise.

If it is assumed that in each case the powder covers the same fraction of the crystal or fiber surface area, the difference in absorptance of the two spectra may be attributed to the difference in the effective thickness. From the figure, the ratio of the absorptance of the two spectra is approximately 3.9; the spectrum with the fiber shows approximately 3.6 percent absorptance, the spectrum with the crystal about 13.9 percent absorptance. It is assumed that ratios of absorptance and absorbance are the same, since the absorptance is small.[46] The difference arises due to the number of reflections of the radiation in the crystal and fiber; seven reflections in the crystal and several hundred reflections in the fiber. Also, the single reflection effective thickness is different in the two cases, because the angle of incidence of the radiation at the interface with the powdered sample is different. In the crystal the angle of incidence is 45°, just above the critical angle of 42°. In the fiber, the radiation propagates within a cone covering incident angles from about 81° up to grazing

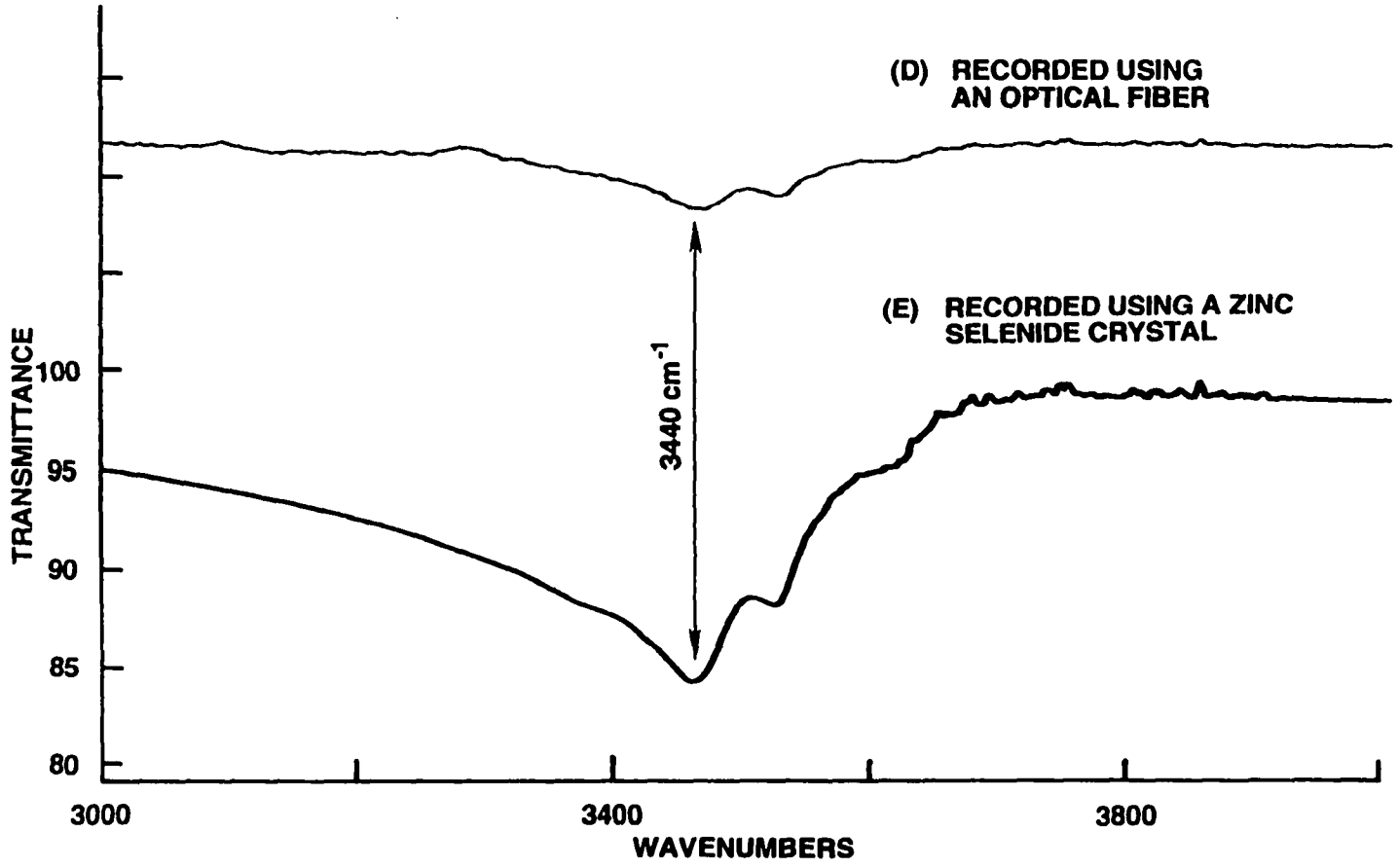

Figure 33. Transmittance spectra of natural corrosion, with an optical fiber and a zinc selenide crystal as an ATR element..

incidence near 90°, far from the critical angle of 35°. For the angles of incidence in the two cases, the effective thickness may be calculated (see chapter 4).

The approximate expression D_{eff}, equation (80), is applicable in the cases of small absorbance (small κ), at large angles of incidence. Therefore the expression should be applicable to the top spectrum of Figure 33. Assume for the quantities in this equation, the following: $\lambda = 3$ μm, $l = 35$ cm, d= 500 μm, $M' = 0.7$, and $\theta_{AC} = 9°$. The obtained value of the total effective thickness D_{eff} equals 2.8 micrometers.

To confirm the approximation given above, the single reflection effective thickness $d_{eff}(\theta)$ was calculated from the expressions given by equations (69) and (71). Assume that $\kappa < 0.25$. Each value of the effective thickness at each angle must be weighted by $[(l/d) \bullet \text{Tan}(90-\theta)]$ which gives the number of bounces of the radiation in the fiber of diameter d=500 micrometer, over the length l =35 cm, at the angle θ. The weighted values, $[d_{eff}(\theta) \bullet [(l/d) \bullet \text{Tan}(90-\theta)]]$, are summed over θ from 81 to 90 °:

$$D_{eff} = (l/d) \bullet \Sigma_{\theta=81 \rightarrow 90} [d_{eff}(\theta) \bullet \text{Tan}(90-\theta)] \ . \qquad (90)$$

The value of the total effective thickness obtained is D_{eff} = 2.7 micrometers. This is in reasonable agreement with D_{eff} = 2.8 micrometers, the value obtained from the expression given in equation (80).

The calculated effective thickness D_{eff} (= 2.7 μm), is employed in the expression for the absorptance, $A_p = \alpha \bullet D_{eff}$, to confirm that the absorption coefficient is small and the comparison is valid. From the upper curve in Figure 29, at the strongest peak of 3440 cm^{-1}, the sample is approximately 3.6% absorbing, or $A_p \approx 0.036$ in absorptance units. Then it follows that $\alpha \approx A_p/D_{eff} = 0.013$ per micrometer of sample effective thickness. From

equation (77), the corresponding absorption index $\kappa = 0.004$, confirming that κ is small. This confirms the applicability of the approximation in equation (80) to the spectrum in Figure 33.

Considering the case of radiation propagating in the zinc selenide crystal, the value of the absorption index, $\kappa = 0.004$, is too small to effect the magnitude of the effective thickness. The single reflection effective thickness calculated for the crystal d_{eff}(crystal) equals 2.4 micrometers. Since four out of the seven radiation bounces within the crystal are on the crystal- sample interface, the total effective thickness for the crystal is four times as great as the single reflection effective thickness, or D_{eff}(total) = 9.6. Compared with the effective thickness using a fiber, which is 2.7 micrometers as calculated above, the effective thickness using the crystal is approximately 3.6 times larger. Returning to Figure 33, it may be seen that the absorptance in the spectrum using the crystal is approximately 4 times larger than that in the spectrum using the optical fiber. Given the experimental uncertainties, it is concluded from the calculation that the spectral data collected using the two different methods is consistent.

The discrepancy in absorptance between the two experimental spectra shown in Figure 33, based on this theoretical calculation is about 10%. Experimental uncertainties which may contribute to this difference include: uncertainties in the numerical aperture of the optical fiber and crystal ATR optical accessory, and the differences in the fraction of the crystal and optical sample surface area covered by the powdered corrosion sample.

6.5 DETERMINATION OF ABSORPTION INDEX κ

If all of the experimental parameters are known and all of the sample characteristics are known except the absorption index κ, then the general theory for R may be used to

calculate absorptance A_p [=(1-R^b)], assuming a value for κ. κ may then be varied until the calculated and observed absorptance agree.

The basis for the calculations is the general expressions for the parallel and perpendicular components of the Fresnel single reflection reflectivity R_N and R_P as in equations 32 and 38. An example is shown in Figure 34 calculated for n_1 equal to 2.8, the refractive index of the chalcogenide fiber core. A large value of κ was used in the calculation to display the shape of the R_N and R_P curves. Typically κ is less than 0.1. The dependence of the single reflection Fresnel loss (1-R_N) and (1-R_P) is also shown in this figure. Because of the f/1 zinc selenide lens that focuses the radiation on the fiber end, the cone of radiation propagating through the fiber is limited to 9 degrees, between 81 degrees and grazing incidence, 90 degrees. Therefore the experimental reflectivity (R) will be larger than 75 percent for a value of $\kappa < 0.75$ and the single reflection Fresnel loss (absorptance) will be smaller than 25 percent. The fact that R is large and (1-R) is small in the range of 81 to 90 degrees reduces the sensitivity of the technique in its present instrumental form. If it was possible to make angles of incidence close to the critical angle, then as the figure shows, the sensitivity of the technique could be increased by almost a factor of 4.

One of the advantages of crystal ATR evanescent wave absorption spectroscopy, in which the radiation is incident at the crystal-sample interface very close to the critical angle. The zinc selenide crystal has n_1 equal to 2.4 and a critical angle of about 42°. The corresponding curves for R and (1-R) are only slightly different from those shown in Figure 34. The radiation is incident at the crystal-sample interface at an angle of 45 °, very close to the critical angle of 42°. Consequently, the technique is about four times more sensitive for a zinc selenide crystal ATR optical element as than an optical fiber having the same surface area. A 500 micrometer core diameter 35 cm long optical fiber would have

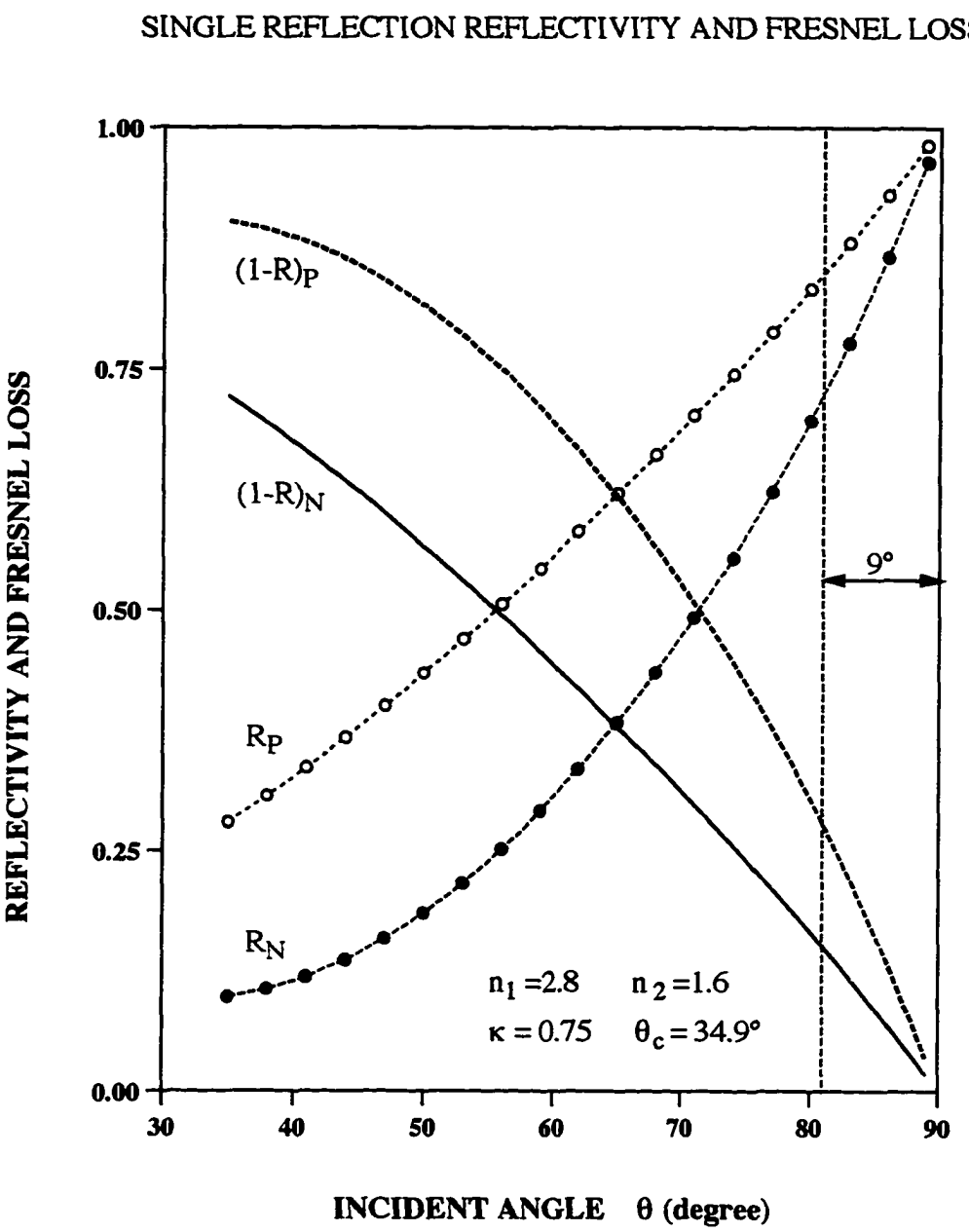

Figure 34. Single reflection reflectivity (R), and Fresnel loss (1-R) for perpendicular and parallel polarization as a function of incident angle θ at fiber core-sample interface.

the same surface area as the crystal. Of course, the crystal must be collocated with the spectrometer and does not have the advantages for remote sensing offered by optical fibers.

If the absorption index is known as a function of wavenumber, then an experimentally measured absorptance spectrum may be analyzed to determine the concentration of the sample. As described in the chapter 4, if the absorption coefficient (α) and the effective thickness (D_{eff}) are known, then the concentration (c) may be computed by fitting the calculated absorptance with the measured absorptance.

Theoretical values of absorption index (κ) and absorption coefficient (α) for aluminum hydroxide and natural corrosion are not known. The absorption index may be determined experimentally by comparing a calculated absorptance versus absorption index curve with an experimentally measured absorptance. The reference technique of crystal ATR-FTIR evanescent wave absorption spectroscopy may be used to make the experimental measurements. The high sensitivity of this reference technique will ensure that the experimentally determined absorption index may be used with high accuracy to analyze data collected using optical fibers.

If the entire surface is covered by absorbing sample, a concentration absorption coefficient product ($\alpha \bullet c$) of one per unit of length of effective thickness can be assumed. A calculation of absorptance versus absorption index for zinc selenide ATR evanescent wave absorption measurement of aluminum hydroxide or natural corrosion is shown in Figure 35. The curves correspond to the perpendicular and parallel polarizations of radiation incident at the crystal-sample interface. For unpolarized radiation the absorptance would be the average of the two separate polarizations.

As the figure shows, for small κ, absorptance versus κ is linear. As κ increases the absorptance approaches 1. Absorptance measured as a function of wavenumber may be converted to a measured absorption index as a function of wavenumber by using Figure

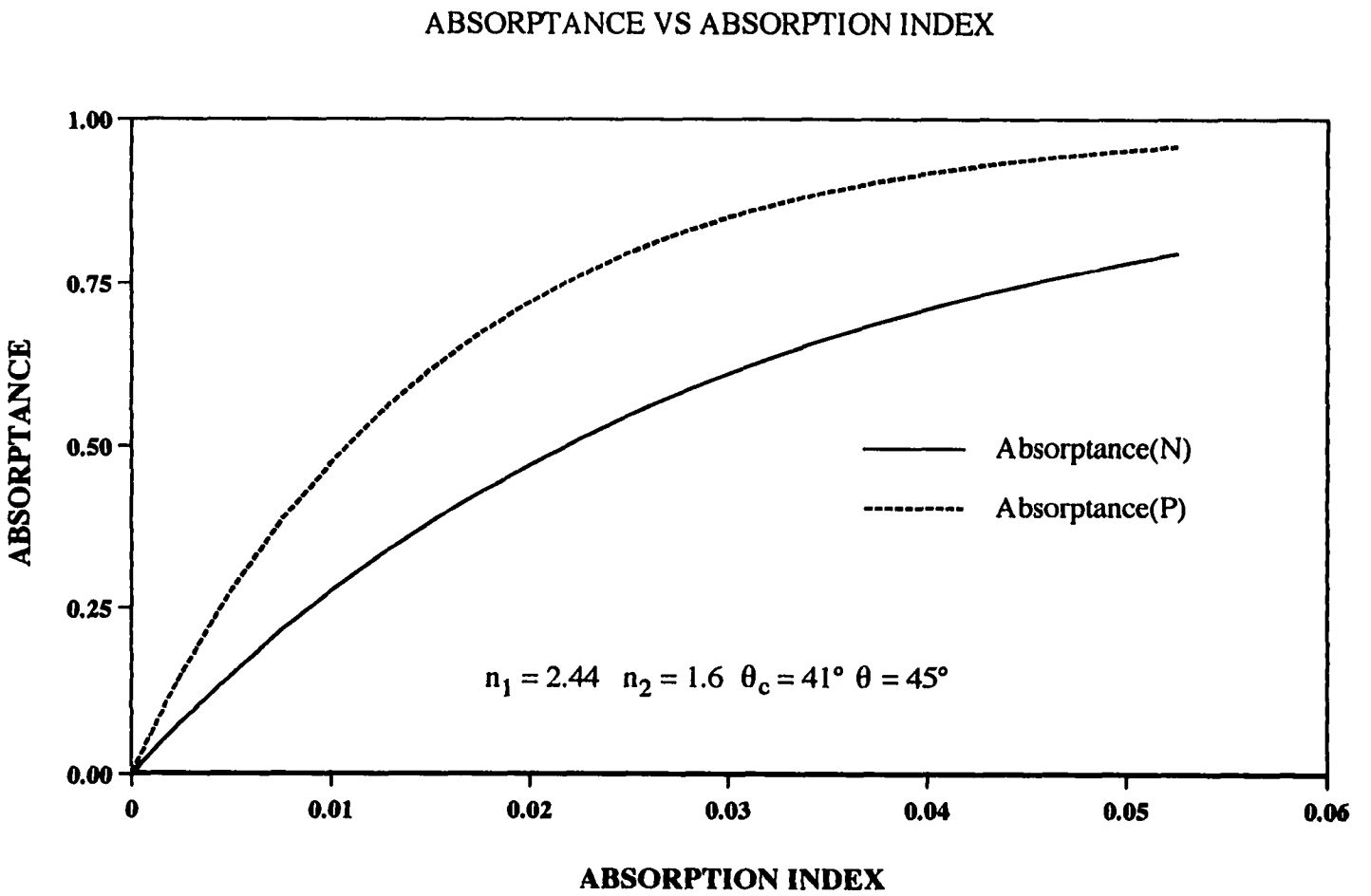

Figure 35. Perpendicular and parallel absorptance versus absorption index.

35. If the concentration (c) of the sample is known the absorption coefficient (α) may be determined or vise versa if the absorption coefficient (α) is known the concentration (c) may be determined.

The transmittance spectra shown in Figure 30, of aluminum hydroxide and natural corrosion collected using the zinc selenide ATR element were converted to absorptance spectra (1-Transmittance) in Figures 36 and 37. The calculated absorptance versus absorption index data in Figure 35 was then used to match the measured absorptance data to obtain the absorption index data shown in Figures 38 and 39. The absorption index data shown in Figure 38 and 39 are independent of all instrumental effects and may be used to analyze spectral data of aluminum hydroxide or natural corrosion collected from any spectrometer. Knowing the absorption index and from the equation (57) the absorption coefficient allows spectral data to be analyzed to determine the sample concentration; for example see equation (76).

6.6 LINEARITY OF ABSORPTANCE

For both qualitative and quantitative analyses of absorptance the dependence of absorptance on the length of fiber covered by the sample is to be determined. Several experiments were performed using aluminum hydroxide since it may be obtained in pure form. A few measurements were made using natural corrosion for comparison.

A paste of aluminum hydroxide and acetone was placed on a segment of the fiber core of known length. Once the paste had dried and a spectrum collected, paste was placed on an additional increment of fiber length and spectral data was collected again. A single background spectrum was collected at the beginning of each data set. Figure 40 shows transmittance data including 8 spectra of aluminum hydroxide covering a total of 80 cm of fiber in increments of 10 cm. The spectra have been displaced for clarity. Absorptance for

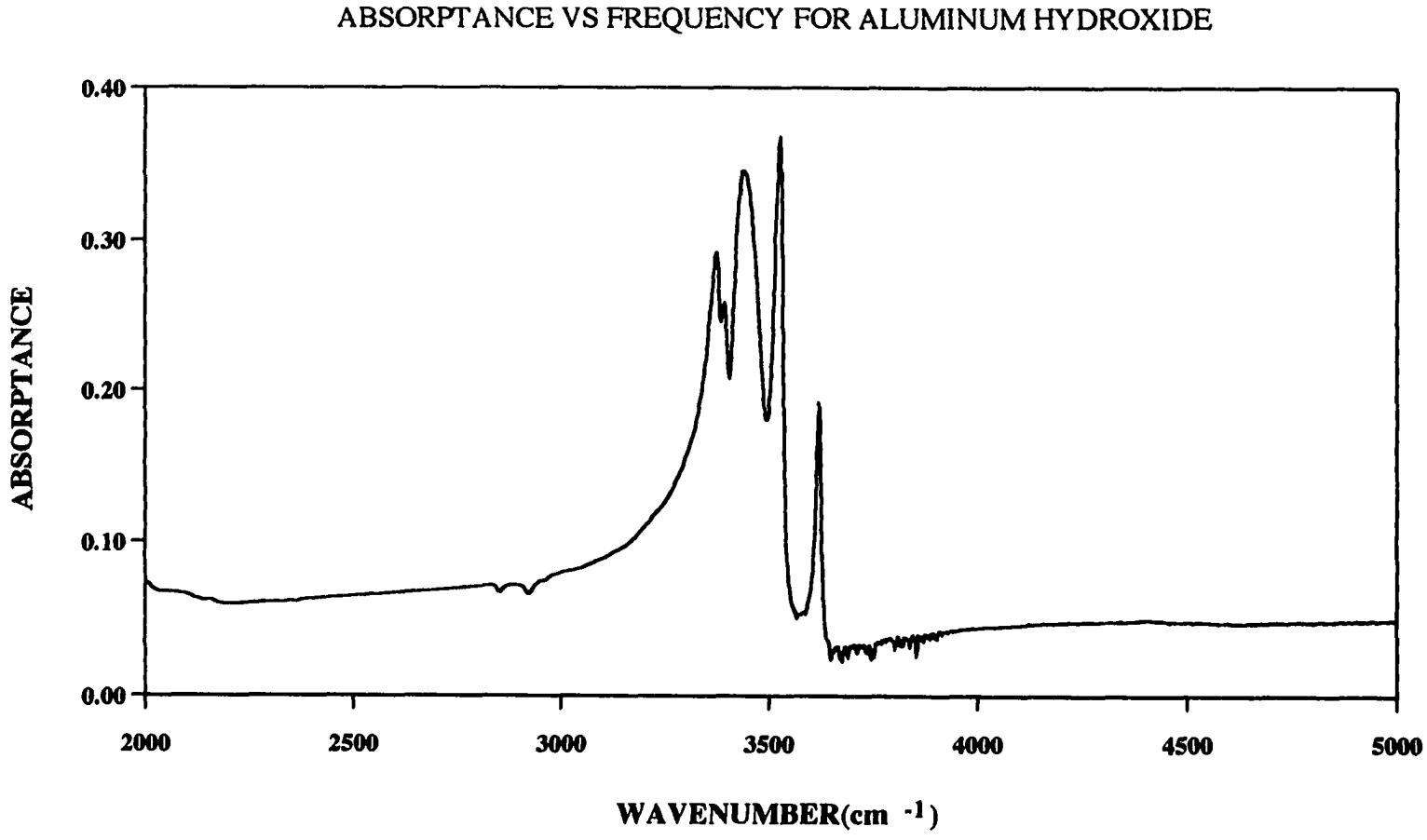

Figure 36. Absorptance versus frequency for a powdered aluminum hydroxide. The spectrum was collected using zinc selenide crystal as an ATR element.

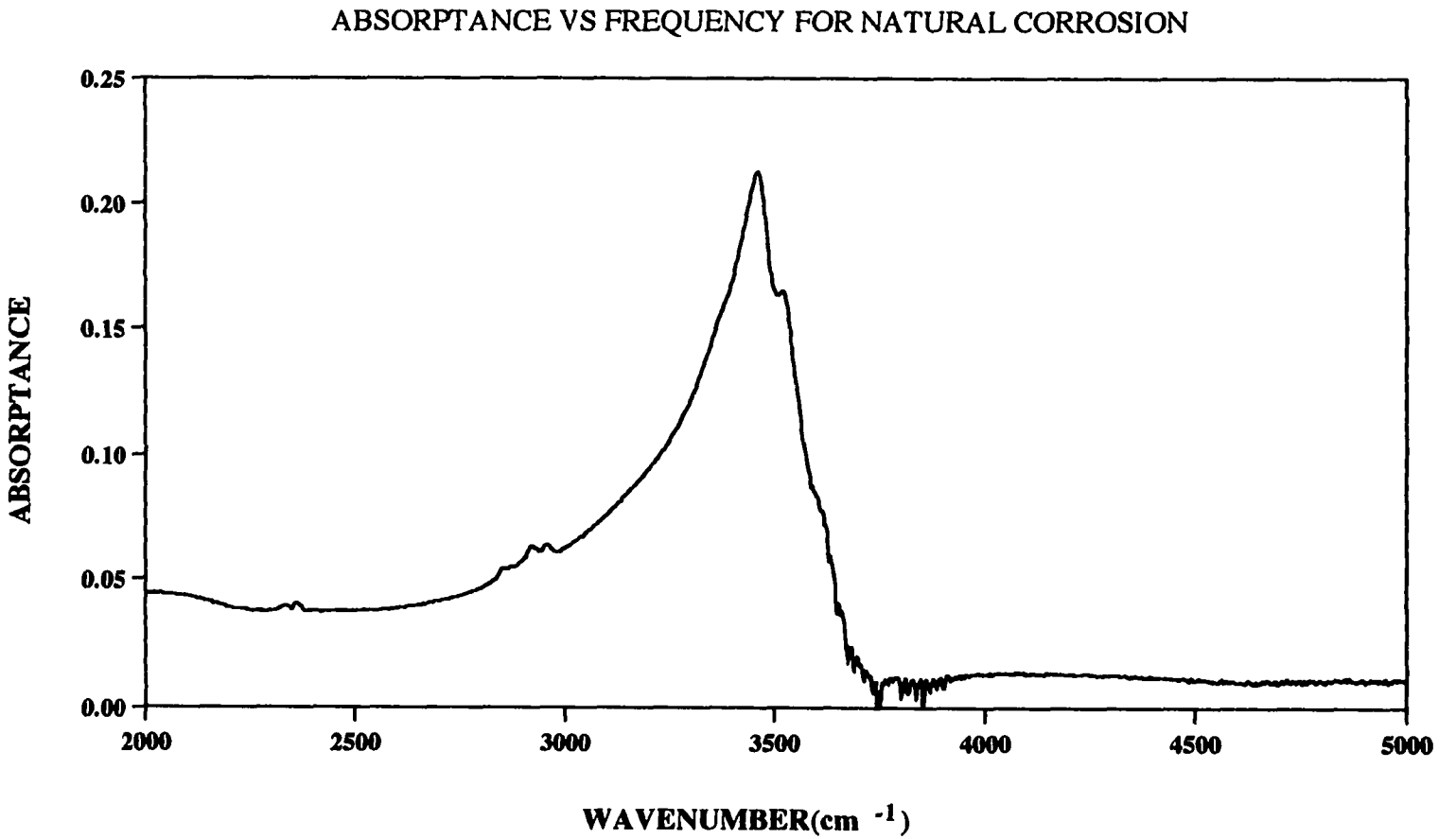

Figure 37. Absorptance versus frequency for a powdered sample of natural corrosion. The spectrum was collected using zinc selenide crystal as an ATR element

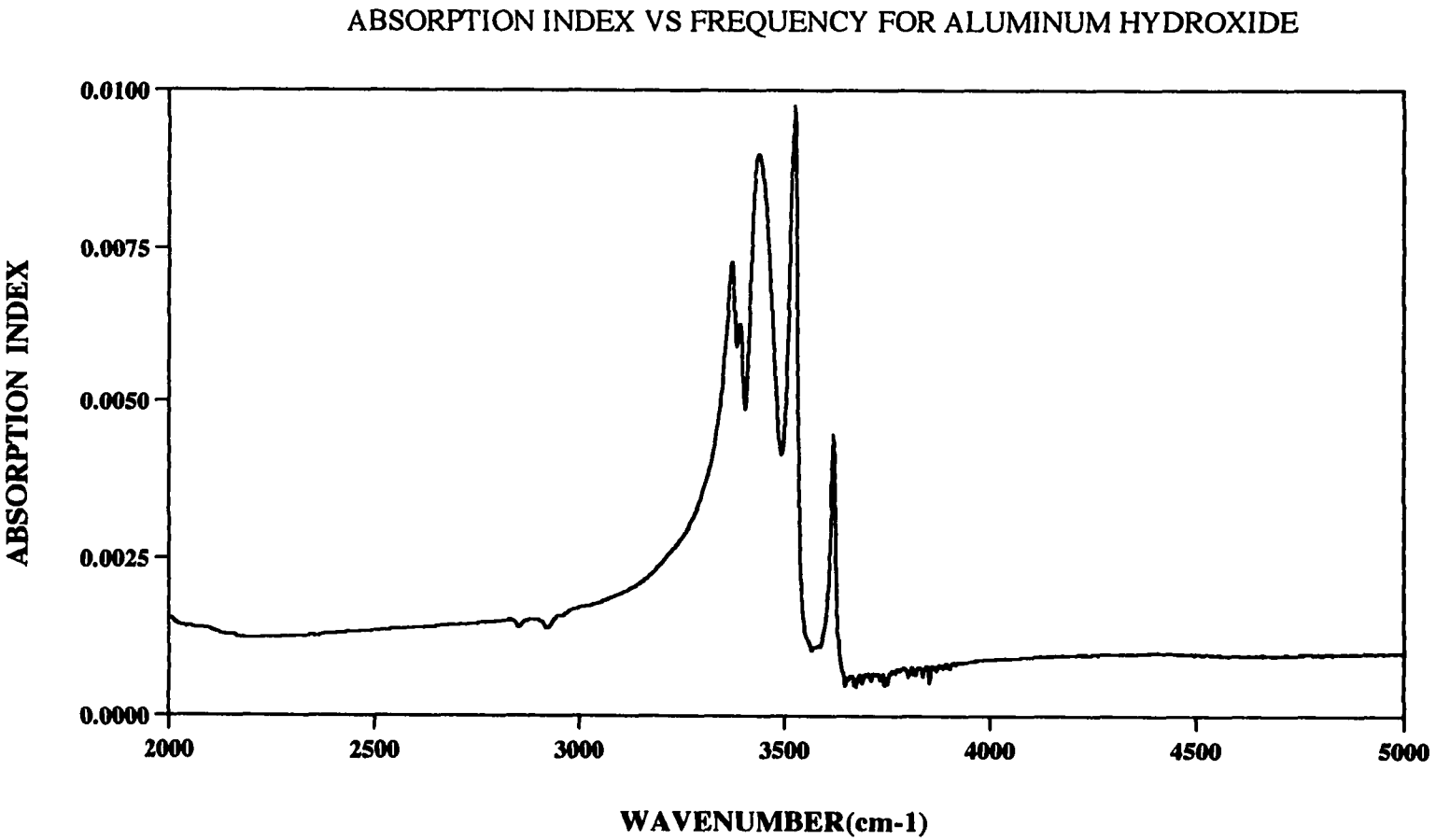

Figure 38. Absorption index versus frequency for a powdered sample ofaluminum hydroxide. The spectrum was collected using zinc selenide crystal as an ATR element.

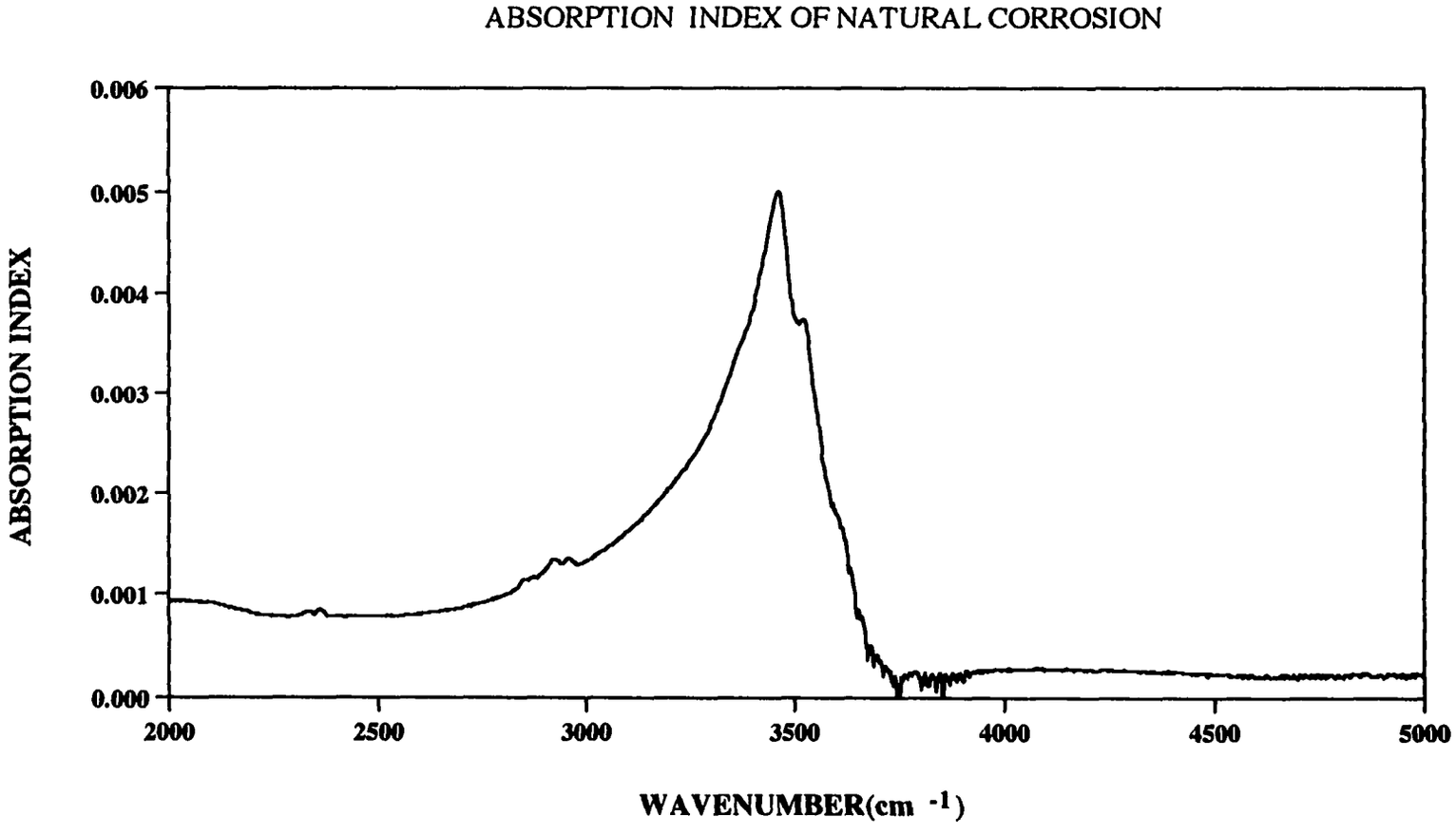

Figure 39. Absorption index versus frequency for a powdered sample of natural corrosion. The spectrum was collected using zinc selenide crystal as an ATR element.

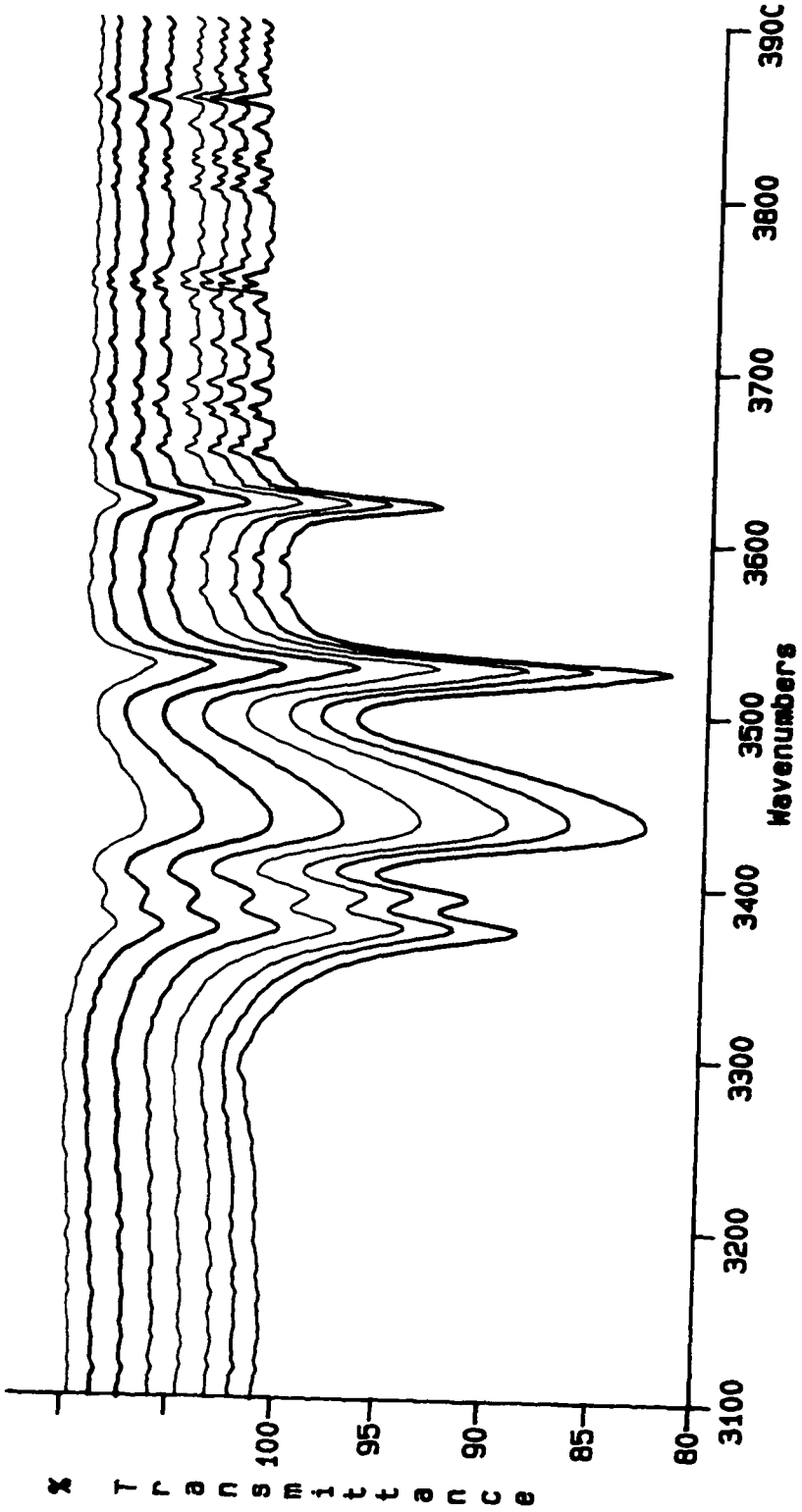

Figure 40. Transmittance spectra of aluminum hydroxide covering 80 cm of fiber with 10 cm increments.

each spectrum measured at the strong peak at 3440 cm^{-1} is shown in Figure 41. The dependence is almost linear with a very small second order component when a three parameter polynomial is fit to the data. There is a small systematic shift of approximately 0.006 absorptance units as a positive intercept.

The measurements were repeated under similar experimental conditions to check the accuracy. A new length of fiber was used because the fibers can not be easily cleaned to remove previous sample material. This requires selecting a new length of fiber, polishing the fiber ends, mounting the fiber into the optical path of the spectrometer, and adjusting the x,y,z translation stages to bring the fiber end properly to the focus of the zinc selenide lens. The criterion for proper alignment was to obtain the maximum signal at the zero path difference point of the interferogram. The new fiber is decoated and a new background spectrum is collected. The fiber interferometer spectrometer system is then ready for the sample to be placed on the fiber.

Spectral data of aluminum hydroxide covering 150 cm of fiber core in increments of 20 cm is shown in Figure 42. The absorptance for each spectrum, again measured at 3440 cm^{-1} is displayed in Figure 43. Again the absorptance versus length of fiber covered by the sample is linear, with a small positive intercept of about 0.008 absorptance units. The variation from linearity and non-zero intercept of the data points is mostly a result of the uncertainty in placing the aluminum hydroxide paste on the fiber core over precisely the length desired.

The absorptance data from the two separate experiments can be compared using the results shown in Figures 41 and 43. At any given length of fiber covered by the aluminum hydroxide sample the absorptance in Figure 41 is more than twice the absorptance in Figure 43. The spectral measurements were repeated two additional times using a new fiber each time. The spectral data are shown in Figures 44 and 45, while the corresponding

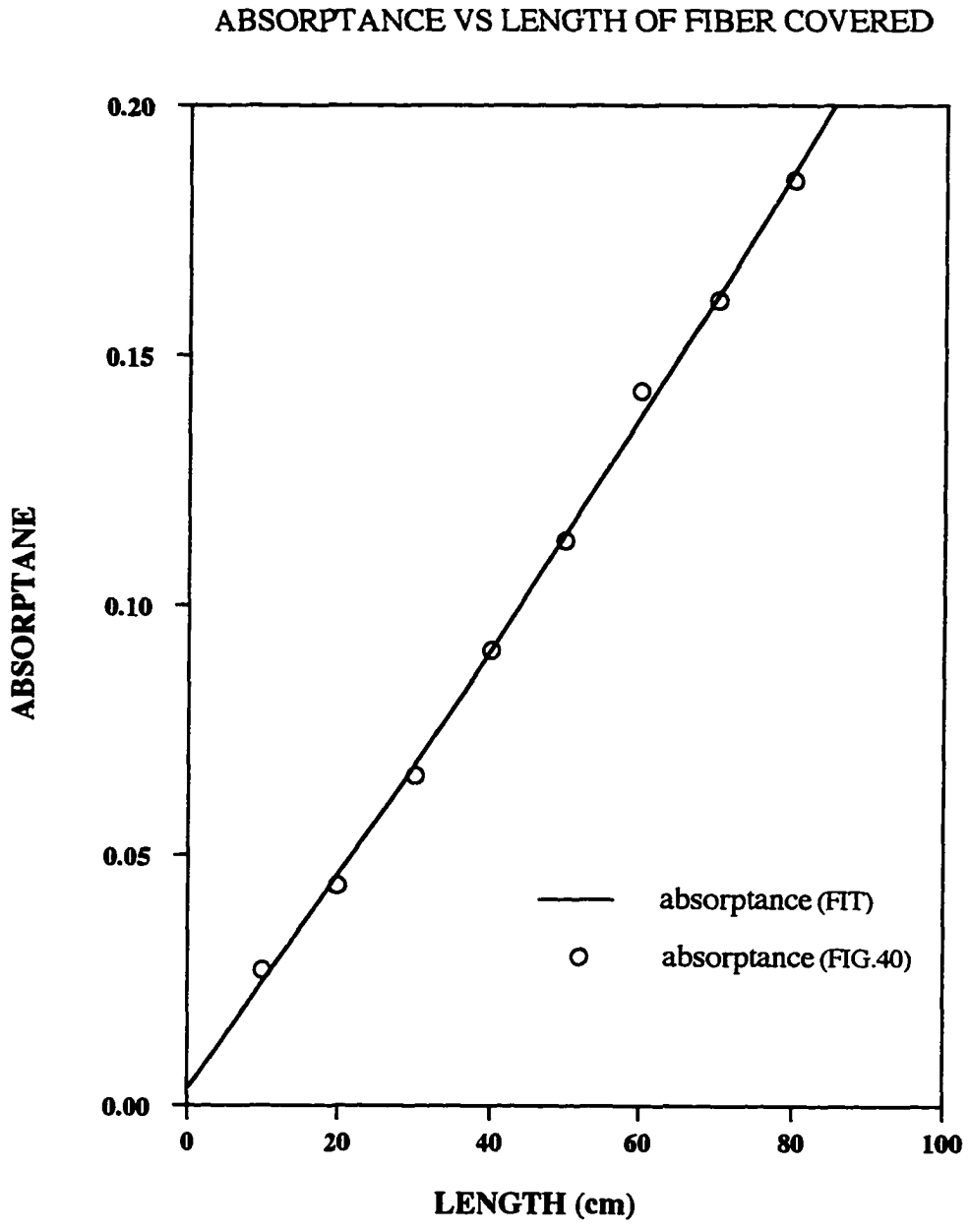

Figure 41. Absorptance at 3440cm^{-1} vs length of fiber covered by aluminum hydroxide.

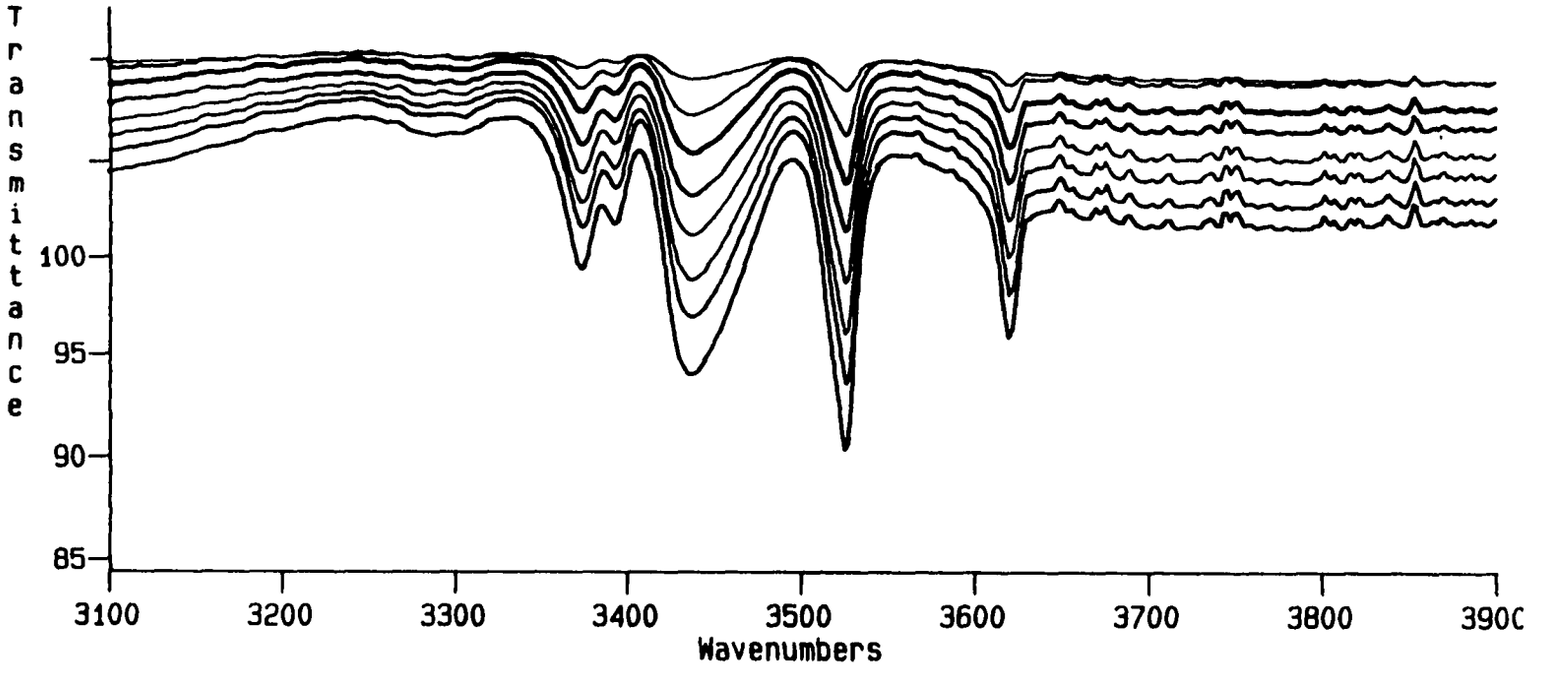

Figure 42. Transmittance spectra of aluminum hydroxide covering 150 cm of fiber with 20 cm increments

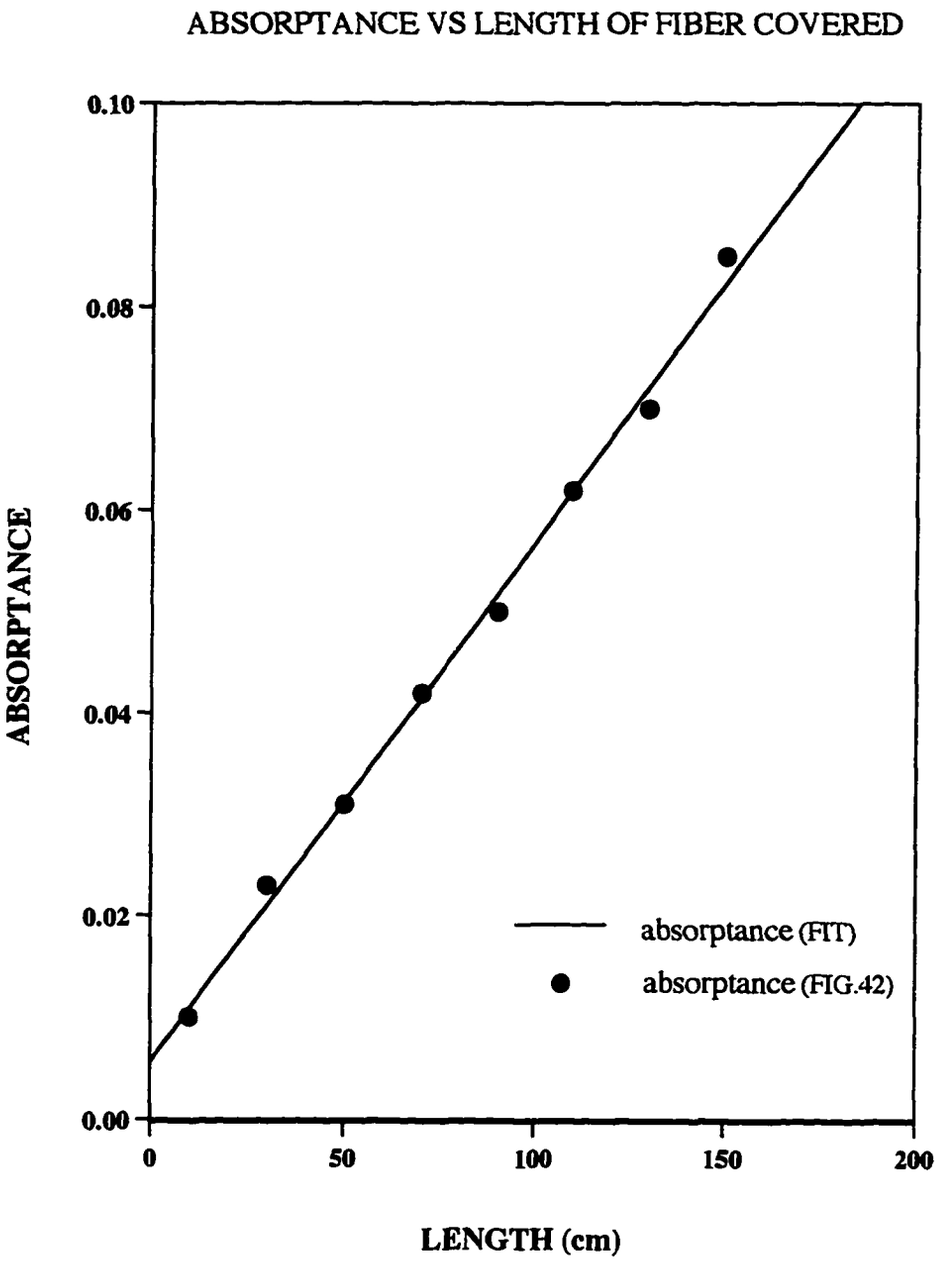

Figure 43. Absorptance at 3440cm^{-1} vs length of fiber covered by aluminum hydroxide.

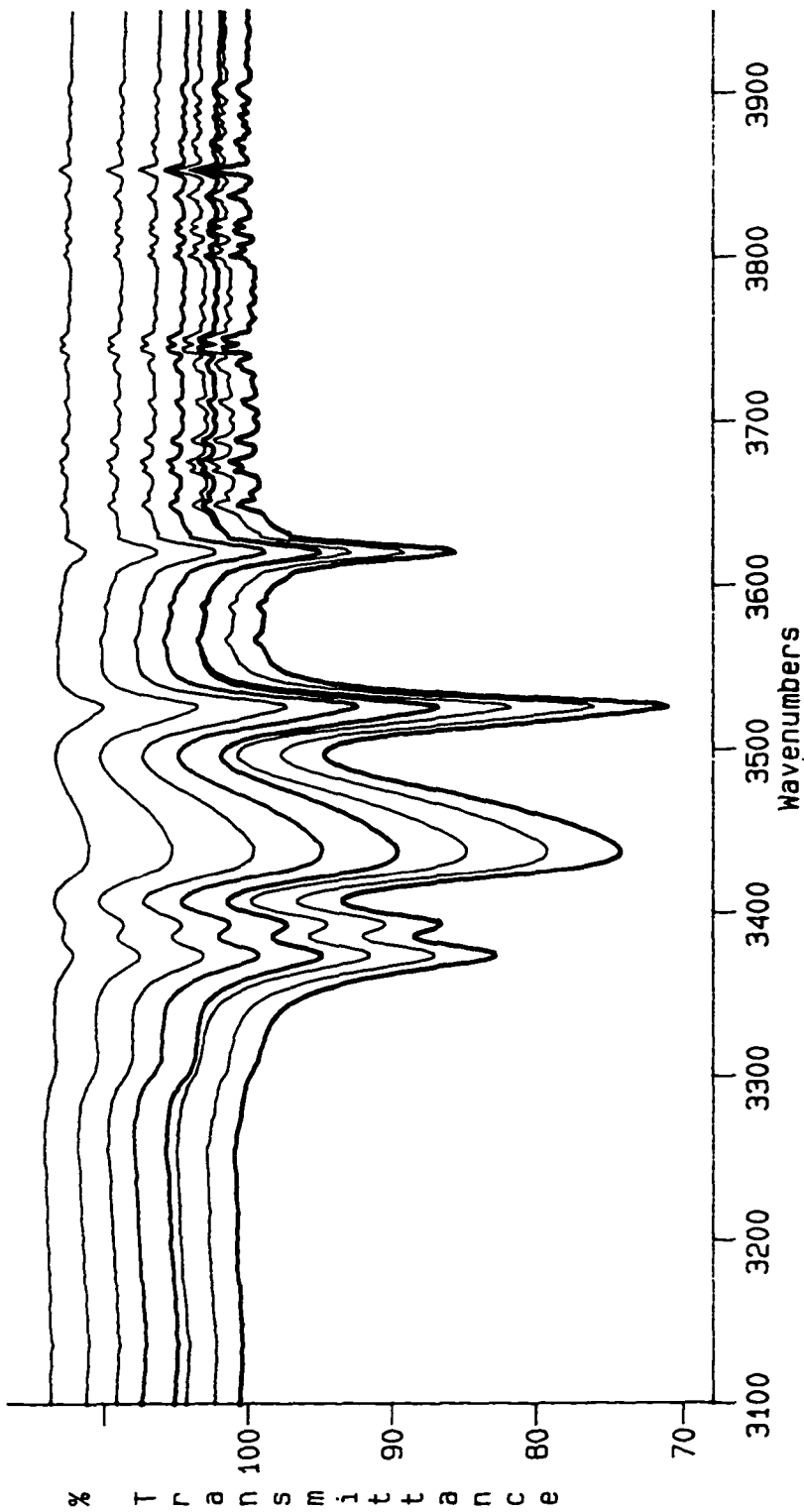

Figure 44. Transmittance spectra of aluminum hydroxide covering 200 cm of fiber with 25 cm increments.

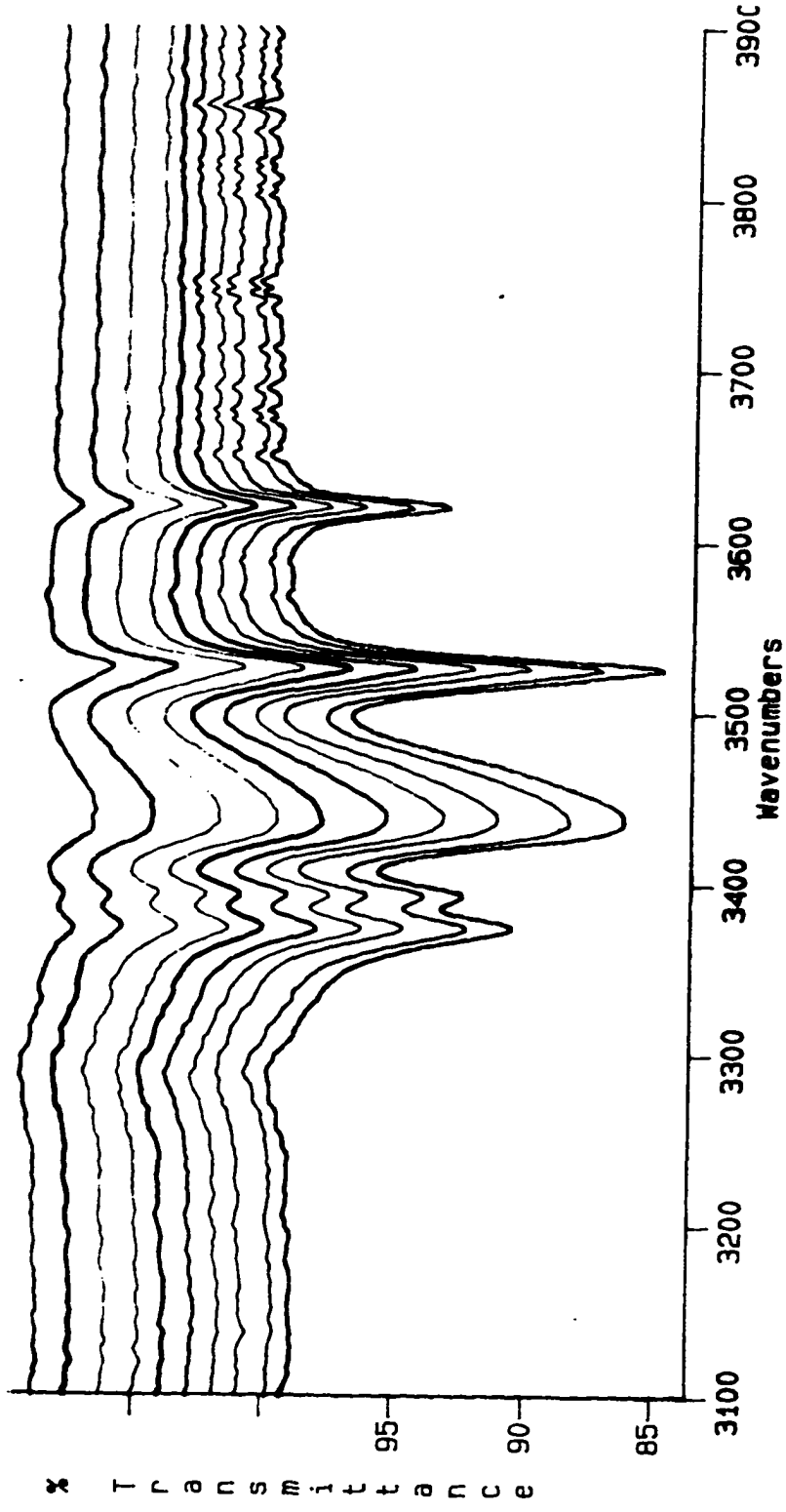

Figure 45. Transmittance spectra of aluminum hydroxide covering 120 cm of fiber with 20 cm increments.

absorptance data are shown in Figures 46 and 47. The absorptance data obtained from these two sets of measurements have non-linear behavior, but the magnitude of the absorptance data shown in Figures 46 and 47 agrees reasonably well.

For comparison, all of the experimental data discussed above is displayed together in Figure 48. It is clear that for any given value of fiber length covered by the sample there is a wide range of measured absorptance. This difference is not due to preparation of the sample paste of aluminum hydroxide and acetone placed on the fiber core. If the sample preparation were the origin of the problem then the linear dependence in Figures 41 and 43 would not have been obtained.

The origin of the variation in the measured absorptance values must result from the way that radiation is launched into the optical fiber. This could be due to several factors. The fiber end may not have been polished perfectly perpendicular to the optical axis. Consequently, radiation is incident on the polished fiber end at slightly different angles each time a different fiber is used. Also, the position of the fiber end relative to the focus of the f/1 lens is very sensitive. Small displacement of the fiber end in a direction perpendicular to the fiber optical axis, in the focal plane of the lens, reduces the interferometric signal recorded at the zero path difference point of the interferogram. The f/1 focusing lens does not fill the acceptance cone of the fiber completely. This suggests that each time a new fiber is used to make measurements, the radiation focused onto the end of the fiber fills a different portion of the fiber acceptance cone. The cone of propagating radiation inside the fiber core is consequently not symmetric and not centered with respect to the optical axis of the fiber core. This will affect the distribution of incident radiation on the core-sample interface. The result will be a variation in the penetration depth of the evanescent field, and effective thickness for each fiber. Consequently the absorptance values will be affected by this variation.

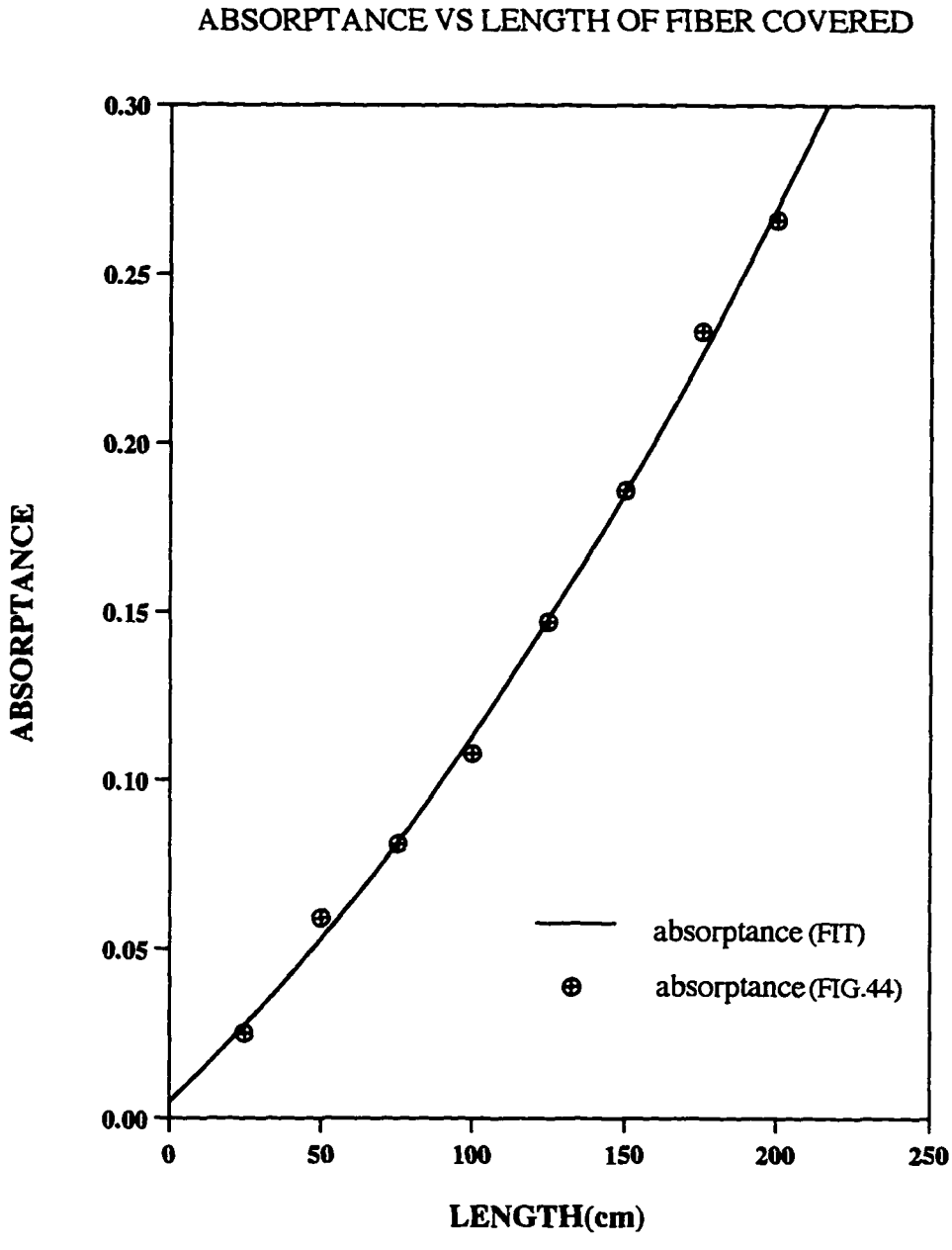

Figure 46. Absorptance at 3440cm^{-1} versus length of fiber covered by aluminum hydroxide.

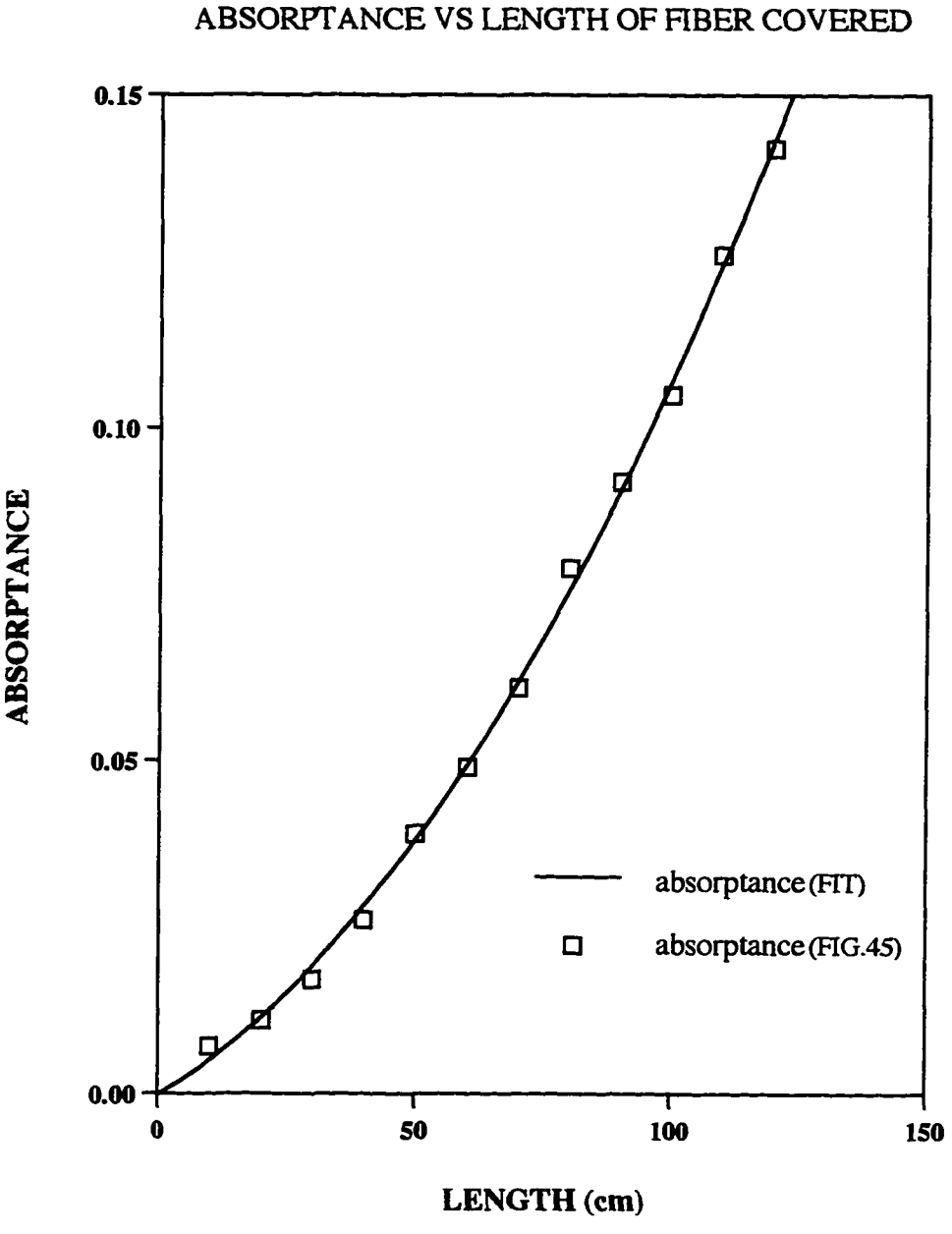

Figure 47. Absorptance at 3440 cm^{-1} versus length of fiber covered by aluminum hydroxide.

Spectral data collected using the zinc selenide crystal as the ATR optical element does not show this variation in absorptance since the crystal is rigidly mounted in the well defined optical path. Spectral data collected from this reference technique was used to infer an absorption index which was then used to predict the absorptance measured using an optical fiber.

The absorption index κ shown in Figure 38 was used with the general expression for R, from equations 28 and 34, to calculate the absorptance $A_p(\theta,b) = (1-R^b)$ at a particular angle of incidence θ for which radiation bounces within the fiber b times. The absorptance was calculated using the value of absorption index of 0.0093 at 3440 cm^{-1}. The absorptance values $A_p(\theta,b)$ were numerically integrated over θ weighted by the increment of area through which the radiation at θ passes. A check on the numerical integration was made by comparing the numerical answers with the approximate analytical result from equation (72), where that approximation is valid. For this calculation to be valid, the sample must cover the same fraction of zinc selenide crystal and optical fiber sample surface area.

This calculated result is also shown in Figure 48. The magnitudes of all of the experimental values using the optical fiber probes are below the calculated (theoretical) absorptance values. The experimental measurements of absorptance obtained using the optical fibers give approximately the proper dependence on length of fiber covered by the sample, but not the proper magnitude of absorptance.

Samples of natural corrosion were also used to make measurements of absorptance versus length of fiber covered by the sample. The procedure was the same as above for aluminum hydroxide. The spectral data are shown in Figures 49 and 50 for samples covering up to 150 cm of fiber in increments of 25 cm. The absorptance data measured at 3440 cm^{-1} is shown in Figure 51, and the absorbance data is shown in Figure 52.

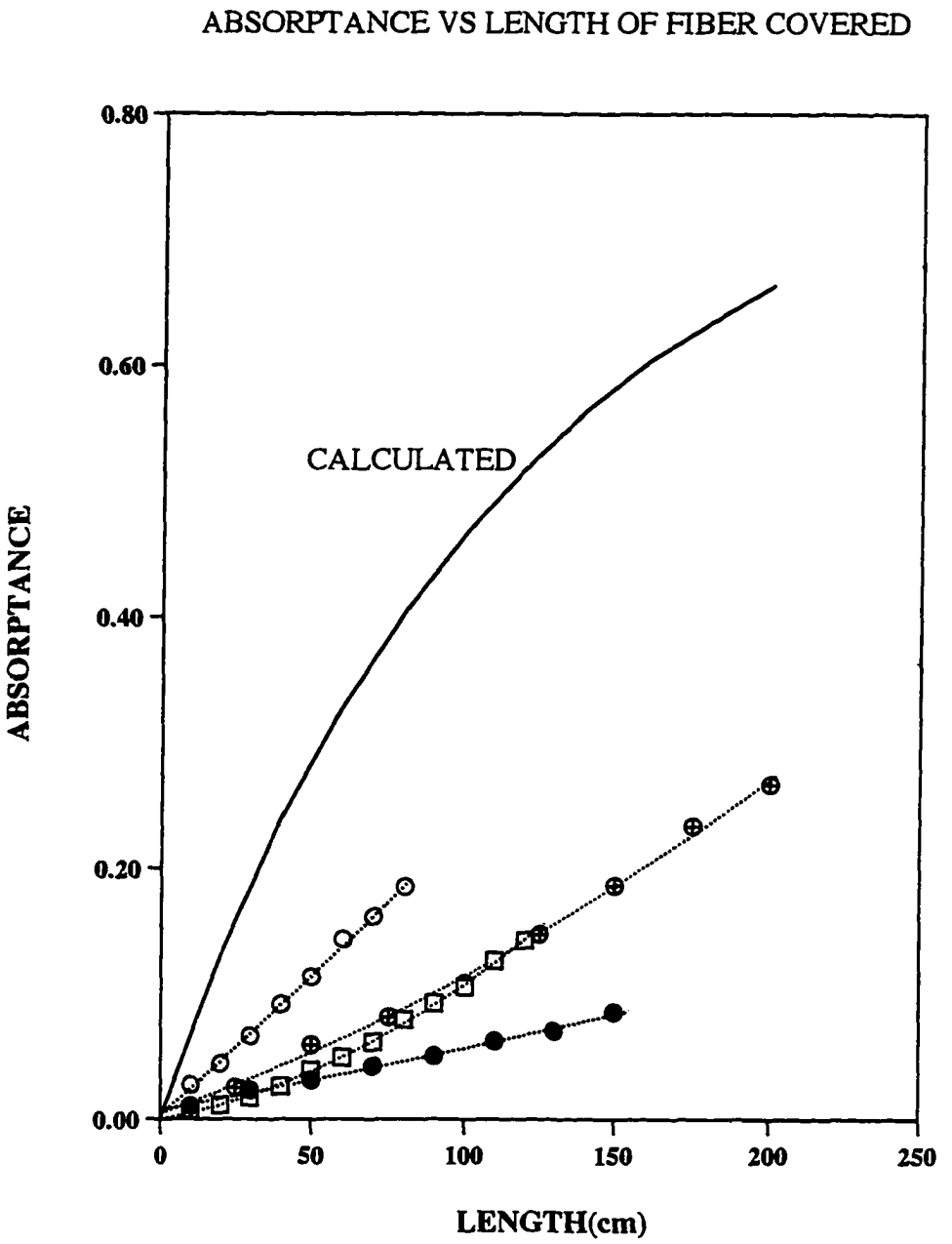

Figure 48. Absorptance at 3440cm^{-1} versus length of fiber covered by aluminum hydroxide (from Figures 41, 43, 46, 47).

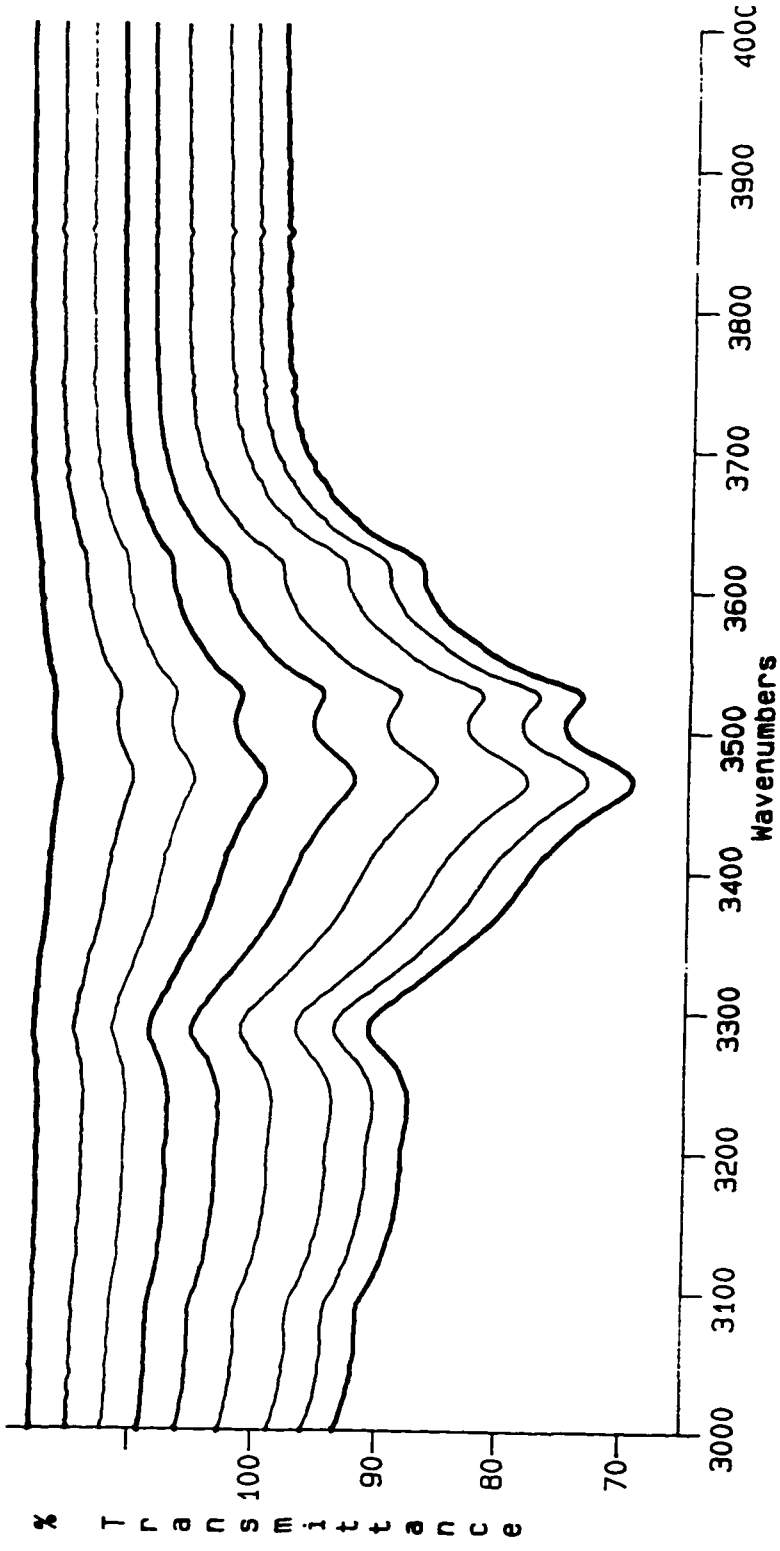

Figure 49. Transmittance spectra of natural corrosion covering 150 cm of fiber in increments of 25 cm.

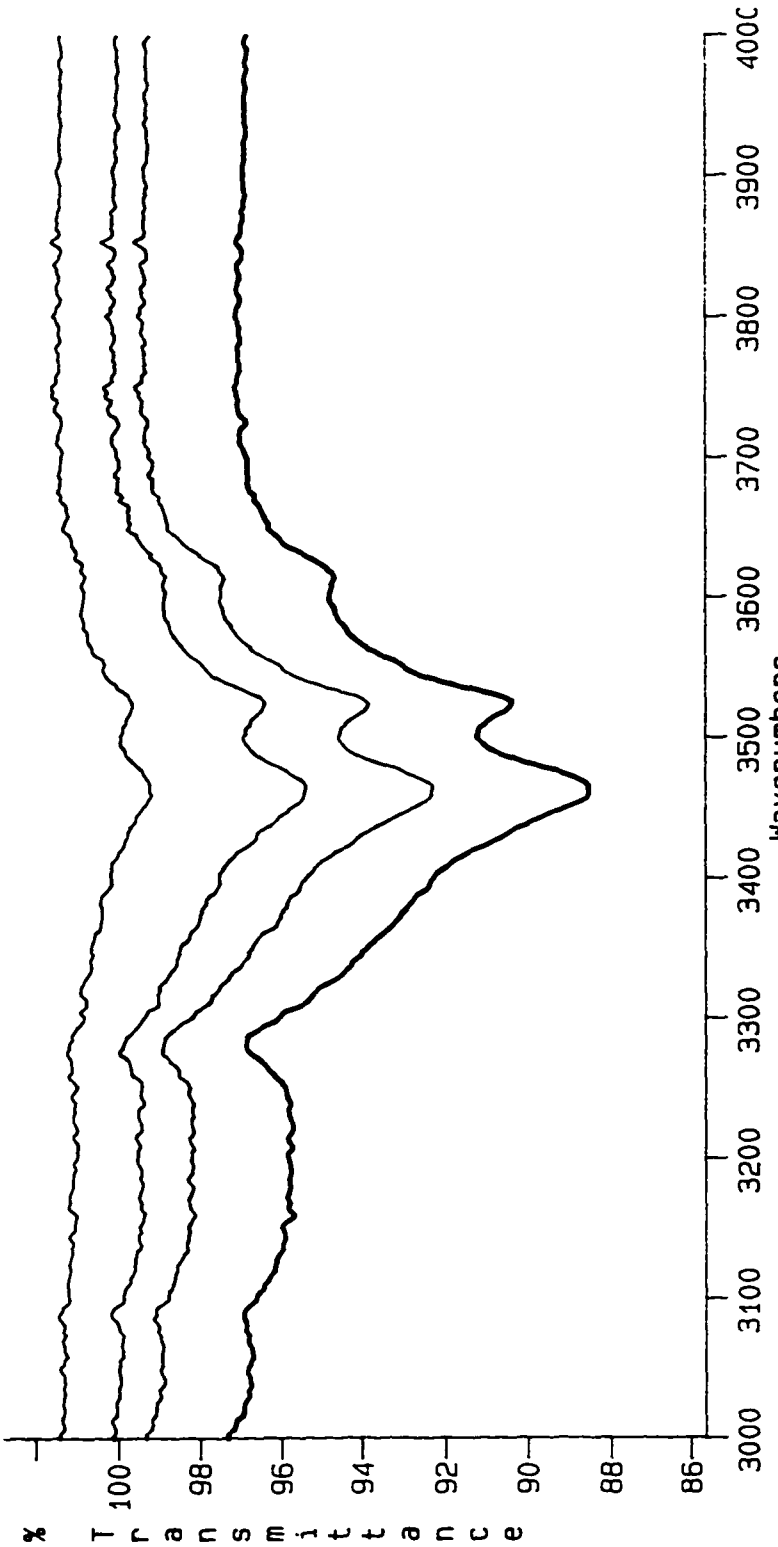

Figure 50. Transmittance spectra of natural corrosion covering 100 cm of fiber in increments of 25 cm.

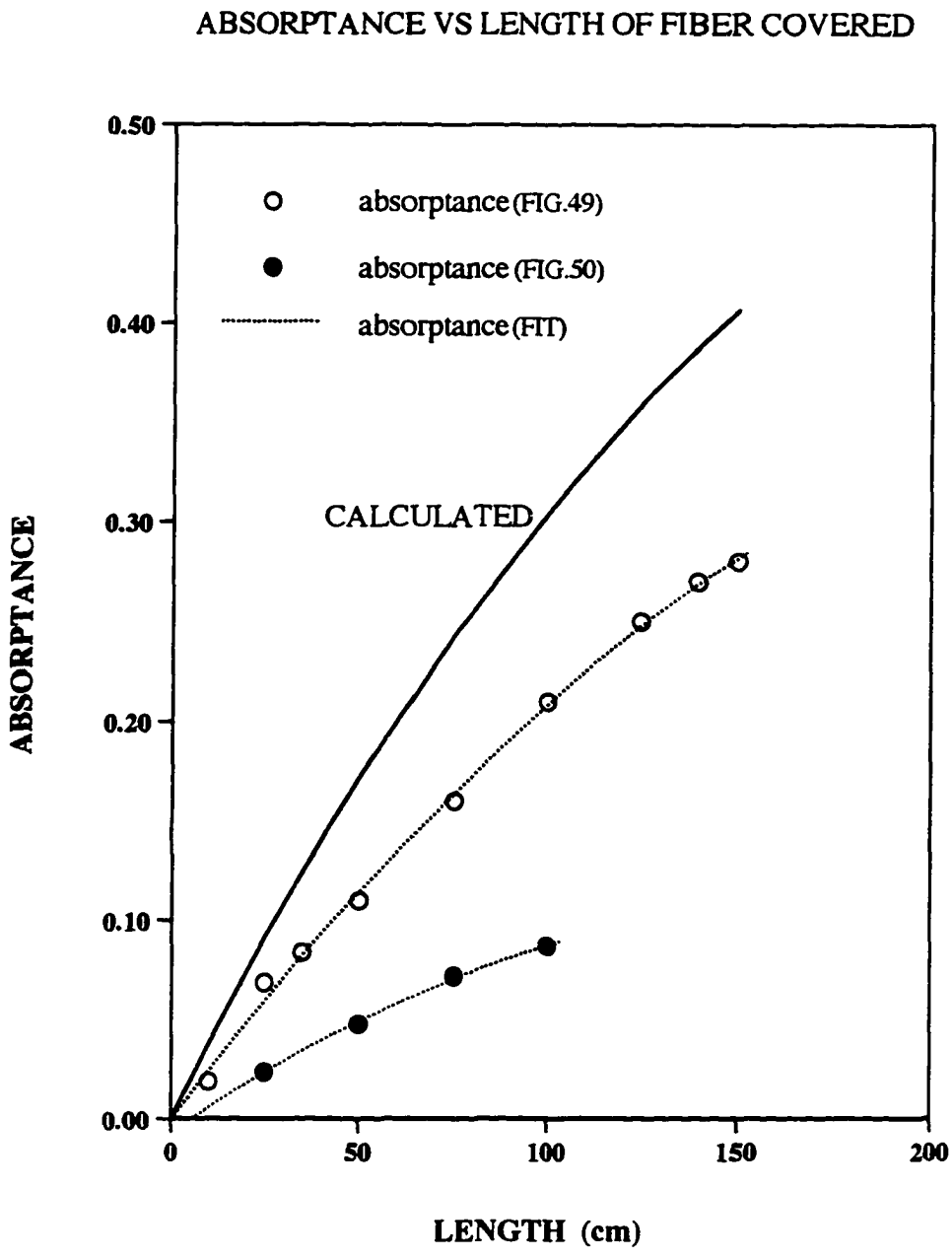

Figure 51. Absorptance at 3440 cm^{-1} vs length of fiber covered by natural corrosion

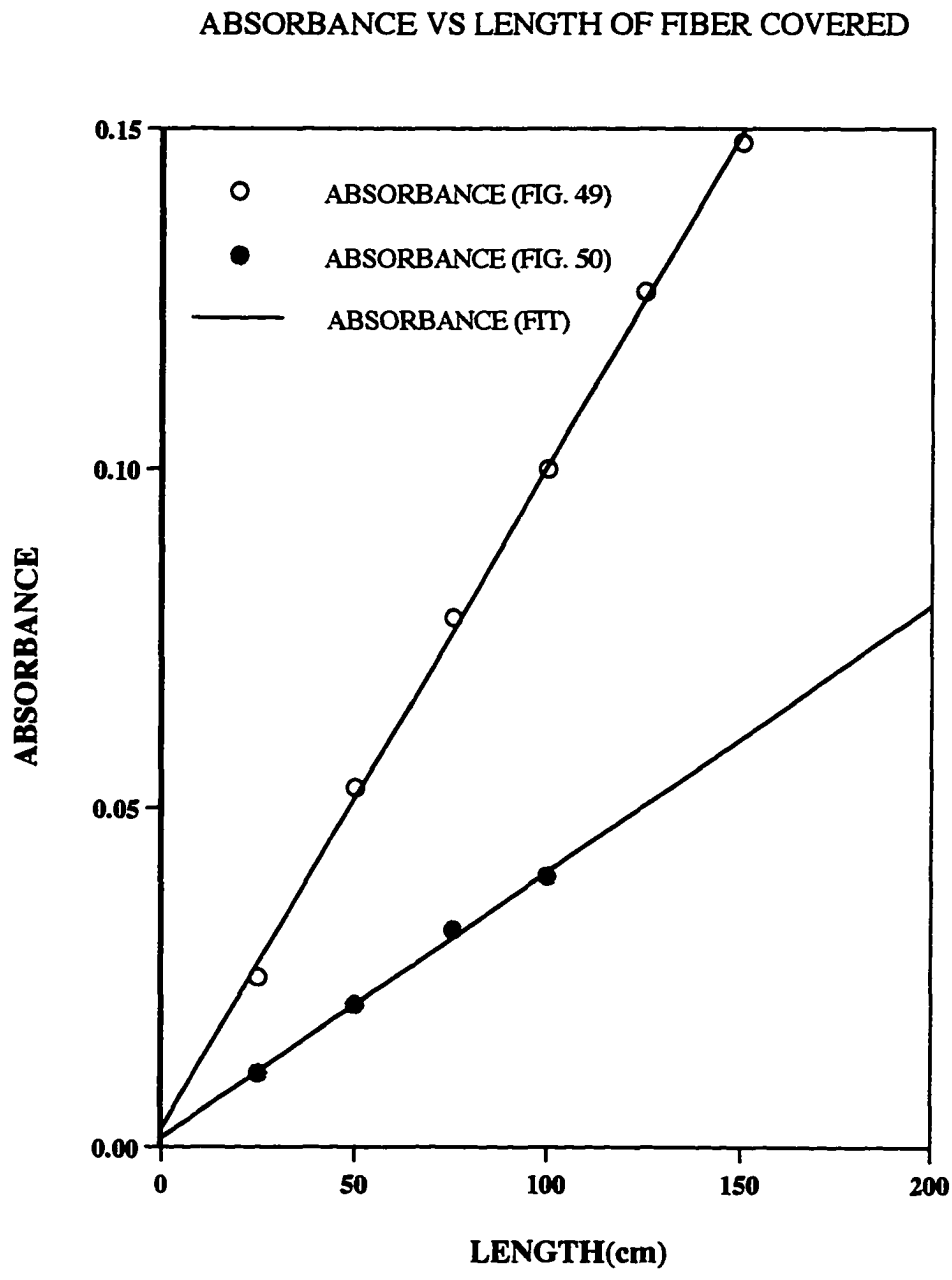

Figure 52. Absorbance at 3440cm^{-1} vs length of fiber covered by natural corrosion sample

The spectral data, Figure 49, has a flat background above 3900 cm^{-1}(100% line) against which to measure the absorptance values. The signal to noise ratio is high, greater than 400 to 1, so that the absorptance can be measured with high precision. The source of measurement errors will be systematic errors that results from instrumental changes that occur during the data collection.

Both sets of absorptance data display non-linear dependence on length of fiber covered by the sample. Absorbance determined for two data sets is linear with approximately zero intercept in both cases (see Figure 52). The slope of the absorptance differs when the two data sets are compared. To estimate what the magnitude of the absorptance should be, the absorption index displayed in Figure 39 was used with the general theory for R, as in the case of aluminum hydroxide. In this case, from Figure 39, a magnitude of 0.005 at 3440 cm^{-1} was used in the calculation. The result is the solid curve marked calculated in the Figure 51.

Experimental effects which can change the measured absorptance by changing the angle of incidence of the internally reflected propagating radiation are estimated to be small. This includes the effect of fiber bending and the effect of diffuse reflection of the propagating radiation. Fiber bending has been estimated to have almost no effect until the bending radius is less than about 4 cm. For that reason the bend radius was kept larger than 10 cm. Also, diffuse reflection of the internally reflected radiation does not occur for radiation of the wavelength being studied, approximately three micrometers. The fiber surface is smooth on a scale much smaller than this wavelength. This may be seen in Figure 53 which is a scanning electron micrograph of a chalcogenide fiber segment with sample of aluminum hydroxide adhered to the surface of the fiber. The magnification scale is at the bottom of the figure for comparison. The right side of this figure is an enlargement of the small rectangular area on the left side. The smallest aluminum hydroxide particles

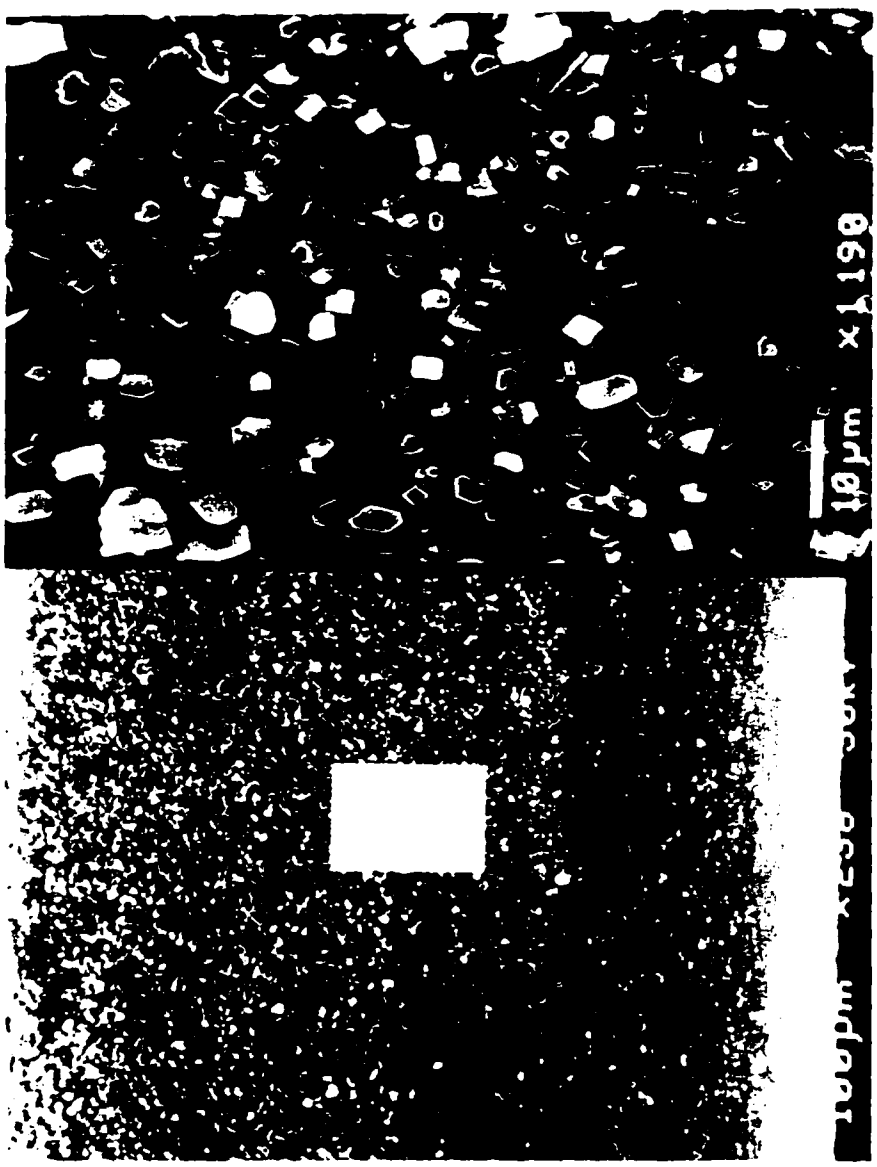

Figure 53. Scanning electron micrograph of optical fiber with aluminum hydroxide adhered to surface.

which can be seen on the right side are less than one micrometer across. No imperfections of the fiber surface can be seen on the micrometer scale. Therefore diffuse scattering on the micrometer scale can be ruled out.

The absorptance deduced from fiber measurements is lower than expected. The measured dependence of the absorptance as a function of fiber length covered by the sample is correct. Based on the theoretical curve in Figures 48 and 51, using a properly aligned instrument for radiation to fill the acceptance cone uniformly and properly polished end of optical fiber should be possible not only detect natural corrosion but also predict quantities of aluminum hydroxide.

CHAPTER 7

SUMMARY AND CONCLUSION

An experimental technique for remote detection of aluminum corrosion has been investigated. The technique combines long chalcogenide optical fibers and a Michelson interferometer spectrometer to make FTIR evanescent wave absorption measurements of aluminum corrosion. The corrosion samples were collected from discarded aircraft components which had been corroded in the natural environment. For comparison, absorption data of pure powdered aluminum hydroxide was also collected.

To evaluate the technique using optical fibers as remote probes, data of the same samples were collected by conventional evanescent wave absorption spectroscopy using a zinc selenide crystal as the ATR optical element. Since the conventional technique using crystal has relatively simple geometry and well defined optical path, it was used as a reference technique. The optical fiber technique has the advantage that long fibers can guide radiation far from the spectrometer and the same fiber can be used as the sensing element.

Spectral resolution and measurement sensitivity were investigated. It was found that the 8 cm^{-1} and 16 cm^{-1} resolution were adequate to faithfully record the spectral features of aluminum hydroxide and aluminum corrosion product, respectively. It was also found that an instrumental signal to noise ratio of about 400 to 1 is sufficient to detect a corrosion sample on 1 to 3 mm^2 of a 500 μm chalcogenide optical fiber.

Aluminum hydroxide is a principal corrosion product of aluminum. Therefore spectra of pure aluminum hydroxide were compared with those of naturally occurring corrosion. Five spectral absorption features at 3374, 3394, 3440, 3525, and 3620 cm^{-1} are identified in aluminum hydroxide. The spectral features of corrosion samples located at the

same frequencies as aluminum hydroxide. The spectral peaks of corrosion samples are broader but have approximately the same integrated area indicating more frequent collision of the O-H bonds with surrounding molecules.

Since water is important to the corrosion process in the natural environment, spectra of water and aluminum hydroxide together were collected. It was found that the presence of water changes the environmental conditions such that the aluminum hydroxide does not absorb evanescent wave radiation. The presence of water lowers the penetration depth and may hold the aluminum hydroxide in suspension away from the sensing fiber. The minimum penetration depth at grazing incidence angle is about 0.2 micrometer at a wavelength of 3 micrometers as confirmed by numerical calculations.

Absorption spectra of liquid water alone were collected using an optical fiber. This data was collected because a liquid sample is expected to cover the fiber uniformly and completely. In spite of carefully controlled conditions, a systematic shift in the absorptance was found when two data sets were compared. This suggested that the launching condition of radiation into the fiber were not consistent.

Absorption spectra of three samples of natural corrosion from different aluminum alloy were collected and compared. Three samples were collected on separate occasions from components of different aircraft which indicates the corrosion environments were different. The spectra of the three samples were collected using a zinc selenide crystal as an ATR element with the same surface area for each sample. The positions of the spectral peaks and the half widths at the half maximum were found to be the same. This indicates that the same corrosion product was produced. The magnitude of the transmittance in the three spectra were different. It could be due to other materials collected along with the corrosion samples scraped from the aircraft components. These materials are present on the fiber surface along with the corrosion sample. The results indicate that detection of

corrosion is possible. Quantitative analyses of corrosion would be possible by comparing spectra of a known amount of pure sample.

The reference technique with a zinc selenide crystal ATR optical element was used to collect spectral data of aluminum hydroxide and corrosion sample. An absorption index was determined by comparing the absorptance data from the spectra with theoretical calculations. This absorption index was then used to predict absorptance of the same samples studied using an optical fiber .

Absorptance was measured as a function of the the length of fiber covered by the sample for both aluminum hydroxide and corrosion sample. An approximate linear dependence with zero intercept was found. An absorption index was obtained from spectral measurements using the reference technique and theoretical calculations. These theoretical absorptance values were larger than all of the measured values, which suggested that the theoretical absorptance values are an upper limit on the experimental measurement.

This difference was due to the launching conditions of the radiation into the zinc selenide ATR crystal element and optical fiber. Launching radiation into the zinc selenide crystal at the proper angle with its large cross section has maximum throughput, penetration depth, and effective thickness. However the optical fiber cross section is much smaller and more sensitive to alignment than the crystal and the acceptance cone changes each time a new fiber is used. This changes the penetration depth and effective thickness which affects the quantitative results.

It is confirmed that optical fiber FTIR evanescent wave spectroscopy is a very sensitive technique for qualitative detection of small amount of natural aluminum corrosion. When the technique can be compared with the conventional reference technique using crystal ATR optical elements, quantitative measurement can be made as well.

REFERENCES

1. F. Moser, N. Barkay, A. Levite, E. Margalit, I. Paiss, A. Sa'ar, I. Schnitzer, A. Zur, and A. Katzir, " Research and Development on Silver Halide Fibers at TelAviv University", in Infrared Fiber Optics II", J.A. Harrington, and A. Katzir, Editors, SPIE Proceedings, Volume 1228, 128(1990).

2. A.R. Hilton Sr. "Chalcogenide Glass Optical Fibers", in Infrared Fiber Optics III, J.A. Harrington, A. Katzir, Editors, SPIE Proceedings, Volume 1591, 34(1991).

3. A.R. Hilton Sr. "As-Se-Te-Based Glass Fiber", in Infrared Fiber Optics II", J.A. Harrington, and A. Katzir, Editors, SPIE Proceedings, Volume 1228, 76(1990).

4. D. A. Krohn, *Fiber Optic Sensors*, Instrument Society of America, 1991

5. F.M. Mirabella, Jr., *Internal Reflection Spectroscopy*, Marcel Dekker, 1993.

6. N. J. Harrick, *Internal Reflection Spectroscopy*, Interscience publishers,1967

7. T. Katsuyama and H. Matsumura, *Infrared Optical Fibers*, Adam Hilger Imprint,1989

8. C. Croitoru, N. Shamir, D. Mendlovic, J. Dror, and Y. Lereah, " Glasses and Optical IR fibers of $As_2 Se_{3-x}Te_x$ ", Proceedings of Material Reseach Socierty Symposium, Vol.88, pp. 177-181, 1987.

9. I. Harruvi-Busnach, J. Dror, and N. Croitoru, " Infrared Optical Glasses and Fibers Based on the Chalcogenide Glasses System Ge-Sn-Se-Te ", SPIE Vol. 1228, pp. 85-91,1990.

10. Amorphous Materials Inc., 3130 Benton St. Garland, TX 75042.

11. A. R Hilton, Sr. " Chalcogenide Glass Optical Fibers ", SPIE Vol. 1591, pp. 34-42, 1991.

12. A.R. Hilton, Sr., " As-Se-Te -based Glass Fibers ", SPIE Vol. 1228, pp. 76-84, 1990.

13. M.D. DeGrandpre and L.W. Burgess, " Long Path Fiber-Optic Sensor for Evanescent Field Absorbance Measurements", Anal. Chem. 60, 2582 (1988).

14. F.M. Mirabella, Jr., and N.J. Harrick, eds., Internal Reflection Spectroscopy, Review and Supplement, Harrick Scientific Corporation, New York, 1985.

15. W. Frank, W. Goertz, and H.H. Belz, " Spectral Attenuation of Optical Fibers Measured by FT-IR Spectroscopy ", Appl. Spect. 41, 323 (1987).

16. P.M. Fredricks, P.J. Samson, and A.D. Stuart, " Characterization of Optical Fibers Using Modified FT-IR Spectrometer ", Appl. Spect. 41, 327 (1987).

17. N.A. Wright, R. Curbelo, D.A.C. Compton and S.L. Hill, " The Use of Mid-Infrared Optical Fibers for Analytical Applications ", SPIE Vol. 1048, 153 (1989).

18. M.D. DeGrandpre and L.W. Burgess,"A Fiber-Optic FT- NIR Evanescent Field Absorbance Sensor", Applied Spectroscopy, 44, 273(1990).

19. S. Simhony, E.M. Losower, and A. Katzir, "Novel attenuated total internal reflectance spectroscopic cell using infrared fibers for aqueous solutions", Applied Physics Letters, 49, 253(1986).

20. S.Simhony and A. Katzir, "Fourier Transform Infrared Spectra of Organic Compounds in Solution and as Thin Layers Obtained by Using an Attenuated Total Internal Reflectance Fiber- Optic Cell", Analytical Chemistry, 60, 1908(1988).

21. S. Simhony, I. Schnitzer, A. Katzir, and E.M. Kosower, "Evanescent wave infrared spectroscopy of liquid using silver halide optical fibers", Journal of Applied Physics, 64, 3732(1988).

22. M. Katz, A. Bornstein, I. Schnitzer, and A. Katzir, "Evanescent wave spectroscopy using chalcogenide glass fiber: theoretical analysis and experiments", in Infrared Fiber Optics III, J.A. Harrington, A. Katzir, Editors, SPIE Proceedings, Volume 1591, 236(1991).

23. W.Wallace, D.W Hoeppner, *Aircraft Corrosion : Causes and Case Histories* , AGARD Corrosion Handbook, Vol.1. 1985.

24. V.L. Snoeyink and David Jenkins, *Water Chemistry* , John Wiley & Sons, Inc., 1980.

25. *Aircraft Weapons Systems Cleaning and Control*, Technical Manual, NAVAIR, 01-1A-509, Naval Air Systems Command, Washington, September,1980.

26. W. Gerhartz, *Ullmann's Encyclopedia of Industrial Chemistry*, Vol. 1, 1985.

27. M. Beaver, *Encyclopedia of Materials Science and Engineering*, Pergamon Press & The MIT press, Vol. 1, 1986.

28. G.M. Scamans and C.D.S. Tuck, *In Environment-Sensitive Fracture of Engineering Materials*, TMS-AIME, New York, 1979.

29. D.A. Krohn, *Fiber optic sensors*, Instrument society of America,1992.

30. A.W Snyder and J.D. Love, *Optical Wave guide Theory*, Chapman and Hall, 1983.

31. P. Lorrain and D. Corson, *Electromagnetic Field and Waves*, Second Edition, W.H Freeman and Co, 1970.

32. G. Muller, K. Abraham, and M. Schaldach,"Quantitative ATR Spectroscopy: Some Basic Considerations," Applied Optics, 20, 1182(1981).

33. M. Katz, A. Katzir, I. Schnitzer, and A. Bornstein, "Quantitative evaluation of chalcogenide glass fiber evanescent wave spectroscopy," Applied Optics, 33, 5888(1994).

34. P.R. Griffiths and J.A. deHaseth, *Fourier Transform Infrared Spectrometry*, John Wiley and Sons, 1986.

35. D.R. Mattson, "Sensitivity of a Fourier Transform Infrared Spectrometer", Applied Spectroscopy, 32, 335(1978).

36. Bio-Rad Digilab Division, 237 Putnam Avenue, Cambridge, Massachusetts 02139.

37. J.S. Namkung, M.L. Hoke, and R.S. Rogowski, "Characterization and Application of Optical Fibers with FT-IR Spectroscopy", Proceedings of the 9th International Conference on Fourier Transform Spectroscopy, J.E. Bertie ed., Calgary Alberta, Canada, 23-27 Aug. 1993.

38. C.W. Brown and Z. Ge, "Ins and Outs of Fiber Optics for Chemical Analysis", Bio-Rad Digi-Lab Division FTS/IR Note No. 87, 1991.

39. J.T. Baker Chemical Company, Phillipsburgh, NJ 08865.

40. J.S. Namkung, M.L. Hoke, and R.S. Rogowski, " Optical Fiber FTIR Remote Detection of Aluminum Hydroxide " SPIE proceeding on North American Conference on Smart Structures and Materials, Vol. 2191, pp. 526-535, February, 1994

41. J.S. Namkung, M.L. Hoke, R.S. Rogowski, and S. Albin, " FTIR-Optical-Fiber Remote Detection of Aluminum Hydroxide by Evanescent Wave Absorption Spectroscopy " Applied Spectroscopy, Vol. 49, No. 9, pp. 1305-1310, September, 1995

42. Bio-Rad Sadler Division, 3316 Spring Garden Street, Philadelphia, Pennsylvania

43. J.S. Namkung, M.L. Hoke, R.S. Rogowski, and S. Albin, " Detection of Aluminum Corrosion by Evanescent Wave Absorption Spectroscopy With Optical Fibers " SPIE proceedings on North American Conference on Smart Structures and Materials, Vol. 2444, pp. 447-458, February, 1995.

44. J.S. Namkung, M.L. Hoke, R.S. Rogowski, and S. Albin, " Optical Fiber FTIR Evanescent Wave Absorption Spectroscopy of Natural Aluminum Corrosion " SPIE Proceedings on Optical Remote Sensing for Environmental and Process Monitoring, Vol 2883, VIP-55, pp. 655-669, September, 1995

45. G. Herzberg, Molecular Spectra and Molecular Structure, II Infrared and Raman Spectra of Polyatomic Molecules, D. Van Nostrand Company, New York, 1964.

46. R.M Goody, *Atmospheric Radiation*, Vol. I : Theoretical Basis, Oxford, pp. 125-130, 1964.

APPENDIX I

Evaluating the following square root:

$$[\mathrm{Sin}^2\,\theta - (n_2^c/n_1)^2\,]^{1/2} \tag{1}$$

for the case of a complex refractive index $n_2^c = n_2\,(1+i\,\kappa_2)$.

Write (n_2^c/n_1) as $n_{21}\,(1+i\,\kappa_2)$, where $n_{21} = (n_2/n_1)$. Then the argument in the square root,

$$\mathrm{Sin}^2\theta - n_{21}^2\,(1+i\,\kappa)^2 \tag{2}$$

may be written in the form $(\nu - i\,\mu)$:

$$(\nu - i\,\mu) = [\,\mathrm{Sin}^2\theta - n_{21}^2\,(1-\kappa)^2\,] - (\,i\;2n_{21}^2\;\kappa\,) \tag{3}$$

with real part which we define as ν:

$$\nu \equiv [\,\mathrm{Sin}^2\theta - n_{21}^2\,(1-\kappa)^2\,] \tag{4}$$

and a complex part which we define as μ:

$$\mu \equiv 2n_{21}^2\;\kappa \tag{5}$$

Notice that μ here differs from the expression found in the literature, which as given by Muller is $2(n_2/n_1)^2\,\kappa^2$ here.

Assume that the complex square root which we seek has the form $(X + iY)$, so that

$$(X + i\,Y) = (\nu - i\,\mu)^{1/2} \tag{6}$$

Then writing $(X+iY)^2 = (\,X^2-Y^2\,) + i\,2XY$, equating real and complex parts of $(X^2-Y^2) + i\,2XY$ and $(\nu - i\,\mu)$ yields:

$$(X^2-Y^2) = \nu \tag{7}$$

and

$$2XY = -\mu \tag{8}$$

Solving for X and Y we find, after some algebra:

$$X = (1/\sqrt{2}\,)\,[\pm\,[\,\nu^2 + \mu^2\,]^{1/2} + \nu\,]^{1/2} \tag{9}$$

$$Y = (1/\sqrt{2}\,)\,[\pm\,[\,\nu^2 + \mu^2\,]^{1/2} - \nu\,]^{1/2} \tag{10}$$

We have to chose between the (+) and (-) sign so that the real part of the square root has a negative sign. This will make the magnitude of the evanescent field decrease with increasing Z. This means that we must chose the positive sign (+) and the final answer for the square root is:

$$(\nu - i\,\mu\,)^{1/2} = (\,\mathrm{Re} + i\,\mathrm{Im}\,) \tag{11}$$

where

$$\mathrm{Re} = (1/\sqrt{2}\,)\;\;[\pm\,[\,\nu^2 + \mu^2\,]^{1/2} + \nu\,]^{1/2} \tag{12}$$

$$\mathrm{Im} = (1/\sqrt{2}\,)\,[\pm[\,\nu^2 + \mu^2\,]^{1/2} - \nu\,]^{1/2} \tag{13}$$

APPENDIX II

Derive expressions for the Fresnel Loss (1-R) for the perpendicular ($1-R_N$) and parallel ($1-R_P$) polarizations, in the approximation of small absorption index, κ.

First consider the perpendicular polarization. Begin with the expression for the reflectivity, R_N given in the main text:

$$R_N = \frac{\mathrm{Cos}^2\theta + [\nu^2+\mu^2]^{1/2} - \sqrt{2}\,\mathrm{Cos}\,\theta\,[[\nu^2+\mu^2]^{1/2}-\nu]^{1/2}}{\mathrm{Cos}^2\theta + [\nu^2+\mu^2]^{1/2} + \sqrt{2}\,\mathrm{Cos}\,\theta\,[[\nu^2+\mu^2]^{1/2}-\nu]^{1/2}} \qquad (14)$$

Then the Fresnel loss ($1-R_N$) for this polarization will be:

$$1-R_N = \frac{\sqrt{2}\,\mathrm{Cos}\theta\,[[\nu^2+\mu^2]^{1/2}-\nu]^{1/2}}{\mathrm{Cos}^2\theta + [\nu^2+\mu^2]^{1/2} + \sqrt{2}\,\mathrm{Cos}\theta\,[[\nu^2+\mu^2]^{1/2}-\nu]^{1/2}} \qquad (15)$$

The central approximation is to assume that $n_{21}^2\kappa^2$ in the expression for ν, is much smaller than $n_{21}^2\kappa$ in the expression for μ, since κ is assumed to be much less than 1. Then, in that approximation ν will be:

$$\nu \approx \mathrm{Sin}^2\theta - n_{21}^2 \qquad (16)$$

With this, $(\nu^2+\mu^2)$ will be given approximately by:

$$(\nu^2+\mu^2) \approx (\mathrm{Sin}^2\theta - n_{21}^2)^2 \cdot \left[1 + \frac{4\,n_{21}^4\,\kappa^2}{(\mathrm{Sin}^2\theta - n_{21}^2)^2}\right] \qquad (17)$$

Since the second term, proportional to κ^2, is assumed to be small, the square root $(\nu^2+\mu^2)^{1/2}$ can be approximated as:

$$(\nu^2+\mu^2)^{1/2} \approx (\mathrm{Sin}^2\theta - n_{21}^2) \cdot \left[1 + \frac{2\, n_{21}^4\, \kappa^2}{(\mathrm{Sin}^2\theta - n_{21}^2)^2} \right] \tag{18}$$

Based on this approximation the term $[(\nu^2+\mu^2)^{1/2} - \nu]$ will be:

$$[(\nu^2+\mu^2)^{1/2} - \nu] = \frac{2\, n_{21}^4\, \kappa^2}{(\mathrm{Sin}^2\theta - n_{21}^2)} \tag{19}$$

And finally, the square root $[(\nu^2+\mu^2)^{1/2} - \nu]^{1/2}$ is given by:

$$[(\nu^2+\mu^2)^{1/2} - \nu]^{1/2} = \frac{\sqrt{2}\, n_{21}^2\, \kappa}{(\mathrm{Sin}^2\theta - n_{21}^2)^{1/2}} \tag{20}$$

which becomes more obvious when written in the following way:

$$[(\nu^2+\mu^2)^{1/2} - \nu]^{1/2} \approx \mu / \sqrt{(2\nu)} \tag{21}$$

This completes the approximations needed to evaluate $(1-R_N)$.

If these approximations are inserted into the expression for the reflectivity R_N, and the Fresnel loss $(1-R_N)$ given above, the result is:

$$R_N \approx \frac{\mathrm{Cos}^2\theta + \nu - \sqrt{2}\,\mathrm{Cos}\theta\ (\mu/\sqrt{2\nu})}{\mathrm{Cos}^2\theta + \nu + \sqrt{2}\,\mathrm{Cos}\theta\ (\mu/\sqrt{2\nu})} \tag{22}$$

or

$$R_N \approx \frac{(1 - n_{21}^2) - [(2\,\mathrm{Cos}\theta\, n_{21}^2\, \kappa) / (\mathrm{Sin}^2\theta - n_{21}^2)^{1/2}]}{(1 - n_{21}^2) + [(2\,\mathrm{Cos}\theta\, n_{21}^2\, \kappa) / (\mathrm{Sin}^2\theta - n_{21}^2)^{1/2}]} \tag{23}$$

and

$$(1-R_n) = \frac{4\, n_{21}^2\, \mathrm{Cos}\,\theta\, \kappa}{(1 - n_{21})\,(\mathrm{Sin}^2\theta - n_{21}^2)} \tag{24}$$

Next, consider the parallel polarization. From the main text of the theory, the reflectivity, R_P is given as (u-v)/(u+v). The Fresnel loss will then be $(1-R_P) = 2v/(u+v)$ where (u,v) are given

by:

$$u = \mathrm{Cos}^2\theta[\,(\mathrm{Sin}^2\theta - \nu)^2 + \mu^2\,] + [\,\nu^2 + \mu^2\,]^{1/2} \tag{25}$$

and

$$v = \sqrt{2}\,\mathrm{Cos}\theta\,\{(\mathrm{Sin}^2\theta - \nu)\,[\,[\,\nu^2 + \mu^2\,]^{1/2} - \nu]^{1/2} + \mu\,[\,[\,\nu^2 + \mu^2\,]^{1/2} + \nu\,]^{1/2}\} \tag{26}$$

The same approximations above, that were used to derive $(1-R_N)$, can be used to obtain approximations for (u,v). Neglecting the terms containing κ^2 and κ^4, u is given approximately as:

$$u \approx (\,\mathrm{Cos}\,\theta \bullet n_{21}{}^4\,) + (\mathrm{Sin}^2\theta - n_{21}{}^2) \tag{27}$$

One additional approximation is needed to obtain an approximation for v. From the expression for $(\nu^2 + \mu^2)^{1/2}$ given above, a clearly reasonable approximation for $[\,(\nu^2 + \mu^2)^{1/2} + \nu\,]^{1/2}$ can be obtained,

$$[\,(\nu^2 + \mu^2)^{1/2} + \nu\,]^{1/2} \approx [\,(\mathrm{Sin}^2\theta - n_{21}{}^2)^{1/2} \bullet [\,2 + \frac{2\,n_{21}{}^4\,\kappa^2}{(\mathrm{Sin}^2\theta - n_{21}{}^2)^2}\,]\,]^{1/2} \tag{28}$$

by dropping the term μ^2, which is proportional to κ^2:

$$[\,(\nu^2 + \mu^2)^{1/2} + \nu\,]^{1/2} \approx \sqrt{2}\,(\mathrm{Sin}^2\theta - n_{21}{}^2)^{1/2} \tag{29}$$

which becomes clear when written as:

$$[\,(\nu^2 + \mu^2)^{1/2} + \nu\,]^{1/2} = \sqrt{(2v)} \tag{30}$$

With this additional approximation, v becomes:

$$v \approx \sqrt{2}\,\mathrm{Cos}\,\theta \left\{ n_{21}^2 \left[\mu / \sqrt{(2v)}\right] + \left[\mu\sqrt{(2v)}\right] \right\} \tag{31}$$

or

$$v = \sqrt{2}\,\mathrm{Cos}\,\theta\, n_{21}^2\, \kappa\, (\mathrm{Sin}^2\theta - n_{21}^2)^{1/2} \bullet \left[2 + \frac{n_{21}^2}{(\mathrm{Sin}^2\theta - n_{21}^2)} \right] \tag{32}$$

Because v is proportional to κ, it will be dropped in the denominator of $(1\text{-}R_P)$, which then becomes $2v/u$:

$$(1\text{-}R_P) \approx \frac{4\, n_{21}^2\, \mathrm{Cos}\,\theta\, \kappa \bullet (\mathrm{Sin}^2\theta - n_{21}^2)^{1/2}}{(\mathrm{Cos}^2\theta \bullet n_{21}^2) + (\mathrm{Sin}^2\theta - n_{21}^2)} \bullet \left[2 + \frac{n_{21}^2}{(\mathrm{Sin}^2\theta - n_{21}^2)} \right] \tag{33}$$